Doctoral Thesis

Evaluation of Locomotion Performance for a Wheel-Paddle Robot

September 2019

Doctoral Program in Advanced Mechanical Engineering and Robotics

Graduate School of Science and Engineering

Ritsumeikan University

SHEN Yayi

Doctoral Thesis Reviewed
by Ritsumeikan University

Evaluation of Locomotion Performance for a Wheel-Paddle Robot (車輪パドルを有するロボットのための運動性能評価)

September 2019
2019 年 9 月

Doctoral Program in Advanced Mechanical Engineering and Robotics
Graduate School of Science and Engineering
Ritsumeikan University

立命館大学大学院理工学研究科
機械システム専攻博士課程後期課程

SHEN　Yayi
シェン　ヤイ

Supervisor：Professor　MA　Shugen
研究指導教員：馬　書根　教授

Fall 2019

A thesis submitted in fulfillment of the requirements for the degree of Doctor of Philosophy

Committee in Charge:

- Professor MA Shugen, Chair
- Professor HIRAI Shinichi
- Professor UENO Satoshi

"You've got to travel over a lot more string to get to the pearls..."

Begin Again

Abstract

Evaluation of Locomotion Performance for a Wheel-Paddle Robot

by

Yayi SHEN

Doctor of Philosophy

Department of Robotics, Graduate School of Science and Engineering

RITSUMEIKAN UNIVERSITY

To help the human beings conducting search and rescue tasks after disasters, the eccentric paddle mechanism was proposed for robot to access various severe amphibious terrains. The design concept is to balance the advantages and disadvantages in both wheeled robot and legged robot, so as to improve the mobility. Moreover, the specialty of the eccentric paddle mechanism is its reconfigurability, which endows the robot with high adaptability in different situations.

Previous work has analyzed the motion modes on a single module prototype. But a complete robot that can be utilized in outdoor fields has not been developed. And the locomotion performance in amphibious environment needs to be explored thoroughly. The main contributions of this thesis include two parts: first is concerning the terrestrial locomotion, where the trafficability of a new fabricated wheel-paddle robot is evaluated on various rough terrains, especially on soft terrain; second is on the aquatic locomotion, where the propulsion efficiency is further improved.

First, a robot prototype that consists of four wheel-paddle modules has been designed and fabricated. Considering the severe environment that the robot will be sent to, necessary protection measures are adopted. Waterproof scheme is added to the electronic system, and sandproof is realized in the gear chamber to ensure the motion accuracy of the paddle shaft. The chain transmission is employed to transfer the torque from the motors to the

wheel-paddle mechanism, which is efficient and more robust in field environment. Besides, a complete control system has been designed, including hardware and software. It has been tested that the control system can realize accurate control of the robot and feedback necessary data.

Based on the new fabricated robot prototype, a hybrid locomotion mode is proposed for traversing terrestrial terrains, which include normal flat floor, rough grass, big stones, small gravels, or even soft terrain like sand. The reason of using this hybrid mode is that the previous legged modes were only suitable for flat ground, but can not be applied to rough terrains directly. And comparing with them, the hybrid mode is easier to be controlled. While dealing with variable terrain situations, the configuration of the wheel-paddle can be transformed quickly by only adjusting the location of the paddle shaft. And during usual locomotion, only the wheel is actuated to generate traction force, which is more efficient.

The robot performing with the hybrid mode is primarily verified in rigid terrains, including three normal rough terrains (grass, stone, gravel) and one flat terrain (floor). It is found that the robot consumes more energy in rough terrains. But comparing with previous legged modes, the efficiency of the hybrid mode in rough terrains is similar with the legged modes on flat ground. In addition, the locomotion speed is increased, which is near one body length per second.

Then, the trafficability of the robot with hybrid mode in sand is investigated particularly due to the special properties of soft terrain, which makes the interaction between the robot and the terrain more complex and variable. First the paddle terredynamics is studied theoretically and experimentally. The results have shown that longer protruding length of the paddles can generate larger traction force. To find out how the protruding paddle length affects the locomotion performance, an indoor testbed that allows one wheel-paddle module moving freely in horizontal and vertical directions is built. It is found that the wheel-support configuration is easy to slip at high locomotion speeds, while the protruding paddles have effectively reduced the slippage and increased the efficiency. The optimal configuration is concluded to be paddle-support according to the results. But the only disadvantage of

the long protruding paddle length is the vertical vibration brought to the system. The locomotion performance of the whole robot in outdoor sand is also evaluated, in which the hybrid-support configuration is the most efficient. The locomotion speed increases with the rotational speed of the wheel, while the efficiency tends to be better at higher locomotion speed. From the evaluation in both indoor testbed and outdoor field, it is found that the locomotion performance also varies with the system inertia and the sand properties. They affect the slippage and sinkage between the robot and the soft terrain, so as to affect the locomotion performance.

At last, the propulsion performance of one wheel-paddle module with different swimming modes are explored. A hydrodynamic model that is suitable for our mechanism is first built to predict the thrust. Then the thrusts generated by the oscillating paddling mode (fish-like) and the rotational paddling mode (propeller-like) are analyzed through simulation and experiment. The results have shown that the rotational mode is superior in generating large amplitude of thrust, while the oscillating mode is more efficient. Both of them can produce linear directional thrust when adjusting the location of the paddle shaft. However, large negative thrust was found in oscillating mode, which is a waste of energy. To further enlarge the thrust amplitude in oscillating mode and increase the propulsion efficiency, a novel front crawl stroke (human-inspired) is proposed. It is verified that the front crawl stroke can generate more than three times net thrust than the oscillating mode, and has increased the propulsion efficiency as well.

The evaluation of the locomotion performance has further verified the mobility and adaptability of the configurable wheel-paddle robot in various field terrains. It also inspires the future work towards real application in amphibious environment.

Acknowledgements

I would first like to thank my supervisor, dear professor Shugen Ma, who gave me the chance to study here and he has given me very valuable advices on my research. Besides, he is patient, kind, and always concerned about me, which I do not deserve it and I really appreciate.

My research could not go favorably without the assistance from Dr. Guoteng Zhang who used to be a postdoctoral researcher in BioInMech Lab and Dr. Yang Tian who is currently a special assistant professor in BioInMech Lab. Not only in the specialized knowledge, but also in the method of doing research have they given me many suggestions. I am grateful to their general help in all aspects. I would give thanks to all the members in BioInMech Lab. Particularly, I want thank Mr. Yuya Inoue and Mr. Hiroki Tomita, who helped me conducting the experiments outside no matter how hot or cold the weather is. Thanks to Dr. Atsushi Kakogawa, Mr. Jie Ma, Mr. Zhe Qiu for their support and kindness. Thanks to all the other members that I apologize for not mentioning, thanks for your help and friendship.

I would like to thank all the Ritsumeikan University staff who helped me with many affairs and documents. They are always patient and careful. I would also like to thank professor Huayan Pu, Dr. Yi Sun, Dr. Yang Yang and Mr. Jinglei Zhao in Shanghai University, China, who gave me useful advices and support sometimes.

Last but not least, I would like to thank my parents for their continuous support during all my life and the doctoral study abroad. I would also like to thank the China Scholarship Council for the financing support of my three years' life in Japan, which allows me focusing on the research confidently.

It has been ten years since I first step into university. I would like to thank fate for all of these. I love this world and all of you guys.

Contents

List of Figures

List of Tables

Chapter 1

Research Background

1.1 Motivation

To access various amphibious environment and conduct search and rescue tasks after huge disasters, an amphibious mechanism named as the eccentric paddle mechanism has been developed [1]. The eccentric paddle mechanism can also be recognized as a configurable wheel-paddle integrated mechanism due to its reconfigurability. The specific configuration applied to the locomotion is variable and dependent on the actuation of all three joints inside the mechanism. So far, the study that have been carried out on this mechanism can be separated into four aspects. First is about the mechanism design and the fabrication of single module prototype. Second is the planning of locomotion mode such as race-walking and non-reciprocating legged mode, which could be utilized in normal ground situation. At the same time, the interaction between the wheel-paddle mechanism and soft soil was experimentally studied as well, regarded as the third aspect. Lastly, two swimming modes were proposed and the generated forces were measured and analyzed. The to date outputs concerning these studies are listed in Appendix. B.

However, a complete robot prototype with robust mechanism and stable control system has not been created till now. Most previous work were based on one module prototype. As a result, the locomotion performance of a complete robot with wheel-paddle mechanism

has not been well studied yet. Besides, the previously designed locomotion modes could only be used on flat ground, and the control of the motion is complex. To access various severe terrain situations, a simple but effective locomotion mode is in an urgent need. As for the locomotion on soft terrain, the interaction between the robot and the substrate need be investigated deeply, and so as to suggest a plan for traversing soft terrain effectively and efficiently. In case of the underwater performance, the characteristics of the propelling thrusts have not been studied thoroughly. And the performance differences between the two proposed swimming modes should be compared to establish an optimal swimming solution.

1.2 Research Objectives

Based on the motivations, the first objective we are achieving in this thesis is to design and fabricate a complete wheel-paddle robot prototype based on the eccentric paddle mechanism. The prototype should be able to traverse severe terrains such as debris, sand, mud, et al.. Hence, necessary protection mechanisms should be added to the robot, and a simple but effective locomotion mode will be applied. Based on the new robot prototype and the new locomotion mode, evaluation of the locomotion performance will be conducted on various rough terrains (including rigid terrain and soft terrain), where the emphasis falls in soft terrain (defined as granular media). The propulsion performance of the two swimming modes will also be evaluated and compared. Based on the results, an optimized swimming mode is proposed to maximize the propelling thrust and efficiency. At last, discussions about the wheel-paddle robot will be given based on the evaluation and future work will be clarified.

1.3 Literature Review

Literature review will be presented from three aspects according to the research contents of this thesis. First the existing robots that can be applied to rough terrains will be

summarized. Then relevant studies on the granular media locomotion is explained. At last, we introduce the existing underwater robots.

1.3.1 Rough Terrain Robots

Due to the rapid growth of sciences and technologies, robots are required to conduct more and more tricky and dangerous missions in harsh environment such as searching and rescuing after huge disasters, terrain mapping, mine inspecting and so on. To traverse on such harsh environments or rough terrains, excellent mobility of a mobile robot is necessary. But it is still challenging to develop a robot that can negotiate variable rough terrains, e.g. grass, stones, stairs, sand, mud, et al..

In the latest decade, various locomotion mechanisms and mobile robots have been designed and fabricated to adapt to various environment. According to the design principle, they can be sorted into three categories: wheeled, legged and hybrid robotic systems. To be specifically, wheeled robots usually can realize fast and efficient locomotion on flat ground. And comparatively, legged robots can achieve accurate and dynamic locomotion on rough terrains. A well-known legged robot is the quadruped Titan series [2] which can perform stable movement with articulated legs on uneven ground. In order to achieve better locomotion performances such as high-speed behavior, efficiency and obstacle negotiability, great efforts have been made by many research teams, such as IIT's hydraulic quadruped HyQ series [3, 4], ETH's ANYmal for hash environments [5], or MIT's electrically actuated cheetah [6]. On the other hand, the hybrid robots are often built on various special mechanisms. A prevalent one is the hexapod RHex series [7, 8, 9] that use a simple actuator and compliant legs to realize rough terrain negotiation. Besides, leg-wheel integrated robot is also popular, such as leg-wheel transformable robot TurboQuad [10], Wheel Transformer [11], and a claw-wheel transformable robot [12].

Nevertheless, it is still a great challenge to realize both the adaptability in rough terrains and the high locomotion efficiency at the same time. For instance, the RHex robot [7] can negotiate rough terrain with high reliability, but it is not as efficient as the Titan robot

[2] or the TurboQuad [10] robot. A robot that is capable of efficient locomotion on rough terrains needs to be developed.

1.3.2 Locomotion on Soft Terrain

While performing in outdoor fields, the robots will come into a variety of complex terrain situations and need to negotiate with them. According to the properties of the substrate, terrains can be roughly separated into two categories. One is named as rigid terrain which substrate are usually hard and not easy to get deformed, e.g., rocks, gravels, stairs, or debris. Another category is called soft terrain where the substrate is deformable or flowable under extra stresses, e.g., sand, mud, soil, or snow. The substrate that consists of soft terrain is granular media, which is defined as collections of discrete particles [13]. The granular media can exhibit behaviors between solid and fluid [14, 15, 16]. Besides, the water content is variable in the granular media. Depending on the water content, granular media is classified into dry granular media and wet granular media. The difference between them is whether cohesion forces are generated among the particles [17].

A number of existing mobile robots are still limited to the locomotion on rigid terrains as summarized in the previous section [4, 5, 9]. As for the locomotion on granular media, most of existing works are about the research on the dry granular media. A prevalent research was done by Li et al with the Sandbot. They discovered that the dynamics of the robot on granular media depends sensitively on the actuation parameters [13, 18]. Moreover, a terradynamical model that can predict the interaction forces between the granular media and locomotor was successfully built in [19]. Besides, the Carnegie Mellon University realized sidewinding motion of a snake robot and they looked into the physics of sidewinding on granular slopes [20, 21]. Mazouchova et al got inspiration from sea turtle and developed a sea turtle inspired robot which used limbs and flippers to move forward [22]. They investigated how the limb-sand interaction affects the locomotion performance of the robot. Since the wet granular media is more complicated than the dry granular mdeia, specifically the rheology varies a lot along with water-solid ratio. Therefore, seldom research about the

robotic locomotion on wet granular media have been involved. Zhang et al experimentally studied the performance of a flipper-legged robot in muddy terrain [23].

1.3.3 Underwater Robots

Underwater robots are being widely used in conducting tasks in aquatic environment, e.g. oceanic exploration, oil device maintenance or even searching and rescuing. Based on the design approach and the propelling principle, existing underwater robots generally include the unmanned underwater vehicles (UUVs) which are propelled by rotary propellers, and the biomimetic swimming robots which are usually inspired by fish and they propel through undulatory or oscillatory motion of either body or fins [24]. Some research results have proved that biomimetic swimming robots can achieve higher energy efficiency than the UUVs, at the same time better dynamic performance and noiseless locomotion [25]. However, some other studies believe that the rotary propellers are more efficient than the biomimetic swimming robots, but fish can realize superior maneuverability during the swim [26, 27]. Yet, in current stage of technology it is still challenging to build a biomimectic underwater robot which can completely imitate the mechanism and motion of real fish. Moreover, the diversity of species is providing us with various imitating choices, but meanwhile has raised the difficulty of screening as well.

Recently, many researchers are working toward improving the swimming performance of biomimetic underwater robots [28, 29, 30, 31, 32, 33, 34, 35]. To figure out the relations between the thrust performance and fish fin shape, K. Kikuchi classified the morphological shape of fish fin into different polygonal shapes and compared them experimentally [28]. K. Feilich discovered that the shape of the caudal fin might interact with the flexural compliance in complicated forms to generate propelling forces [29]. Noticing the variable stiffness in bodies of real fish, K. Lucas analyzed the role of non-uniform bending stiffness during fish propulsion [30] and Y. Park proposed a novel mechanism that is capable of varying its stiffness during swimming based on the kinematic condition for maximizing the thrust [31, 32]. Nevertheless, it was found that in most existing underwater robots with oscillatory

or undulatory swimming motion, both positive and negative propelling forces were produced in the horizontal or forward direction during the swimming, where the existence of negative forces will waste the energy and decrease the efficiency [28, 29, 30, 36, 37, 38]. To resolve this defect, we tried to add compliance to the fish fin like paddle as well as perform asymmetrical oscillating motion. But the results did not show significant improvement [39, 40].

Most of the above studies focus on imitating morphology and kinetics of fish, but there are also some other aquatic animals that possess efficient swimming skills. For example, Y. Song learned from water strider and developed water strider robot based on surface tension [41]. X. Jia got inspiration from the whirligig beetle and proposed an energy-efficient surface propulsion mechanism, which can maximize the positive force in power stroke while minimizing the negative force in recovery stroke [42].

1.4 Thesis Organization

The organization of this thesis is as follows. Chapter 1 introduces the motivation and objectives of this thesis. Literature review on relevant fields are also presented.

Chapter 2 first introduces the concept of the eccentric paddle mechanism and some previous work about the developed one-module prototype. Then the new fabricated robot prototype is presented from mechanical design in Section. 2.3 and control system design in 2.4 respectively. The mechanical design includes the waterproof and sandproof scheme applied to the robot. To be applied in severe environment, transmission mechanism is also improved. The control system design is introduced from electronic system and control structure of the robot. The specifications of the robot are listed in Section. 2.5. And as the most important also the weakest part of the robot, the paddle shaft's stress is also analyzed through simulation before putting into use to ensure the effectiveness. A summary is given in Section. 2.6.

Chapter 3 presents the evaluation of the robot trafficabiltiy on rigid terrains, which include floor, grass, stone and gravel. First the previously planned gaits for flat ground

application are introduced in Section. 3.1. To traverse various rough terrains, the hybrid locomotion mode is proposed and the robot kinematics is presented as well in Section. 3.2. To verify the new fabricated robot prototype and the hybrid locomotion mode, experiments are conducted in Section. 3.3 with various terrain situations. The locomotion speed, system vibration, current consumption during the trials are recorded, and the energetic efficiency is calculated and analyzed. Discussions among the hybrid mode and previous locomotion modes, also among our wheel-paddle robot and other mobile robots are given in Section. 3.4.

Chapter 4 specially analyzes the trafficability of the wheel-paddle robot on soft terrain. The paddle terradynamics which studies the interaction between the paddle and the granular media (sand) will be presented theoretically and experimentally in Section. 4.2. Based on the terradynamic force study, to primarily evaluate the locomotion performance of one wheel-paddle module, an indoor testbed allowing the module to move freely in both vertical and horizontal directions is built in Section. 4.3. By actuating the wheel-paddle module with different rotational velocities as well as various configurations, the trafficability is evaluated from traversing speed, efficiency and vertical vibration. Then the whole robot prototype is placed in outdoor field sand to analyze the overall trafficability in Section. 4.4. At last, we discuss the trafficability of the robot over soft terrain based on the evaluation results in Section. 4.5.

Chapter 5 presents comprehensive evaluation of the propulsion performance of one wheel-paddle module in aquatic environment. Firstly, Section. 5.1 introduces the existing two swimming modes and the relevant previous work. Section 5.2 provides an effective method of modeling the hydrodynamic forces generated by our mechanism. To verify the model and evaluate more detailed characteristics of both swimming modes, a force measuring experimental setup is built in Section. 5.3. Experiments of both modes with different kinematic conditions are conducted and the results will be explained from the thrust magnitude, the thrust direction and the propulsion efficiency. However, large negative thrusts were found in the results of oscillating paddle mode, which is a waste of energy. This prob-

lem will be optimized in Section. 5.4 through a novel human-inspired swimming mode. At last, we compare and discuss the propulsion performance of the swimming modes in Section. 5.5.

Chapter 6 provides an extensive discussion on the locomotion performance of the wheel-paddle robot in terms of an overall scale.

Chapter 7 summarizes the important findings of this thesis and suggests the direction that future study may take with regard to wheel-paddle robot.

Appendix A presents supplemental experiments conducted with the robot prototype, which are not the main research objectives but could be reference to the readers. Specifically, Section. A.1 gives the results of the robot following desired trajectory, which proved the kinematics of the robot. Section. A.2 shows the ability of the robot dealing with obstacles and slops. To ensure the control accuracy of the paddle shaft, verification tests were also conducted in Section. A.3. Appendix B lists all the publications so far of the wheel-paddle robot for the readers' information.

1.5 List of Publications

The following is a list of the publications that were written during the doctoral course and lead to the writing of this thesis. The list contains both journal papers and conference papars, which is listed in chronological order.

1. Yayi Shen, Huayan Pu, Yi Sun, Shugen Ma, Shaorong Xie, Jun Luo and Wenchuan Jia, Generating vectored thrust with the rotational paddling gait of an ePaddle-EGM mechanism: Modeling and experimental verifications, *IEEE Journal of Oceanic Engineering*, vol.42, no.3, pp. 522–531, 2017. DOI: 10.1109/JOE.2016.2576181 (© 2017 IEEE.)

2. Yayi Shen, Yi Sun, Huayan Pu and Shugen Ma, Experimental verification of the oscillating paddling gait for an ePaddle-EGM amphibious Locomotion mechanism,

IEEE Robotics and Automation Letters (with *IROS 2017* option), vol.2, no.4, pp. 2322–2327, 2017. DOI: 10.1109/LRA.2017.2707124 (© 2017 IEEE.)

3. Yayi Shen, Guoteng Zhang, Yang Tian and Shugen Ma, Development of a wheel-paddle integrated quadruped robot for rough terrain and its verification on hybrid mode, *IEEE Robotics and Automation Letters*, vol.3, no.4, pp. 4062–4067, 2018. DOI: 10.1109/LRA.2018.2862431 (© 2018 IEEE.)

4. Yayi Shen, Shugen Ma, et al., Development of a Multi-terrestrial Robot with Eccentric Paddle Mechanism, In *Proc. of the 2018 JSME Conference on Robotics and Mechatronics (*ROBOMECH 2018*)*, Kitakyushu, Japan, pp. 2A2–L07, Jun., 2018. DOI: https://doi.org/10.1299/jsmermd.2018.2A2-L07

5. Yayi Shen, Huayan Pu and Shugen Ma, Realizing efficient front crawl stroke with a wheel-paddle integrated mechanism: inspired by human competitive swimming, *IEEE Journal of Oceanic Engineering*, Early access, 2019. DOI: 10.1109/JOE.2019.2896398 (© 2019 IEEE.)

6. Yayi Shen, Shugen Ma, et al., Study on a novel swimming gait of an eccentric paddle mechanism, In *Proc. of the 2019 JSME Conference on Robotics and Mechatronics (*ROBOMECH 2019*)*, Hiroshima, Japan, Jun., 2019.

7. Yayi Shen, Shugen Ma, Guoteng Zhang and Syuya Inoue, Locomotion Performance of a Configurable Paddle Wheel on Granular Media Terrain, *IEEE Robotics and Automation Letters*, Under review.

Chapter 2

Robot Design

As claimed in the background, the terrain situations after disasters are quite tough and complex, which may include debris, stones, slops, mud, or even aquatic environment. It is of great danger and difficult for human beings to access such terrains to conduct search and rescue tasks. Hence, robots with outstanding locomotion abilities that can negotiate variable amphibious terrains are desirable.

In existing amphibious robots of either biomimetic ones or hybrid ones, most of them are only acquired of few locomotion modes, which can not be applied in complex amphibious environment after disasters. This chapter will introduce the design and fabrication of a special wheel-paddle integrated robot that can realize various locomotion modes adapting to the terrain situation. The concept of the core locomotion mechanism utilized in the robot, which is called eccentric paddle mechanism, is firstly shown in Section. 2.1. Relative work on the design of the mechanism will be briefed in Section. 2.2. Then the complete mechanical design and control system of the new fabricated robot will be illustrated in Section. 2.3 and Section. 2.4, respectively. Finally, we introduce the overall specifications of the robot and analyze the stresses of key parts in Section. 2.5. Summary is given in Section. 2.6.

2.1 Concept of the Eccentric Paddle Mechanism

2.1.1 Components

The concept of eccentric paddle mechanism was first introduced in [1]. Considering the advantages and disadvantages of both wheeled robots and legged robots in various environment, the concept combining wheel and legs together was proposed. Different with normal hybrid locomotion mechanism, our concept can achieve variable configurations and locomotion modes.

The schematic drawing of the concept is depicted in Fig. 2.1. The main components in one eccentric paddle mechanism include a wheel that can rotate around its center and four paddles that can rotate around the paddle shaft. All the paddles protrude or retract freely through the hinges that are evenly located at the wheel rim. Specifically, each hinge indicates a revolute pair and a sliding pair. The specialty of this mechanism lies in the controllability of the paddle shaft's location. It can be controlled to reach anywhere inside the wheel. The vector from the wheel center to the paddle shaft is called eccentricity, which is also the reason we named this mechanism the eccentric paddle mechanism. As a result, the configuration of the mechanism is changeable. And combining with the rotation of the wheel, various locomotion modes can be realized.

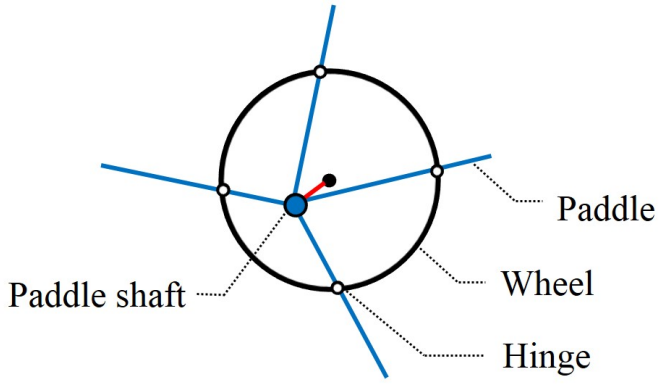

Figure 2.1. Concept of the eccentric paddle mechanism.

2.1.2 Versatile Locomotion Modes

As shown in Fig. 2.2, the near-earth paddles can be retracted into the wheel completely if the paddle shaft is located at the highest eccentricity. Since only the wheel contacts with the ground in this situation, it is called wheeled mode. And the wheeled mode is good at fast and energy efficient locomotion on flat ground. But when the terrain becomes uneven like steps or needs more accurate control on the trajectories of the paddle tips, legged mode can be applied to realize stable locomotion. Another mode that can be achieved by the mechanism on terrestrial terrain is wheel-leg-integrated motion, where both the wheel and the paddle interact with the substrate. This motion has more advantages in rough terrain like sandy soil or mud since it is able to improve the trap problem of purely legged mode and reduce the slippage in wheeled mode, which helps access severe regions after disasters. As for aquatic swimming, the paddles can generate effective propelling thrusts due to the larger area compared with normal rod shaped legs.

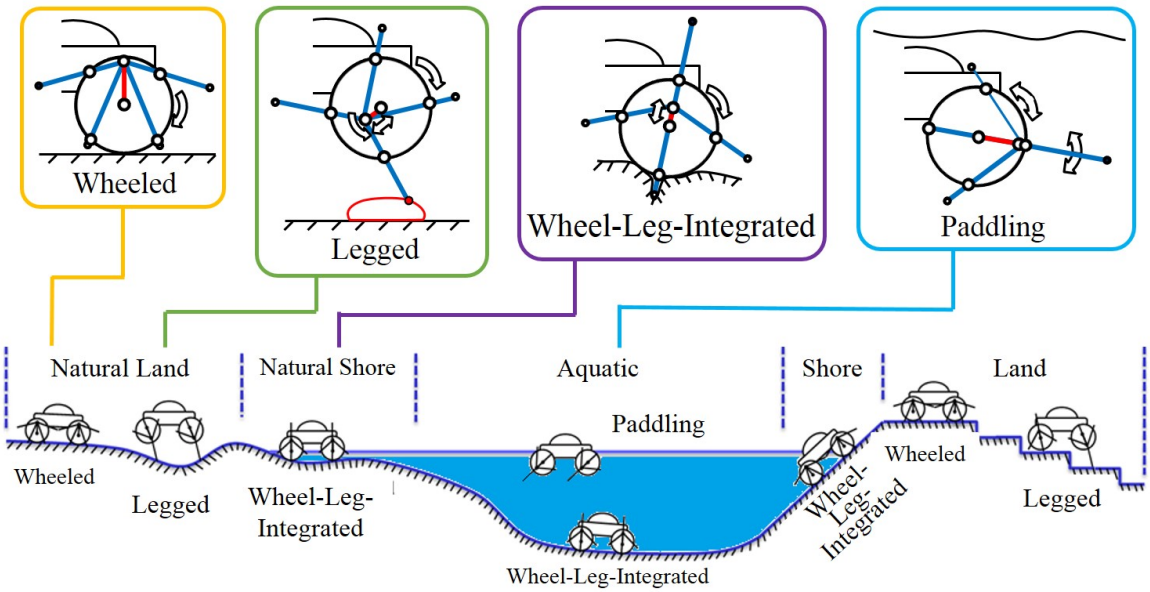

Figure 2.2. Feasible locomotion modes realized by eccentric paddle mechanism in various amphibious environment.

The four amphibious modes mentioned above are generalized ideas based on the features of the locomotion. Exact motion sequence or pattern could be varied according to the application scenarios. Details will be illustrated in this thesis hereinafter.

2.2 Relative Work

2.2.1 Single Module Design

In order to implement the motion of each joint as expressed in Section. 2.1, an eccentric paddle mechanism based on the planetary gear system has been proposed and a single-module prototype has been fabricated [43, 44]. As shown in Fig. 2.3(a)(b), both front and back view of the 3-D model are presented. To reach any position within the wheel, the paddle shaft is actuated by a planetary gear system, which is composed of a sun gear, a planet gear and a planet carrier. The paddle shaft is solidly connected with the planet gear by the paddle shaft carrier. As expressed in the concept, the four paddles can rotate freely around the paddle shaft, and the attitudes of the paddles are passively controlled by the rotation of the wheel. The paddles can protrude out of the wheel or retract into the wheel freely through the hinges. The picture of the prototype is shown in Fig. 2.3(c) while the schematic drawing of the mechanism is shown in Fig. 2.3(d). To be specifically, letter S indicates the paddle shaft, O and O_1 are the centers of sun gear and planet gear separately, segment OO_1 and O_1S correspond to the effective lengths of the planet carrier and the paddle shaft carrier respectively. Only one paddle (black line) is seen in the schematic drawing for simplification. The main design parameters of the mechanism are listed in Table 2.1.

2.2.2 Kinematics

In this eccentric paddle mechanism, there are three rotational joints that are actively controlled, which are the wheel joint (θ_0), the sun gear (θ_1) and the planet carrier (θ_2). The sun gear and the planet carrier jointly control the location of the paddle shaft, while the rotation of the wheel can vary the attitude angle of the paddles. The eccentricity from the paddle shaft (S) to the wheel center (O) is defined by the eccentric distance (r_S) and the eccentric angle (θ_S). As a result, we can obtain a mapping relation from the system inputs

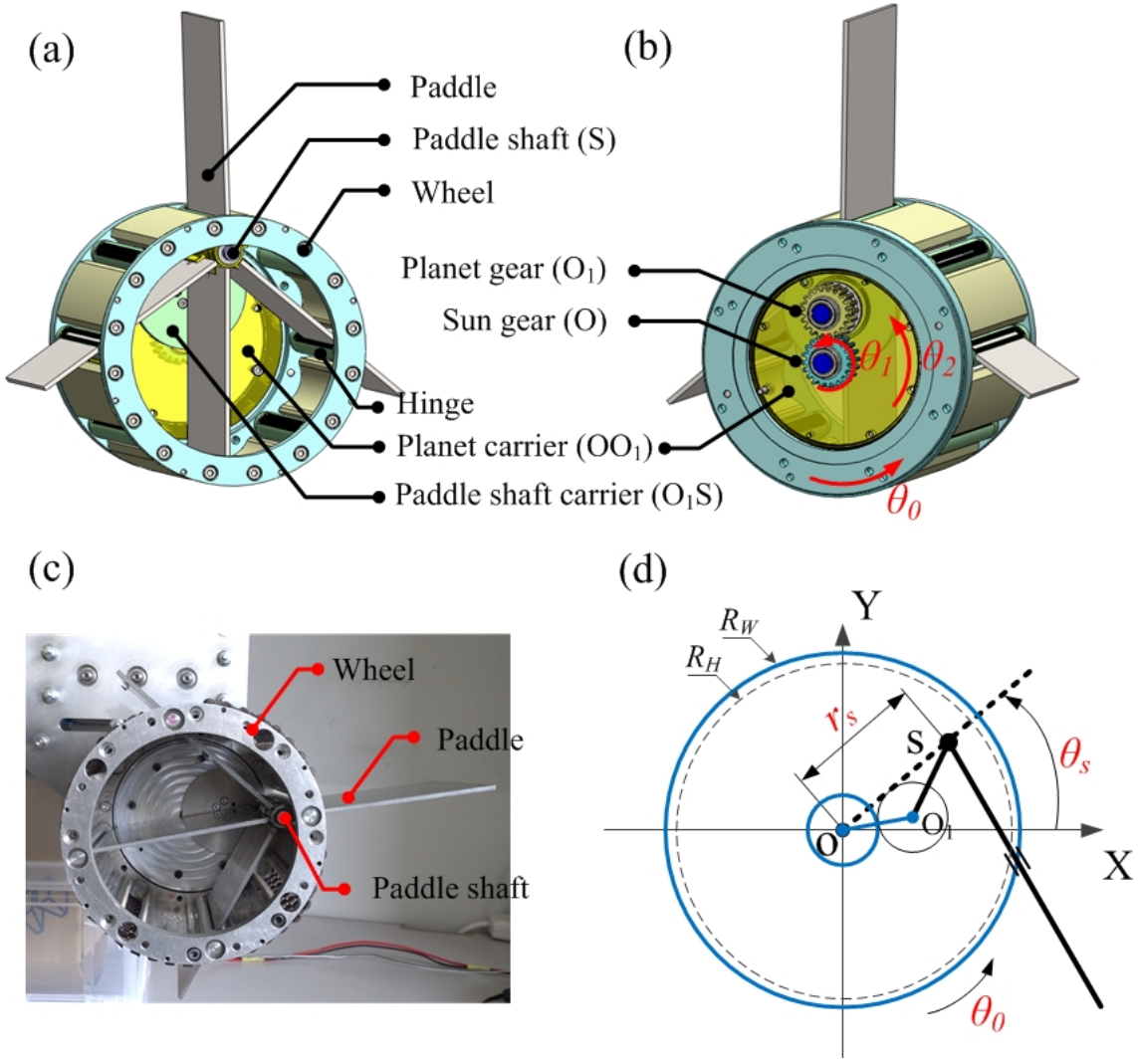

Figure 2.3. Single module design of the eccentric paddle mechanism: (a) front view of the 3-D model; (b) back view of the 3-D model; (c) picture of one prototype; (d) schematic drawing of the mechanism.

Table 2.1. SPECIFICATIONS OF THE ECCENTRIC PADDLE MECHANISM

Description	**Symbol**	**Value**
Radius of wheel	R_W	56mm
Hinges layout radius	R_H	50mm
Pitch circle diameter of sun/planet gear	d	20mm
Effective length of planet carrier	OO_1	20mm
Effective length of paddle shaft carrier	O_1S	20mm
Paddle length	l	96.5mm
Paddle width	a	63mm
Paddle thickness	b	2mm

to the outputs, described as

$$\boldsymbol{f}: \begin{bmatrix} \theta_1 \\ \theta_2 \\ \theta_0 \end{bmatrix} \rightarrow \begin{bmatrix} r_S \\ \theta_S \\ \theta_0 \end{bmatrix} \tag{2.1}$$

.

The joint kinematics of the eccentric paddle mechanism is depicted in Fig. 2.4. The configuration of the i-th (i = 1, 2, 3, 4) paddle is decided by the position of the paddle shaft (x_S, y_S) and the attitude angle of each paddle θ_{P_i}. They can be calculated through the geometric relations in the mechanism. Specifically, it can be expressed as

$$\boldsymbol{\chi_{pi}} = \begin{bmatrix} x_S \\ y_S \\ \theta_{P_i} \end{bmatrix} = \begin{bmatrix} d\cos\theta_2 + d\cos(3\theta_2 - \theta_1) \\ d\sin\theta_2 + d\sin(3\theta_2 - \theta_1) \\ \mathrm{atan2}(\mathrm{y_{H_i}} - \mathrm{y_S}, \mathrm{x_{H_i}} - \mathrm{x_S}) \end{bmatrix} \tag{2.2}$$

where d is the diameter of the sun gear and planet gear, θ_1 and θ_2 indicate the input angles of the sun gear and the planet carrier. (x_{H_i}, y_{H_i}) is the coordinate of the i-th paddle hinge, which can be expressed as

$$\boldsymbol{H_i} = \begin{bmatrix} x_{H_i} \\ y_{H_i} \end{bmatrix} = \begin{bmatrix} R_H \cdot \cos\theta_{H_i} \\ R_H \cdot \sin\theta_{H_i} \end{bmatrix}, (\theta_{H_i} = \theta_0 + (i-1)\pi/2) \tag{2.3}$$

where R_H is the radius of the hinges layout circle, θ_0 is the angular position of the wheel, and θ_{H_i} is the angular position of the i-th paddle hinge. When the actuated joints of the wheel θ_0, the sun gear θ_1 and the planet carrier θ_2 are known, the motion state of the eccentric paddle mechanism can thus be obtained from

$$\boldsymbol{\chi} = \begin{bmatrix} r_S \\ \theta_S \\ \theta_0 \end{bmatrix} = \begin{bmatrix} d\sqrt{2(1+\cos(2\theta_2 - \theta_1))} \\ 2\theta_2 - \theta_1/2 \\ \theta_0 \end{bmatrix} \tag{2.4}$$

.

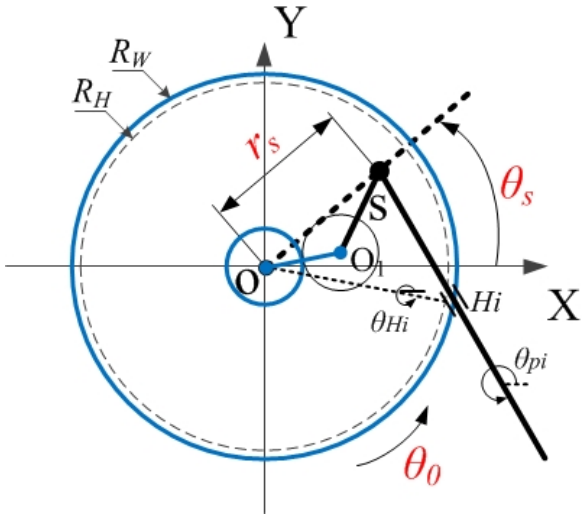

Figure 2.4. Kinematics of the eccentric paddle mechanism.

According to the mapping relation $\boldsymbol{f}$, the motion states of both the wheel and the paddles can be obtained based on the given inputs. Since the mapping $\boldsymbol{f}$ is reversible, inverse kinematics can also be derived to actuate the mechanism so as to achieve desired trajectories of the wheel and the paddles.

2.3 Mechanical Design of the Robot

The basic principle and the single-module prototype of the eccentric paddle mechanism has been introduced. However, a complete and reliable robot prototype which can be employed in real severe amphibious environment has not been developed. This section

involves the mechanical design of a wheel-paddle integrated robot that based on the eccentric paddle mechanism. The new developed robot prototype is shown in Fig. 2.5 [45]. It consists of a body that is covered by carbon fiber plates and enclosed with whole electronic system, and four wheel-paddle modules which are assembled with the body through aluminum plates and beams.

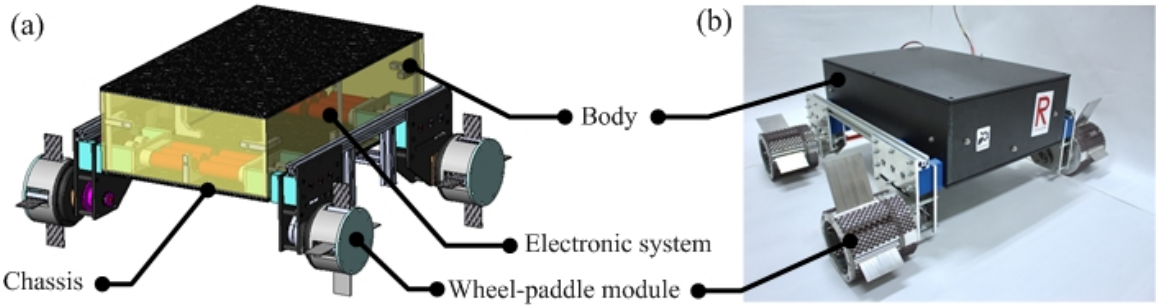

Figure 2.5. Prototype of the wheel-paddle integrated robot: (a) 3-D model; (b) picture.

Considering the application of the robot in severe terrains which contain tiny particles or water like mud or sand, the reliability and stability of the robotic system should be maintained during the locomotion. Therefore, the electronics system should be isolated from outside so that dust and water will not affect the normal operation of the electric parts. Besides, due to the complexity and the accuracy of the transmission system, even very small particles can not be allowed to get into the clearance among the parts. Or else the transmitting inaccuracy, unsteadiness, or even failure will happen to the transmission system and affect the electronic parts as well. However, it is known that the paddle shaft follows a two degree-of-freedom planar motion and the paddles protrude or retract through the hinges in the wheel to contact with the environment, so it is difficult to realize sealing or isolation for the whole robot. As a result, a compromised protection mechanism was designed, where the electronics system is protected from both water and little granules, the eccentric paddle mechanism is protected from granules, and the transmission method is also improved.

2.3.1 Waterproof Scheme

To realize waterproof for the body that enclosing the electronic system, both static sealing method and dynamic sealing method are employed. As shown in Fig. 2.6, to achieve waterproof of the body, it is crucial to implement the sealing between the body and the driving shafts because of the existing relative rotation. These driving shafts deliver torques from the motors to the eccentric paddle mechanism. So the inputs of these shafts are the rotation motion of the motor inside the body, and the output ends transmit torques to the joints in each wheel-paddle module through chains. To achieve sealing between the body and the driving shafts, stuffing boxes were designed and used. As seen in the cross-section drawing of the stuffing box, it mainly includes a V-ring and the felt that is saturated with grease. When the shaft is driven to rotate, the boundary film will be produced around the surface of the shaft. The film can lubricate the rotational motion of the shaft. And at the same time, since the boundary film is not uniform, the effect of labyrinth is to form and prevent the water or dust from intrusion.

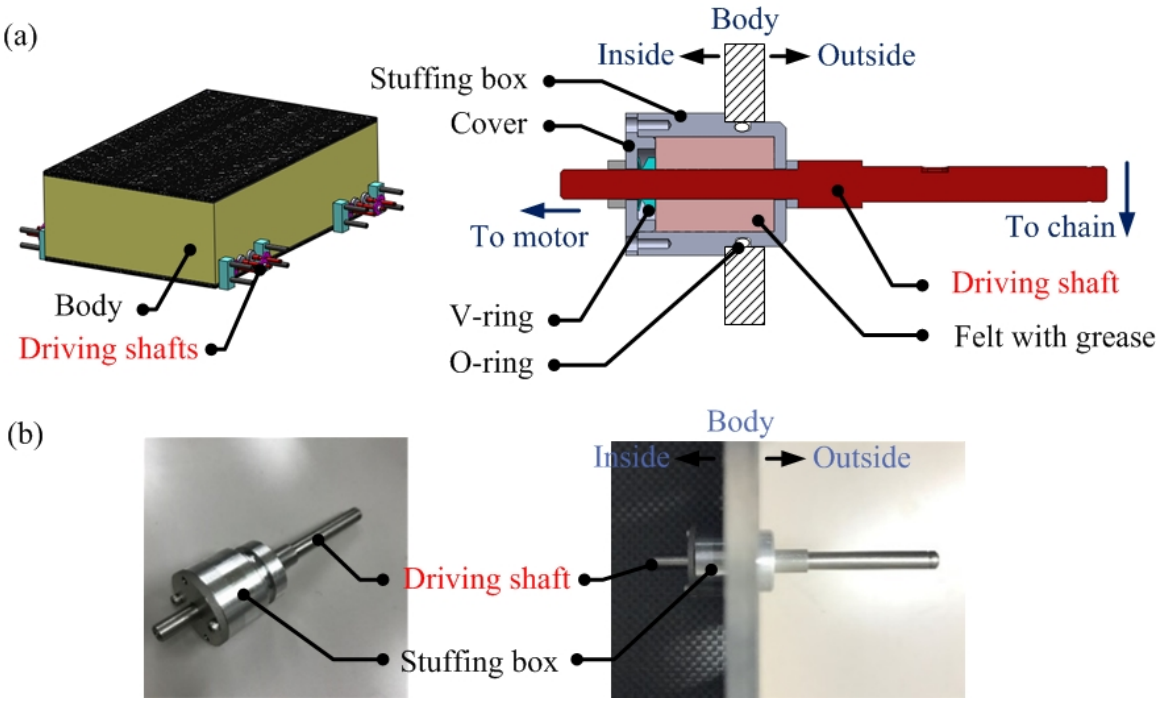

Figure 2.6. Waterproof scheme applied between the body and the driving shafts: (a) structural diagram; (b) picture of stuffing box.

2.3.2 Sandproof Scheme

The sandproof scheme was achieved to each wheel-paddle module. As shown in Fig. 2.7, one wheel-paddle module and its cross-section drawing are depicted. Some parts like the paddles are not shown in the figure for clearance. As described in previous sections, the motion accuracy of the paddle shaft is essential to vary the configuration of the wheel-paddle module and control the whole robot. And since the paddle shaft is actuated by the planetary gear system which is easy to fail when little granules get inside. Therefore, sandproof scheme was applied to the planetary gear mechanism to ensure the performance of the paddle shaft. As shown in the cross-section drawing, wool felts are inserted into the gap between two components that rotate relatively to realize isolation. For instance, felts exist between the paddle shaft carrier and the planet carrier, between the wheel rim cover and the planet carrier, and between the body connector and the wheel rim. As a result, the chamber containing the planetary gear mechanism is protected from outside granules. The gear chamber is enclosed within red lines as shown in the figure.

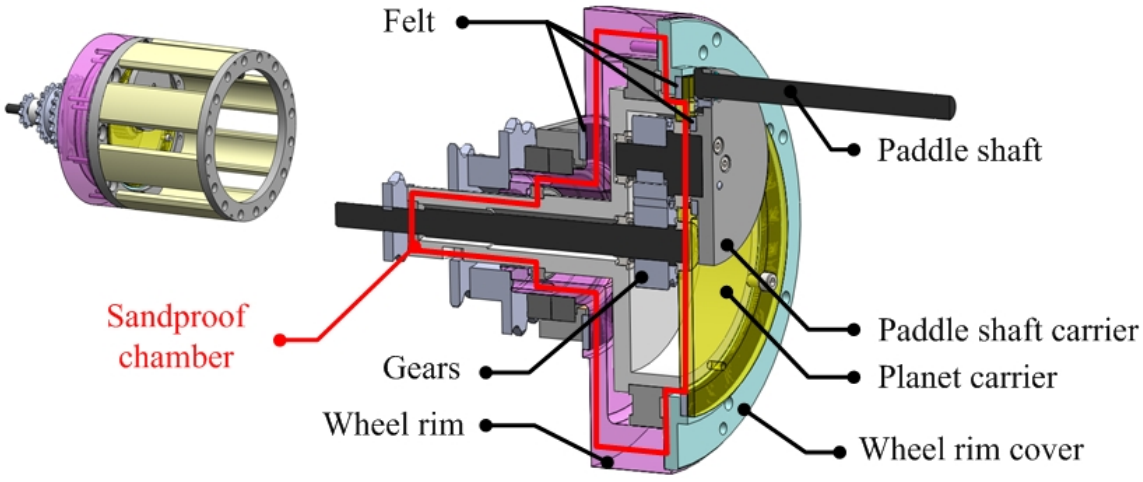

Figure 2.7. Sandproof scheme applied to the planetary gear mechanism.

To verify the effectiveness of both the waterproof and sandproof schemes, tests were conducted based on the stipulation of the International Protection Marking standard (IEC 60529). The results have shown that the protection level of the body reaches IP65, which means no ingress of dust and water jet. And the protection level of the gear chamber is

IP53, where it can stop the dust and spraying water. Hence, it is recognized that the robot can be utilized in rough terrains with granules or puddles, and also feasible on water surface.

2.3.3 Transmission Mechanism

Previously, gears were applied to transmit torque from the motors to the eccentric paddle mechanism. However, gears are easy to fail if granules go into the backlash. And the multistage transmission reduced the accuracy as well as adding the whole weight of the mechanism. To ensure the robustness and effectiveness in harsh environment, chain transmission was employed in this robot instead of gears or timing belts. Besides, chain achieves the best transmitting efficiency among the three methods. As shown in Fig. 2.8, three chain wheels are used to actuate one wheel-paddle module. To be specifically, the chain wheels in the dashed line box of Fig. 2.8(b) actuate the sun gear, the planet carrier and the wheel joint respectively. And they are connected with the motors through chains.

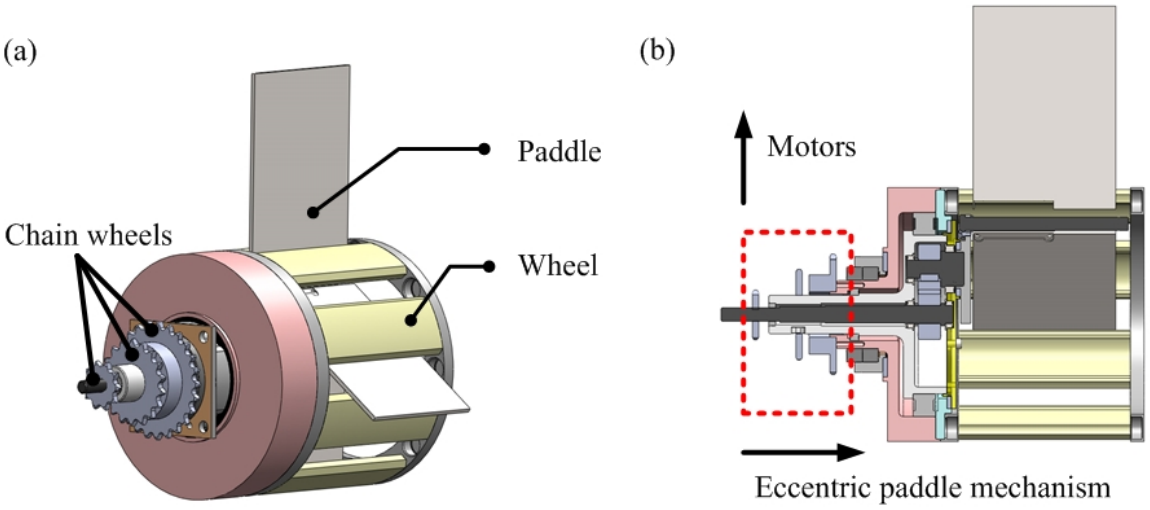

Figure 2.8. Chain wheel transmission diagram: (a) isometric view; (b) cross-section view.

Tension device is necessary for chain transmission to ensure the operating effectiveness. Whereas no standard parts could be used directly due to the space limit. As a result, a POM (polyformaldehyde) gasket shown in Fig. 2.9 was utilized to tension the chain.

POM is widely used for fabricating special tension devices due to its characteristics of self lubricating and abrasion resistance.

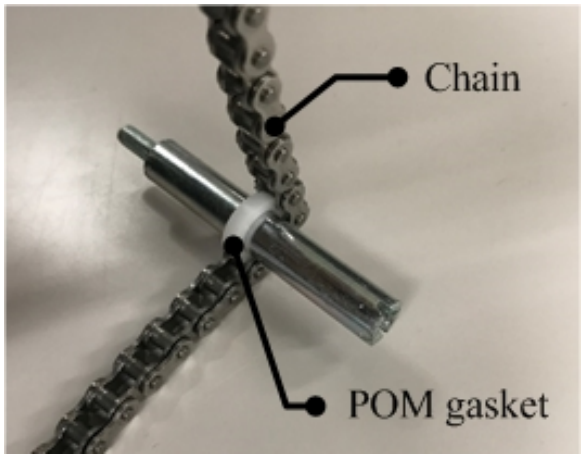

Figure 2.9. POM gasket used for tensioning the chain.

2.4 Control System Design

2.4.1 Electronic System

The electronic system involves the higher layer and the lower layer. The higher layer includes a main computation power which is a PC that works under Windows 64-bit operating system at the frequency of 3.30 GHz. It transmits data with four individual MCUs (MC9S12XS256, NXP, Netherlands) at lower layer through CAN communication. Each individual MCU controls one wheel-paddle module, which may include the PID (abbr. for proportional-integral- differential) control for DC (abbr. for direct current) motors and reading the encoders. Each wheel-paddle module contains three DC motors (RE25, Maxon motor, Switzerland, Type power: 20W) which are the integration of motor, gearbox, and incremental encoder. The motors are actuated by the motor drivers made from VNH5019 (Pololu, USA, Type: 5.5-24V, 30A) which has large voltage range and the current can be measured as well. To obtain the real time position and orientation of the robot, a Kinect Box (Microsoft, USA) was assembled to the top of the body. The electronic parts of lower layer inside the body are shown in Fig. 2.10.

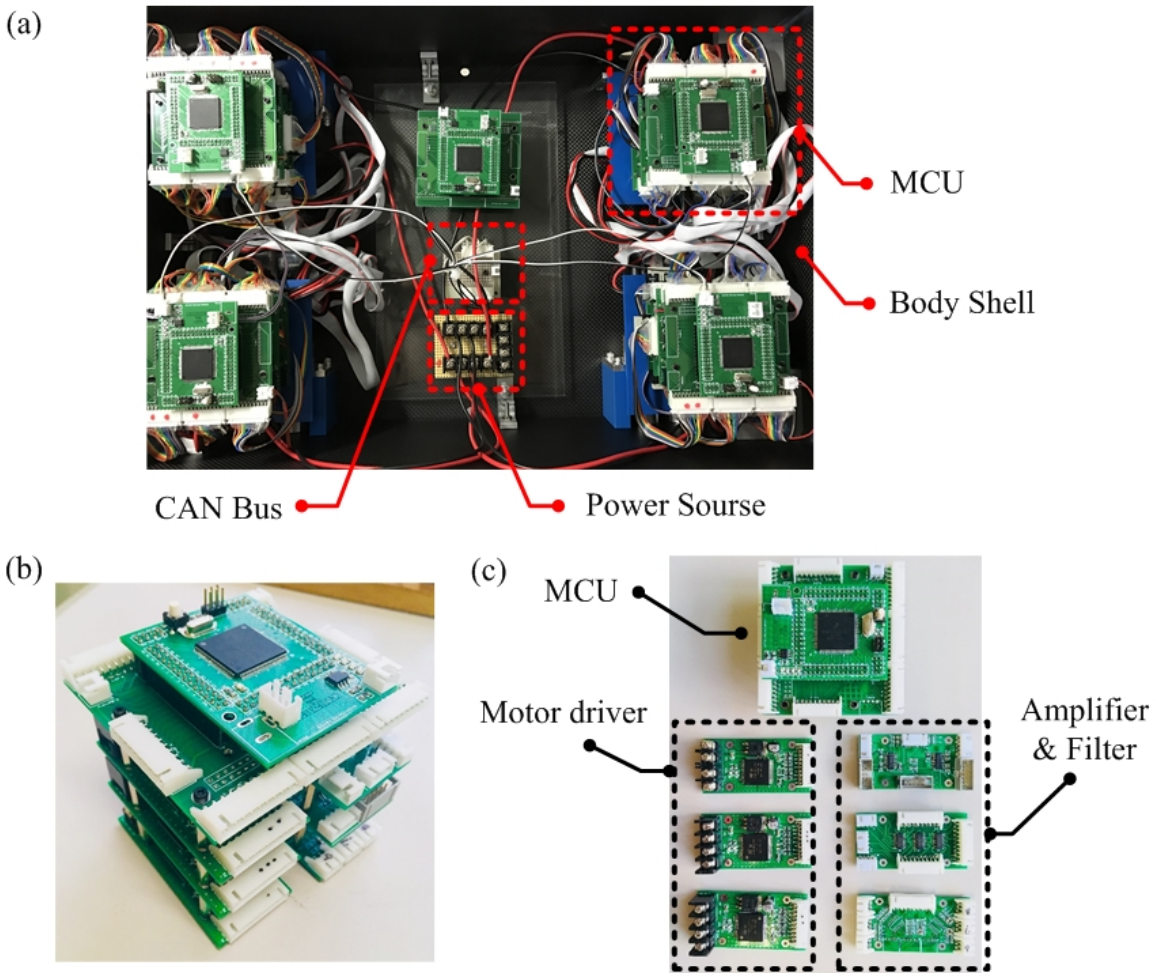

Figure 2.10. Electronic system of lower layer inside the body shell: (a) overall layout; (b) individual MCU picture; (c) components in one individual MCU.

2.4.2 Control Structure

The full control structure of the robot is shown in Fig. 2.11, which is composed of three layers. High-level commands such as speed, orientation and locomotion modes are sent from the higher PC layer. These commands will be first converted into joint velocities through kinematics or inverse kinematics of the robot. Then the joint velocities are sent to the behavior layer as inputs for velocity control. The behavior layer contains four sub-control units, corresponding to four MCUs. Each MCU controls three DC motors that drive one wheel-paddle module. The ground-truth motion of the robot which include the position and orientation is obtained by a Kinect Box to feedback to the PC layer. An UI (User Interface) was developed with Visual Studio (Microsoft) in the PC layer to send control commands and record feedback data. The interface is captured as shown in Fig. 2.12.

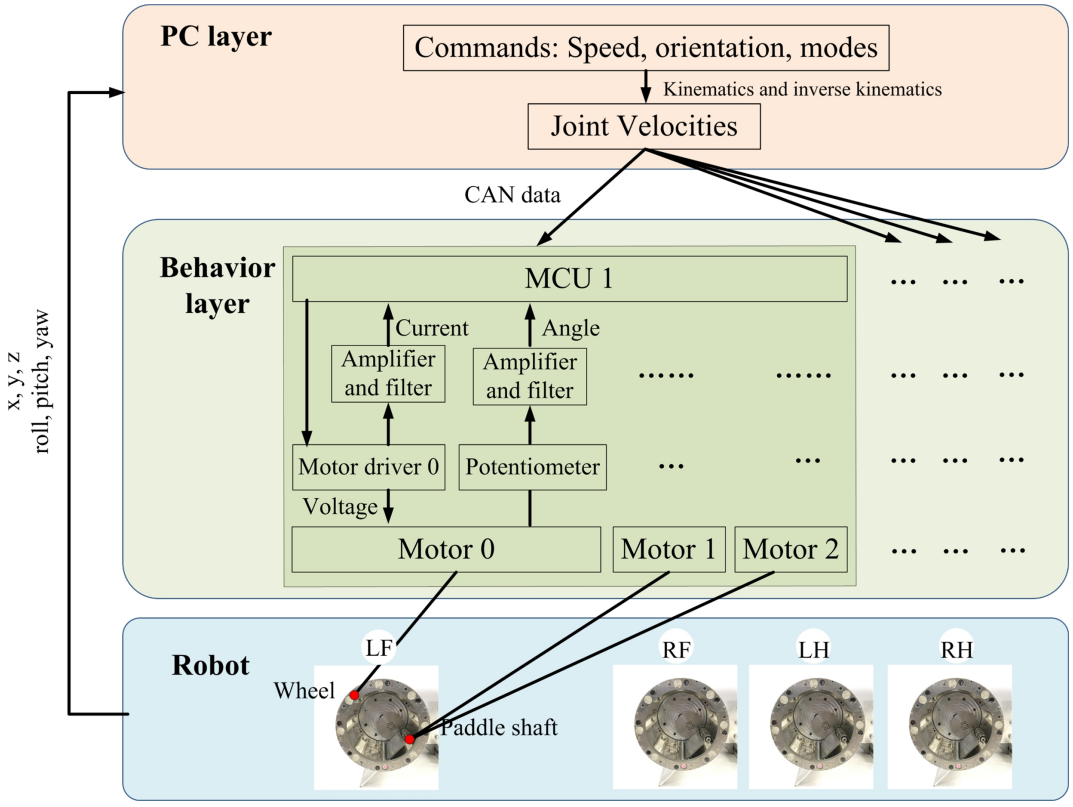

Figure 2.11. Control structure of the robot [45].

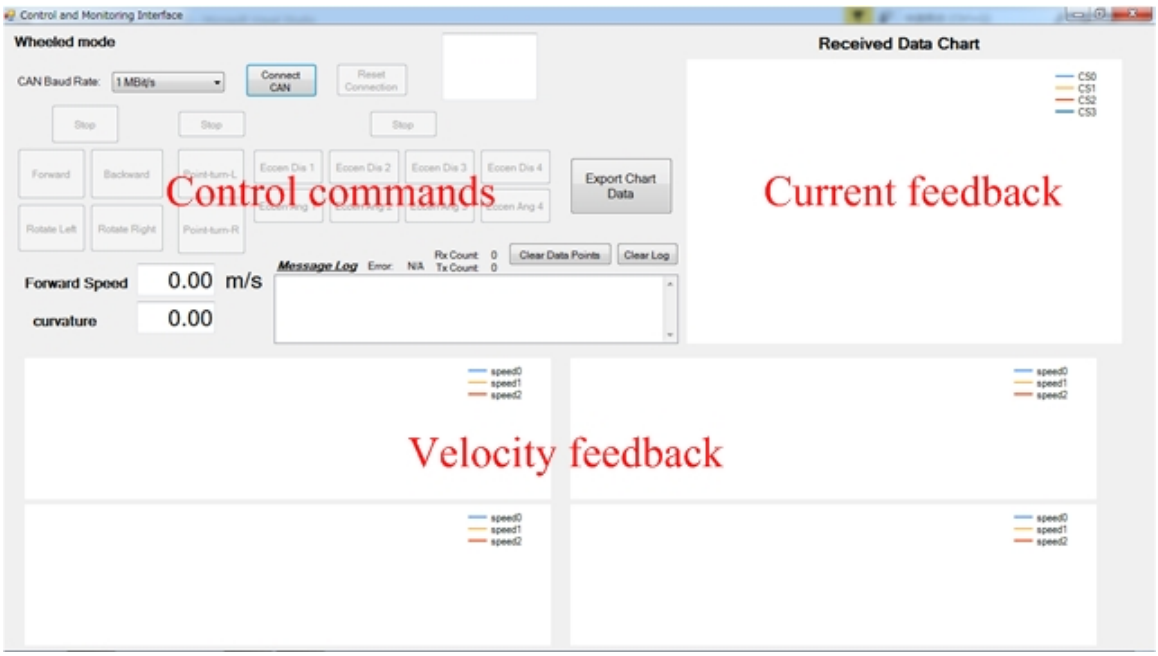

Figure 2.12. Screen capture of the user interface in PC layer.

2.5 Specifications and Safety Analysis

The specifications of the robot are summarized in Table 2.2. It was found that the robot weighs much heavier than the previous single module. To be specifically, the weight that each wheel-paddle module needs to undertake is larger than the previous. To ensure the safety of the mechanism, stress analysis was conducted on the weakest part of the robot: paddle shaft. The paddle shaft works like a cantilever beam which need to support the whole weight of the robot and endure the impulse transiting from the ground to the paddles. The considered situation is shown in Fig. 2.13, which consists of a single-end fixed paddle shaft, a paddle clamp and a paddle with external loads applying vertically upside. The robot was assumed to fall freely from a certain height above the ground. According to the robot size and the possible locomotion modes, the falling height was set as 0.1 m, which is much larger than the radius of the wheel. Thus, the external loads applying on the paddles can be calculated through the theorem of impulse as:

$$F \cdot \Delta t = m \cdot \Delta v \tag{2.5}$$

where F is the sum forces that applied on all the four paddles from all wheel-paddle modules, Δt is the impulse time that starts from the contacting instant during falling and ends with the moment of robot bouncing up. In the simulation the impulse time was set as 0.1 s. And m is the mass of the whole robot as shown in Table 2.2. But considering a safety factor, m equals 30 kg in the stress simulation. Δv indicates the velocity variance during the impulse, which is obtained through:

$$\Delta v = 2\sqrt{2gh} \tag{2.6}$$

where g is the acceleration of gravity and h is the falling height.

Table 2.2. ROBOT SPECIFICATIONS

Descriptions		Values	Units
Length	Body	0.5	m
	Axle-to-axle	0.42	m
Width	Body	0.32	m
	Body include wheel	0.61	m
Height	Body	0.15	m
	Ground to chassis (min)	0.116	m
	Ground to chassis (max)	0.196	m
Wheel diameter		0.112	m
Wheel width		0.112	m
Weight	One Wheel-paddle	1.7	kg
	Body	14	kg
	Total	24	kg

The stress simulation was conducted in Solidworks and the results could be found in Fig. 2.13. Fig. 2.13(a) shows the mesh result of the analyzed parts and the mesh details are listed in Table 2.3. Based on the real situation, the fixture and the external loads are depicted in Fig. 2.13(b) with green and red arrows respectively. The stress along the paddle shaft is shown in Fig. 2.13(c), where the maximum value is 184.7 MPa. Since carbon steel was utilized to fabricate the paddle shaft, which yield strength (220.59 MPa) is mush larger

than the simulated peak value, it is concluded that the paddle shaft can perform securely in the locomotion.

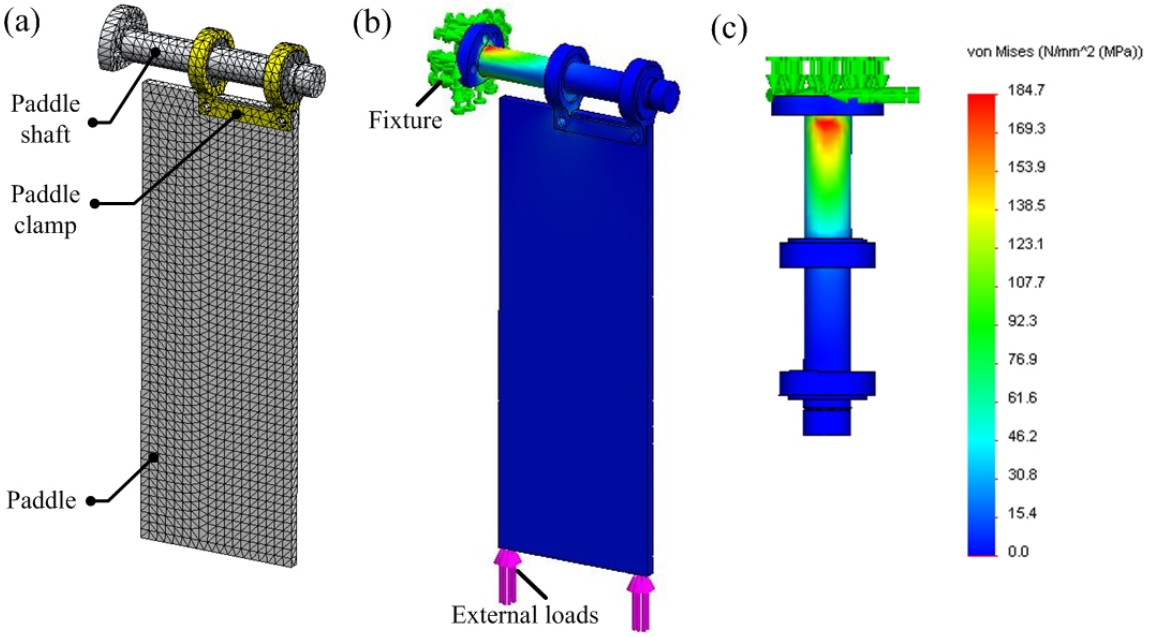

Figure 2.13. Stress analysis on paddle and paddle shaft: (a) created mesh; (b) result of von Mises stress; (c) enlarge view of stresses on paddle shaft.

Table 2.3. MESH DETAILS

Mesh type	Solid mesh
Jacobian points	4
Element size	1.7 mm
Tolerance	0.087 mm
Total nodes	27570
Total elements	15877
Percentage of elements with aspect ratio <3	94.4
Percentage of elements with aspect ratio >10	0.101

2.6 Summary

So far, a complete wheel-paddle robot platform based on the eccentric paddle mechanism has been developed. Introduction about designing the platform has been made from both mechanism and control system. To ensure the effectiveness and robustness in severe environment, special protections have been applied to each crucial part. The safety of the weakest position has been verified through simulation as well. The locomotion performance of the robot platform in various amphibious environment will be studied in the following chapters.

Chapter 3

Trafficability on Rigid Terrain

Amphibious environment is consist of terrestrial and aquatic areas. While robots are performing terrestrial tasks in outside fields, usually they need to work in extreme environment and deal with rough terrains. Common rough terrains may include grass, stones, debris, et al., which substrates are comparatively steady under external stresses, named rigid terrain. Yet there are some special terrains such as sand, snow or mud, which substrates are composed of granular media, called soft terrain. These soft terrains are flowable or deformable under external pressure. Hence, the locomotion performance of robot in such terrains are complex, which will be illustrated in next chapter.

This chapter will first propose a hybrid locomotion mode that is configurable and can be applied in various rough terrains including the rigid terrain and soft terrain. Then, to verify the hybrid mode as well as the new fabricated robot prototype, trafficability of the robot will be evaluated on three rigid rough terrains, which contains grass, gravel and stone. The results on flat floor are given for reference as well. At last, the locomotion performance are discussed and compared with previous gaits and other rough terrain robots.

3.1 Previous Work

Previous work about the locomotion on terrestrial terrain mainly concerns the motion planning of individual wheel-paddle module on flat ground. In [46, 47], a non-reciprocating crawling gait was proposed to avoid the two-directional rotation of the motors so as to increase the transmission accuracy of the planetary gear system. And to increase the locomotion speed and efficiency, a race-walking gait was designed in [48]. However, both the legged gaits were only designed and tested on flat ground and they are sensitive to the unevenness of the terrain. Thus, they can not be directly employed in outside fields. Moreover, the complexity of the motion sequences added on the difficulties of controlling the robot. And three motors working together in a single module is not energetic efficient. Hence, in following of this chapter we will propose a hybrid locomotion mode to deal with the roughness of the ground and tests on the new fabricated robot prototype will be conducted in various fields to verify the effectiveness.

3.2 Motion Generation

The motion generation of the wheel-paddle robot is composed of two levels: the first is at the level of individual wheel-paddle module, and the second level is the collaboration among all the four wheel-paddle modules. The first level explains the motion followed by each individual wheel-paddle module in one period, while the second level establishes a strategy used for generating a gait or pattern among all the modules for the whole robot.

3.2.1 Motion of Individual Module

In order to realize reconfiguration and fast transformation when dealing with various rough terrains, also to improve the locomotion efficiency as much as possible, the hybrid mode was proposed. When the robot performs in hybrid mode, the wheel joint is controlled to rotate continuously so as to generate continuous forward traction forces, while the location of the paddle shaft is only adjusted when the terrain situation changes. In this way, there

is only one motor working in one module at most time during the locomotion. Hence, the control scheme is simplified and the energy consumption will be reduced comparing with the previous legged modes. Through changing the position of the paddle shaft, the contacting situation between the wheel-paddle module and the ground will be altered correspondingly. And different contacting situation will lead to different traction force applying on the robot. As shown in Fig. 3.1(a)-(d), four supporting situations will appear if the eccentric distance of the paddle shaft r_S is increased from $0mm$ to $40mm$. To simplify the control of the robot in primary research, the eccentric angle of the paddle shaft is set constant as $\pi/2$, which means the paddle shaft only moves along the Y-axis. And considering the stability of the robot, the eccentric distance is set as positive to reduce the protruding length of the paddles, implying the paddle shaft moves above the wheel center O.

Fig. 3.1(a) plots the paddle-support stance where only the paddles contact with the ground but the wheel never touches the ground during the locomotion. This situation occurs when the eccentric distance of the paddle shaft is less than a threshold. Fig. 3.1(b) depicts the moment of the wheel just contacting with the ground. Based on the geometric relation in Fig. 3.1(b), the threshold ($r_S = 28mm$) can be calculated through

$$R_W + r_S = l \ \cos\varphi \tag{3.1}$$

where l is the paddle length and φ is the angle between the paddle and Y-axis. If the eccentric distance of the paddle shaft is increased to be larger than that threshold, the wheel-paddle module will be transformed into the hybrid-support stance (as shown in Fig. 3.1(c)). In hybrid-support situation, both the wheel and the paddles contact with the ground during one period of the locomotion. As shown in the figure, the stance transforms between the wheel-support (pale lines) and the paddle-support (bold lines) periodically. When the paddle shaft reaches the maximum eccentric distance or the highest location in the wheel ($r_S = 40mm$), the paddles will be entirely taken back into the wheel when rotating near the ground. In this case, the situation is called wheel-support stance, as shown in Fig. 3.1(d).

In order to obtain the forward locomotion speed of the robot in hybrid mode, stride length (L) by each wheel-paddle module in different supporting situations have been cal-

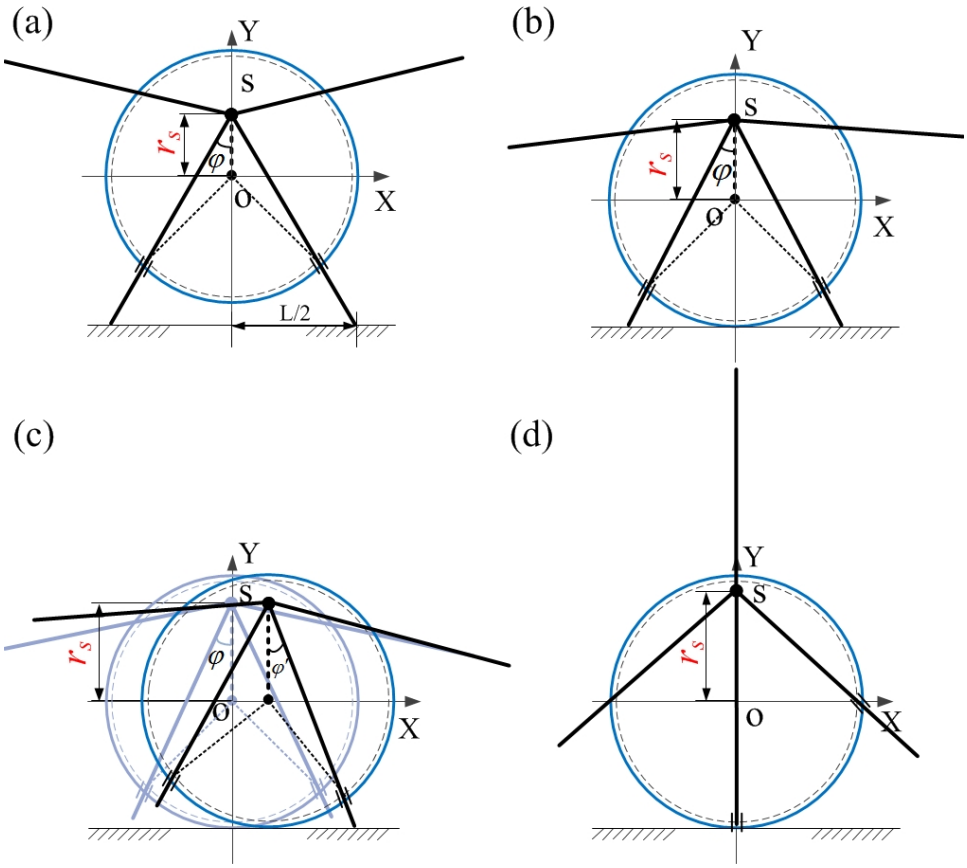

Figure 3.1. Principle of the hybrid mode in schematic drawing: (a) paddle-support; (b)wheel starts contacting with ground; (c) hybrid-support; (d) wheel-support.

culated. The stride length is defined as the distance between two supporting points when the i-th and the $(i+1)$-th paddles contact with the ground. Since there are four paddles in one wheel-paddle module, in one rotational period of the wheel joint, the displacement of the wheel-paddle will be four times of the stride length which is $4L$. Considering there is no paddle contacting with the ground in wheel-support situation, the stride length is calculated as a quarter of the perimeter of the wheel. Consequently, the stride length of the wheel-paddle module in hybrid mode is written as

$$L = \begin{cases} \sqrt{\dfrac{2l^2R_H^2}{r_S^2 + R_H^2 + \sqrt{2}r_S R_H}}, \text{ if } 0 < \mathrm{r_S} \leq 28\mathrm{mm} \\ 2R_W(\pi/4 - \varphi - \arcsin(\dfrac{r_S}{R_H}\sin\varphi')) + 2l\sin\varphi', \text{ if } 28 < \mathrm{r_S} < 40\mathrm{mm} \\ \dfrac{1}{2}\pi R_W, \text{ if } \mathrm{r_S} = 40\mathrm{mm} \end{cases} \tag{3.2}$$

where φ' is the angle between the paddle and Y-axis when the paddle is contacting with the ground in hybrid-support stance. Besides, it is assumed that no slippage occurs between the wheel-paddle and the ground.

3.2.2 Motion of the Robot

In this section, we introduce a two dimensional kinematics of the robot in a plane defined by a global Cartesian coordinate system ($X_G G Y_G$), as shown in Fig. 3.2. For the robot platform, a local coordinate system ($X_L R Y_L$) is defined on it. A general motion of the robot can thus be expressed as

$$q(t) = ((x(t), y(t)), \Psi(t)) \tag{3.3}$$

where the $(x(t), y(t))$ is the position of the origin R in global system at time t and describes the translational motion of the robot. The second term $\Psi(t)$ demonstrates the rotational component of the robot motion. After all, Equation 3.3 describes a three degree-of-freedom motion of the robot in the ground plane. The translational speed $v(t)$, the translational motion orientation $\theta(t)$, and the rotational speed of the robot $\omega(t)$ at time t can then be

calculated through

$$\begin{aligned} v(t) &= \sqrt{x'(t)^2 + y'(t)^2} \\ \theta(t) &= \arctan 2(y'(t), x'(t)) \\ \omega(t) &= \Psi'(t) \end{aligned} \tag{3.4}$$

which describes the incremental motion of the robot. To simplify controlling the locomotion of the robot, a tangential motion was considered and utilized. The tangential motion means the orientation of the translational motion is always along the tangent line of the trajectory curve. As a result, the rotational speed of the robot $\omega(t)$ can also be calculated through

$$\omega(t) = \frac{d\theta(t)}{dt} = \kappa(t) \cdot v(t) \tag{3.5}$$

where $\kappa(t)$ is the curvature of the curve [49]. Based on this simplification, it is found that the tangential motion of the robot could be described in a two degree-of-freedom configuration as

$$Q(t) = (v(t), \theta(t), \frac{d\theta(t)}{dt}) \tag{3.6}$$

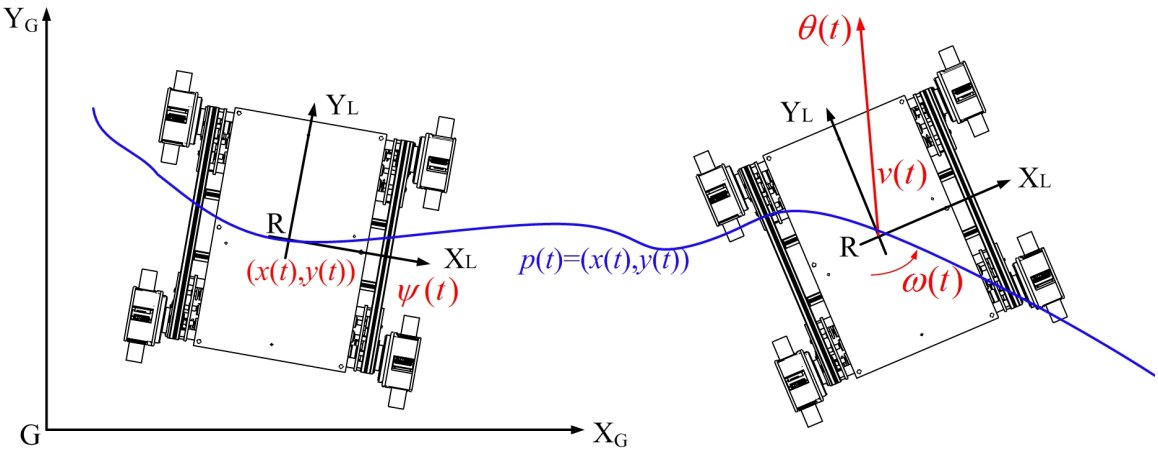

Figure 3.2. Definition of the two dimensional motion of the robot in a plane.

Considering this robot is equipped with fixed wheels, differential skid steering is thus applied. According to [49], there exists a unique relation between the wheel-paddle speeds for a given motion $Q(t)$. As shown in Fig. 3.3, the locomotion speeds of the wheel-paddle

modules on both sides can be derived by

$$\begin{cases} v_1(t) = v(t) - \frac{a}{2} \cdot \omega(t) = (1 - \frac{a}{2} \cdot \kappa(t)) \cdot v(t) \\ v_2(t) = v(t) + \frac{a}{2} \cdot \omega(t) = (1 + \frac{a}{2} \cdot \kappa(t)) \cdot v(t) \end{cases} \tag{3.7}$$

where a is the distance between the left wheels and the right wheels. To be noticed, the wheel-paddles on the same side are actuated with the same forward speed.

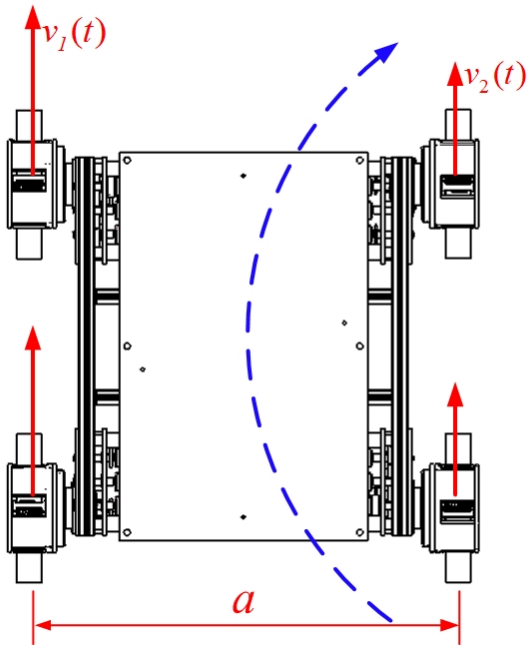

Figure 3.3. Differential steering of the robot.

3.3 Experimental Verification on Rigid Terrains

So far, the robot prototype has been fabricated and the hybrid mode has been proposed for accessing multi-terrain. To verify the design and evaluate the locomotion performance of the robot, experiments were first conducted on rigid terrains with hybrid mode. The rigid terrain in this section will include floor, grass, stones and gravels, which are not as soft or flowable as granular media like sand. And only forward locomotion will be studied. During the experiments, the robot was controlled to go straight at a constant speed. The performance will be evaluated from locomotion speed, vertical vibration and energetic efficiency respectively.

3.3.1 Experimental Environment

The experimental environment and the setup are as shown in Fig. 3.4. The main control PC sends commands to the robot to adjust the eccentric distance of the paddle shaft and the forward locomotion speed. To obtain the position and orientation of the robot in real-time, a Kinect Box (Microsoft, USA) was assembled on the top of the robot body. The six degree-of-freedom motion information were recorded by the assist PC. During the experiments, a camera was utilized to log the locomotion process for reference as well.

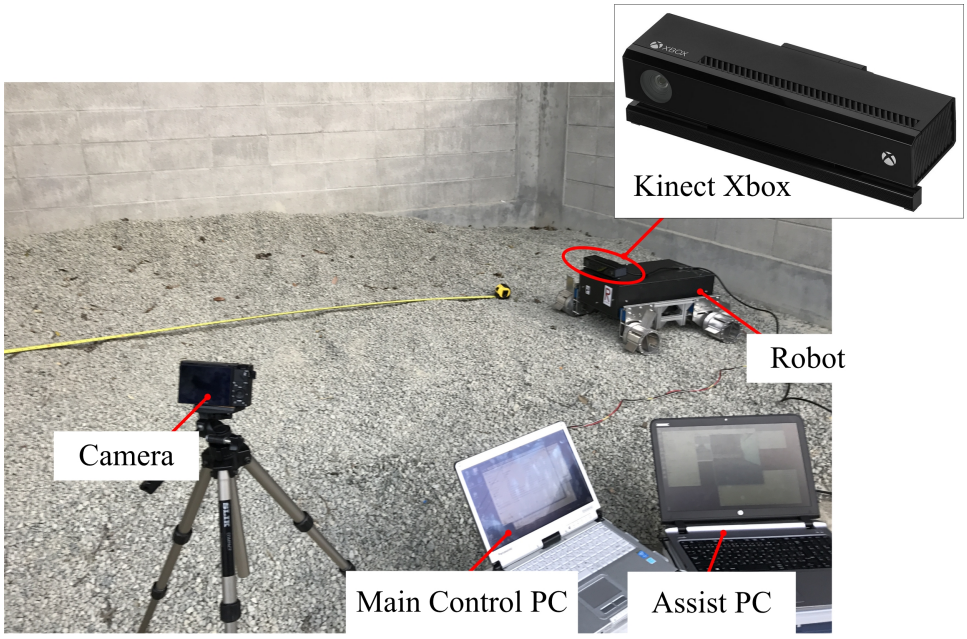

Figure 3.4. Experimental setup for evaluating locomotion performance of the robot on rough terrains.

To compare the trafficability of the robot on different rigid terrains, one indoor and three outdoor terrains were chosen as the experimental sites, as seen in Fig. 3.5. Fig. 3.5(a) shows the robot on indoor flat ground, which is located at the second floor of East Wing, Ritsumeikan University (BKC). Fig. 3.5(b) shows the grass terrain nearby the East Wing. Due to the weakness of the grass substrate, sinkage can happen to the robot. And the terrain is not guaranteed to be horizontal or flat. Even so, experiments were conducted repeatedly to average the results. And it also allows us to study the rough terrain negotiability of the wheel-paddle robot with hybrid mode. Fig. 3.5(c) shows the terrain with stones which

average diameter is near $20mm$. While in Fig. 3.5(d), the average diameter of the gravels is $5mm$.

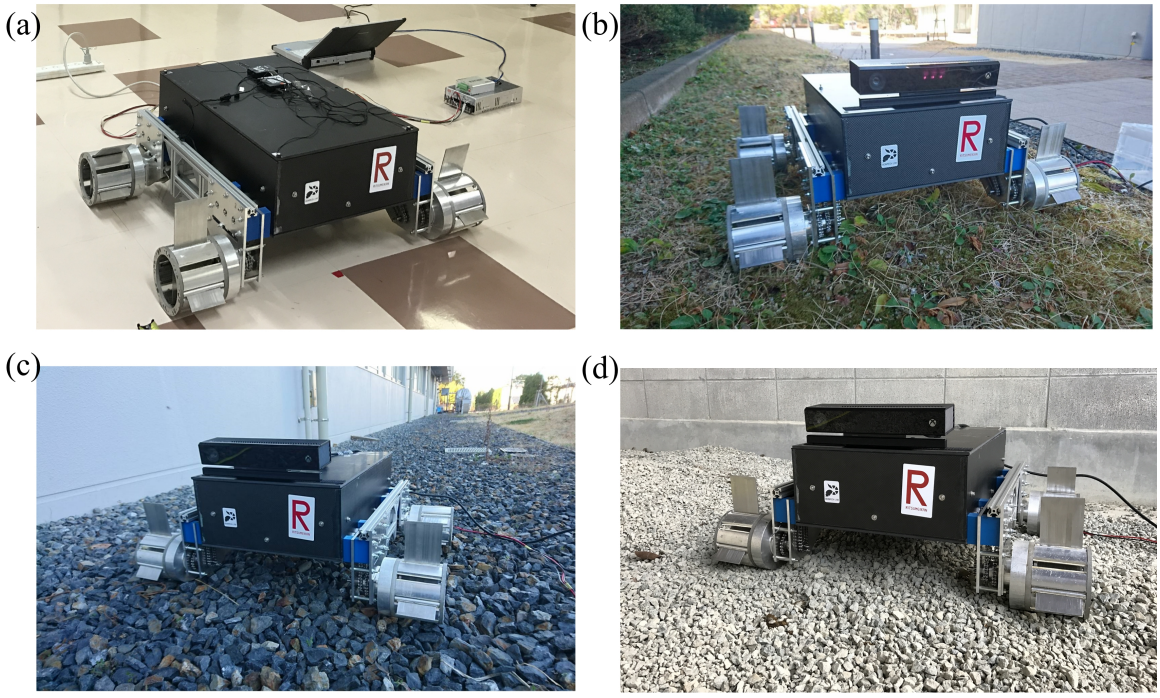

Figure 3.5. Tested indoor and outdoor rigid terrains: (a) indoor floor; (b) grass; (c) stones with average diameter of $20mm$; (d) gravels with average average diameter of $5mm$.

3.3.2 Results Analysis

A. Flat Floor

The experimental results of floor locomotion in hybrid mode are shown in Fig. 3.6. The eccentric distance of the paddle shaft was set as $40mm$, corresponding to the wheel-support configuration. During the tests, the robot was controlled to follow five different constant forward speeds. The displacements changing along with the time are shown in Fig. 3.6(a), where data in five seconds are depicted. The vibration of the robot in the vertical direction was also recorded and the results in one trial are shown in Fig. 3.6(b). The vibration is almost zero in all tests due to the wheel-support configuration. The current consumption of one wheel-paddle module in different locomotion speeds are also shown in Fig. 3.6(c). Along with the speed goes up, the current increases slowly and reaches the highest at the

speed of $0.4m/s$. But generally the current did not change too much. To inspect the current consumption in all four modules, the current of four modules in $0.3m/s$ are shown in Fig. 3.6(d). The letters "FL" indicate the module at the front left of the robot, while "HR" is the hind right module, "FR" is the front right and "HL" is hind left. It is found that the currents generated by the left side modules are a litter smaller than the right side ones, which may be caused by the unbalanced load of the robot body.

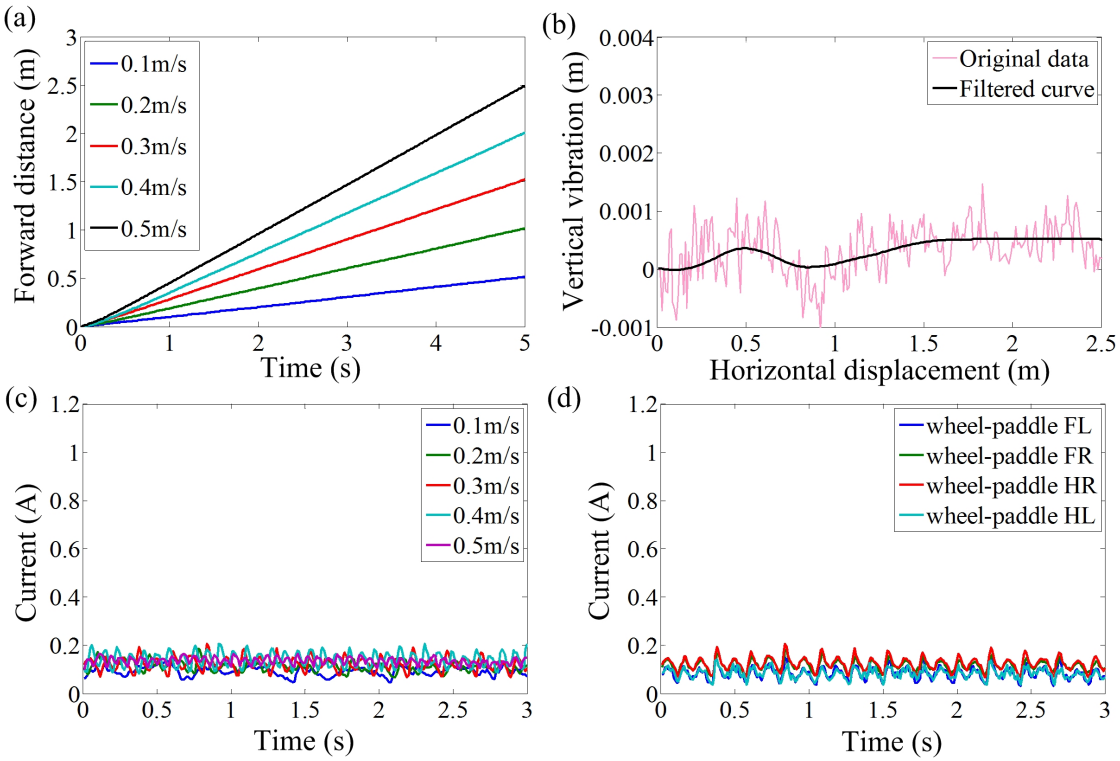

Figure 3.6. Results of floor tests in wheel-support configuration: (a) forward speeds; (b) vertical vibration of the robot; (3) current consumption in different locomotion speeds; (d) currents in four modules of the robot at forward speed of $0.3m/s$.

B. Grass Land

To evaluate the locomotion performance on rough terrain like grass land, the robot was adjusted to hybrid-support configuration. In primary tests, the eccentric distance of the paddle shaft was set to $30mm$. The displacement of the robot at various actuating speeds are shown in Fig. 3.7(a). Different with the data in floor tests, the curves are not absolutely smooth due to the roughness of the grass land. The vertical vibration was also

measured and shown in Fig. 3.7(b). It was found that the vibration was small because the sinkage happens to the robot due to the weakness of the grass substrate, which lead to a comparatively stable locomotion. The variance in the vertical displacement was caused by the unevenness of the terrain. The current consumption at different locomotion speeds and by different modules are shown in Fig. 3.7(c)(d) respectively. Comparing with the currents in floor tests, the values are a little larger. But due to the roughness of the terrain, the currents are difficult to find the rules. It is seen that when the locomotion speed goes up, the current does not change too much.

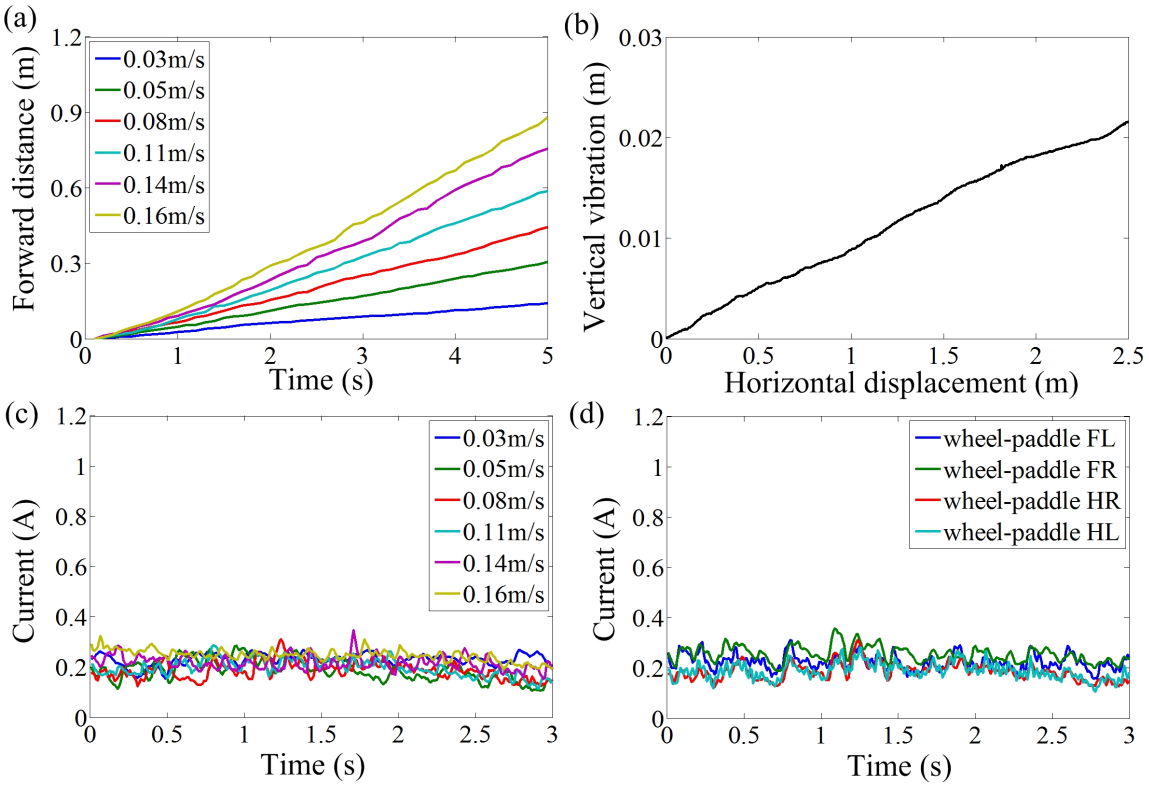

Figure 3.7. Results of grass land tests in hybrid-support configuration: (a) forward speeds; (b) vertical vibration of the robot; (3) current consumption in different locomotion speeds; (d) currents in four modules of the robot at forward speed of $0.08m/s$.

C. Stones

The results from tests on stones can be found in Fig. 3.8. The data of forward distance in Fig. 3.8(a) are not as smooth as floor tests and grass tests, which means it is more difficult

to follow a constant locomotion speed on a rougher terrain situation. The vertical vibration showing in Fig. 3.8(b) also proved that. It is seen that the vibration is larger comparing with the grass locomotion. As for the current during the locomotion, it is cluttered during the roughness of the terrain. Generally, we can find the largest current occurs at $0.11m/s$. The average current will be calculated for further analysis in the next section.

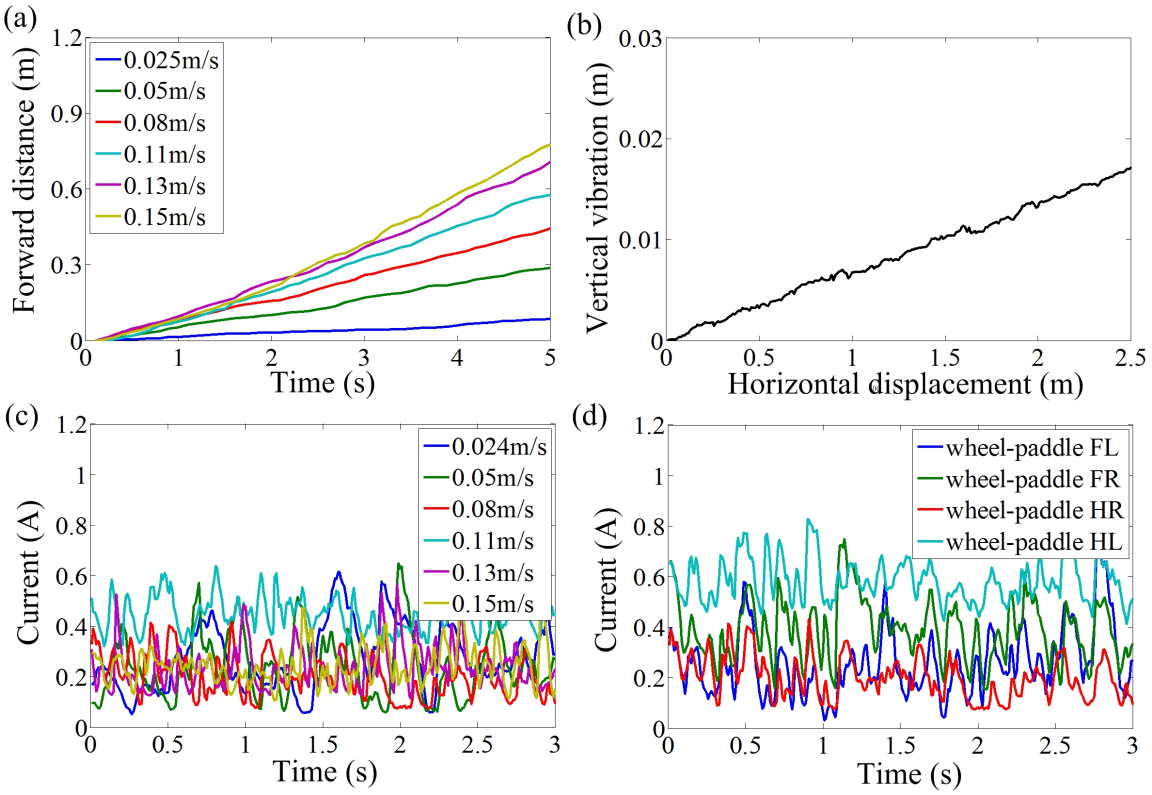

Figure 3.8. Results of stone tests in hybrid-support configuration: (a) forward speeds; (b) vertical vibration of the robot; (3) current consumption in different locomotion speeds; (d) currents in four modules of the robot at forward speed of $0.08m/s$.

D. Gravels

The experiment was also conducted in gravels, which consist of smaller stones comparing with the previous section in big stones. The behavior of the robot was found different in these two terrains. During the locomotion on stones, the paddles seldom insert into the stones deeply and the stone substrate does not change a lot. While in gravels, the paddles insert into the gravels and interact with them in a more complicate way. Due to the small

mass of each gravel, the substrate also changes sometime. The sinkage of the paddle reduced the system vibration but also increased the resistance of going forward. The currents shown in Fig. 3.9(c)(d) are much larger than on the stones.

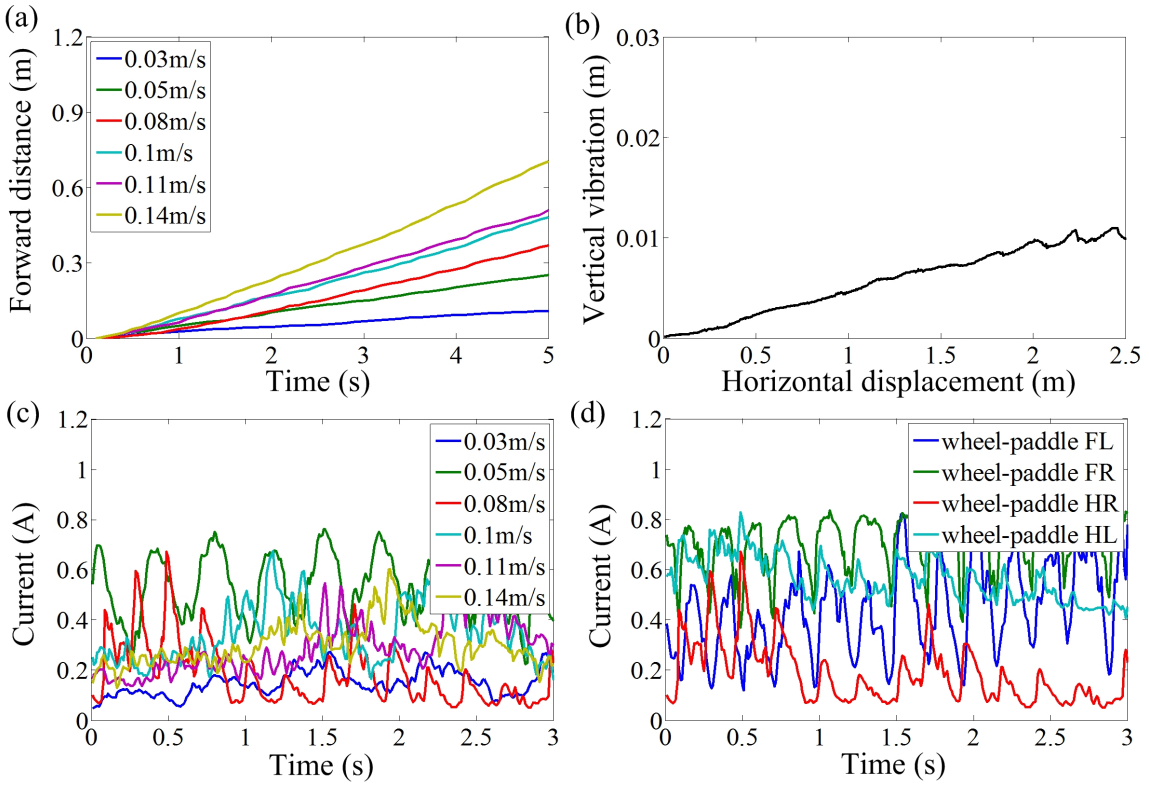

Figure 3.9. Results of gravel tests in hybrid-support configuration: (a) forward speeds; (b) vertical vibration of the robot; (3) current consumption in different locomotion speeds; (d) currents in four modules of the robot at forward speed of $0.08m/s$.

3.3.3 Energetic Efficiency

The previous section has introduced results directly obtained from the feedbacks of the system. To evaluate the locomotion efficiency in different terrains, specific resistance (SR) [50] was was used and it is defined by

$$SR = \frac{P}{mgv} \tag{3.8}$$

where P indicates the power consumption by the whole robot, v is the locomotion speed, m is the mass of the prototype and g is the acceleration of gravity. Both the power P

and speed v are averaged during the calculation. The power consumption by the robot at different locomotion speeds are depicted in Fig. 3.10(a). It is found that the power consumption almost increases linearly with the locomotion speed going up. And it consumes more energy in rough terrains than on flat floor. As for the specific resistance, the results are shown in Fig. 3.10(b). The larger values of specific resistance indicates less efficiency of the locomotion. It is seen that the floor locomotion is the most efficiency. While the locomotion in gravels tends to be the most inefficient among all the rough terrains.

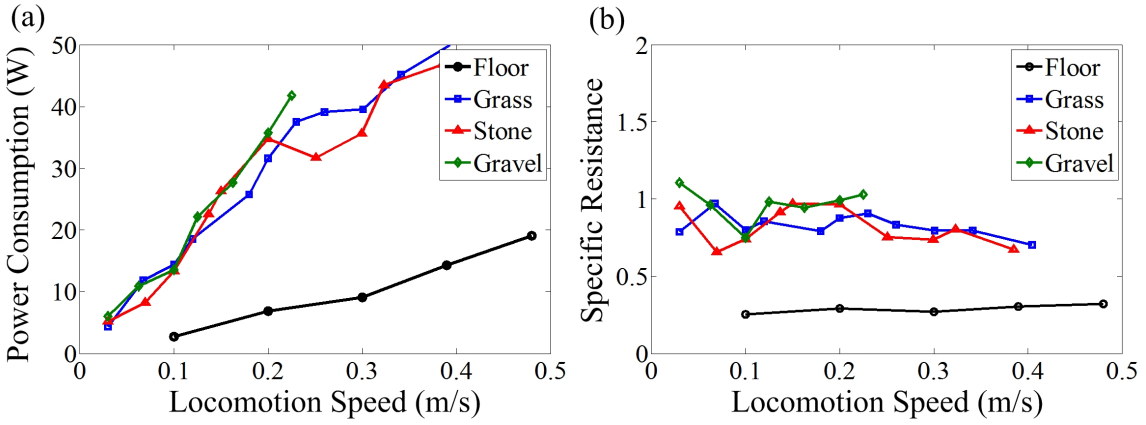

Figure 3.10. (a) Power consumption; and (b) specific resistance of the robot traversing rough terrains at different locomotion speed with the hybrid mode.

3.4 Discussion

This chapter first introduced the previous work about gait planning. But considering the application of the robot in rough terrain, we proposed the hybrid mode and analyzed the robot kinematics as well. The advantage of the hybrid mode is its fast and simple reconfigurability among different support stances, which is necessary to deal with variable terrain situations. For example, the wheel-support configuration is suitable for fast and efficient locomotion on flat ground. While in rough terrains such as stones, the protruding paddles may make up with the unevenness and increase the traction force, so as to increase the locomotion efficiency. This effect of the protruding paddles should be more prominent in the granular media like sand, which will be illustrated in the next chapter. Hence,

this chapter preliminarily tested the hybrid mode on four rigid terrains and evaluated the locomotion speed, vibration and the energy efficiency. To compare the locomotion efficiency with the previous gaits as well as the other mobile robots, we depicted the range of the specific resistance in Fig. 3.11 [45]. The black lines indicate other robots, while the blues lines are our previous gaits, and the red lines are the results of hybrid mode. Due to the large difference between the flat floor locomotion and rough terrain locomotion, we separate the results into two lines. It is found that hybrid locomotion on flat floor is the most efficient and the fastest in our study. The non-reciprocating legged gait is more efficient than the hybrid mode on rough terrain. However, it can only be applied to flat ground and also the speed can not reach as fast as the hybrid mode. As for the crawling gait, the efficiency is almost same with the hybrid mode. Only the locomotion speed is also much slower than the hybrid mode. The slow locomotion speed of both crawling gait and non-reciprocating gait is due to the complicate control of the motion in the eccentric paddle mechanism, which limited the gait frequency so as to the locomotion speed. This is also the reason we utilized the hybrid mode, where only one motor is actuated in one wheel-paddle module during the locomotion, the other two motors are only actuated when transforming among different support stances.

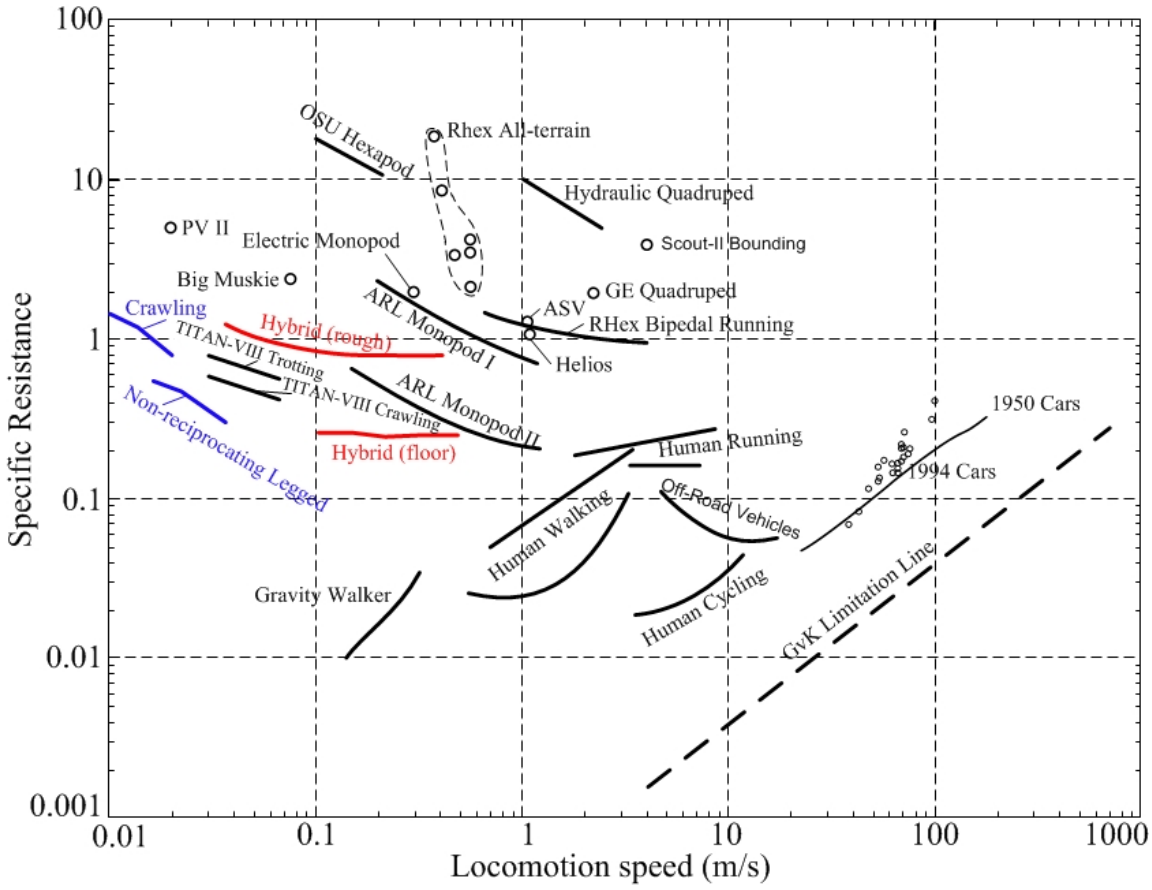

Figure 3.11. Specific resistance of the new robot with hybrid mode (red lines), previous legged gaits(blue lines), and other mobile robot [45]. © 2018 IEEE.

Chapter 4

Trafficability on Soft Terrain

4.1 Introduction

The trafficability of the robot on rigid terrains has been inspected in the previous chapter. However, the rough terrain that the robot needs to deal with include not only the rigid ones but also the soft ones, such as the granular media. The difference is that the substrate of the rigid terrains (floor, grass, gravel, stones, etc.) is not flowable, while the granular media (also named soft substrate in some research) is deformable and flowable under external forces. It is defined as collections of discrete particles which behaves between solid and fluid [14, 15, 16], such as sand, soil, mud, snow, etc.. Moreover, the granular media can be categorized into dry granular media and wet granular media according to the water content of the media. The prominent difference between them is whether cohesion exists.

Currently in our research, we focus on the locomotion of the robot on dry granular media, where the granular particles interact purely through dissipative, repulsive contact forces without cohesion [17]. Due to the wide existence of such granular media on our earth, it is important for a field robot to access it effectively so as to be applied to the real environment. Based on the study of the locomotion on rigid terrain, this chapter discusses the trafficability of the wheel-paddle integrated robot over soft terrain (sand) while conducting the hybrid mode. To be detailedly, first the paddle terradynamics will be

modeled to explore the interaction between the paddles and the soft terrain; based on the theoretical results, an indoor testbed is built and the experiment will be conducted with one wheel-paddle module to verify the interaction as well as the motion; at last the robot will be controlled to traverse real sand in outdoor field and the results will be analyzed.

4.2 Paddle Terradynamics

To traverse soft terrain, the hybrid mode proposed in Sec. 3.2.1 will be remained utilizing due to its flexibility and adaptability in various terrain situations. But on account of the flowability of the granular media, the interaction between the robot and the substrate is more complex compared with the rigid ground. To figure out the optimal configuration of the wheel-paddle for accessing soft terrain, the paddle terradynamics will be first introduced in this section. In both theoretical and experimental analysis, a kind of sand with the properties listed in Table. 4.1 was considered (name Sand I).

Table 4.1. PHYSICAL PROPERTIES OF THE STUDIED SAND I

Description	**Value**	**Unit**
Cohesion stress	400	Pa
Friction angle	38.1	deg
Density	1480	kg/m^3
Scaling factor α_z	1.1	N/cm^3

4.2.1 Modeling

Fig. 4.1(a) shows the schematic drawing of the situation we are discussing. For simplification, only the wheel with wheel center O and radius R_W and one paddle with the paddle shaft S and whole paddle length l are depicted. Comparing with the propelling force that the paddles can generate, the drawbar pull of the wheel is very small. Besides, the interaction between the wheel-paddle and the sand becomes complicate due to the squeeze by two adjacent paddles. Hence, we assume the sinkage of the wheel is zero which means

the wheel just contacts with the sand surface and does not generate effective propelling or resistive forces. We only study the terradynamic force generated by the paddle with different protruding lengths.

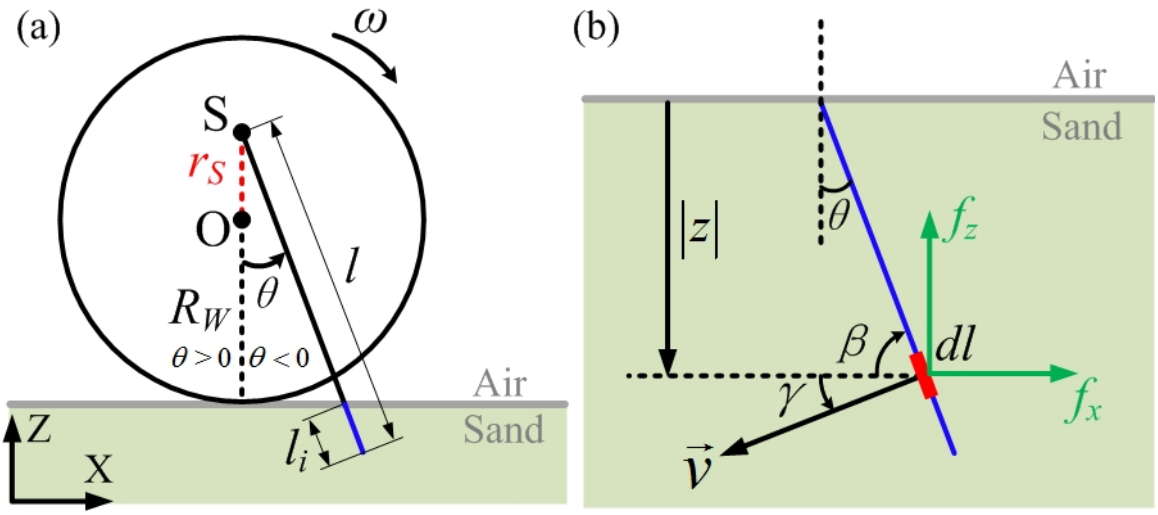

Figure 4.1. Experimental setup for measuring thrust.

The protruding length means the part of the paddle outside the wheel, which is determined by the eccentric distance of the paddle shaft. While the effective length that can generate terradynamic force is the inserting part of the paddle in the sand. The inserting length of the paddle is depicted in blue line in Fig. 4.1(a) and described by l_i. The exact inserting length can be calculated through geometric relations as

$$l_i = l - \frac{r_S + R_W}{\cos\theta} \tag{4.1}$$

where r_S is the eccentric distance of the paddle shaft S away from the wheel center O and defined as positive if the location of S is above O, negative if S is below O. R_W is the radius of the wheel, and θ is the angle between the paddle and the central line. An enlarged view of the inserting paddle is shown in Fig. 4.1(b). The terradynamics proposed in [19] proved that the interface stresses $\sigma_{x,z}$ on a unit paddle segment dl are independent on the moving speed when it is slow, but proportional to the depth of the segment ($|z|$). And the gains of the stress $\alpha_{x,z}$ have an exact functional relation with the attack angle β and the intrusion angle γ of the paddle. The function was parameterized with the discrete Fourier transform

(DFT) coefficient in [19], following

$$\begin{cases} \alpha_z(\beta,\gamma) = \sum_{p=-1}^{1}\sum_{q=0}^{1}[A_{p,q}\cos 2\pi(\frac{p\beta}{\pi}+\frac{q\gamma}{2\pi}) + B_{p,q}\sin 2\pi(\frac{p\beta}{\pi}+\frac{q\gamma}{2\pi})] \\ \alpha_x(\beta,\gamma) = \sum_{p=-1}^{1}\sum_{q=0}^{1}[C_{p,q}\cos 2\pi(\frac{p\beta}{\pi}+\frac{q\gamma}{2\pi}) + D_{p,q}\sin 2\pi(\frac{p\beta}{\pi}+\frac{q\gamma}{2\pi})] \end{cases} \tag{4.2}$$

where the DFT coefficients ($A_{p,q}$, $B_{p,q}$, $C_{p,q}$, $D_{p,q}$) are nine terms of the zeroth and first orders that can be written into vector $\vec{M}$ as

$$\vec{M} = (A_{0,0}\ A_{1,0}\ B_{1,1}\ B_{0,1}\ B_{-1,1}\ C_{1,1}\ C_{0,1}\ C_{-1,1}\ D_{1,0})^T \tag{4.3}$$

Vector $\vec{M}$ is the result of multiplying a generalized DFT coefficient vector $\vec{M}_0$ by a scaling factor χ, expressed as

$$\vec{M} = \chi\vec{M}_0 \tag{4.4}$$

where the scaling factor χ is the vertical stress gain that can be obtained through pushing a horizontal ($\beta = 0$) plate vertically down ($\gamma = \pi/2$) into the sand, denoted as $\alpha_z(0, \pi/2)$. And the generalized vector $\vec{M}_0$ has been obtained in [19]:

$$\vec{M}_0 = (0.21\ 0.17\ 0.21\ 0.36\ 0.06\ -0.12\ 0.25\ 0.01\ 0.09)^T \tag{4.5}$$

After calculating the stress gains $\alpha_{x,z}(\beta,\gamma)$ and knowing the depth of segment dl, the stresses can be achieved by directly multiplying the stress gains with the depth:

$$\sigma_{z,x}(\beta,\gamma,z) = \alpha_{z,x}(\beta,\gamma)|z| \tag{4.6}$$

The details of the derivation can be found in [19]. Given the stresses on each paddle segment, the total interaction forces $F_{z,x}$ can be approximated through liner superposition:

$$F_{z,x} = \int_{\Omega} \sigma_{z,x}(\beta,\gamma,z)ds \tag{4.7}$$

where ds is the surface area of a single paddle segment and Ω is the whole area of the inserted paddle l_i. The interaction forces are generated from the paddle starting to insert the sand to it completely pulling out of the sand surface. To evaluate the effective net

thrust during one operation period, the instantaneous interaction forces $F_{z,x}$ are integrated by differential angle element dθ as

$$N_{z,x} = \int_{\Theta} F_{z,x} d\theta \tag{4.8}$$

where θ is the angle between the paddle and z-axis as denoted in Fig. 4.1. Θ indicates the angle range of effective interaction.

To be specifically, the moment the paddle starts to insert in the sand is shown in Fig. 4.2(a). θ_0 denotes the inserting angle and hence there exists $\Theta = [\theta_0, -\theta_0](\theta_0 \leq 0)$. When the paddle reaches the vertical position as depicted in dotted line in the figure, the inserting length of the paddle is the deepest and the length is described by l_{imax}. It is fond that both the inserting angle θ_0 and the maximum inserting length l_{imax} are dependent on the eccentric distance of the paddle shaft r_S. The dependence is calculated and shown in Fig. 4.2(b). It can be found that large eccentric distance results in small inserting angle and maximum insertion depth of the paddle.

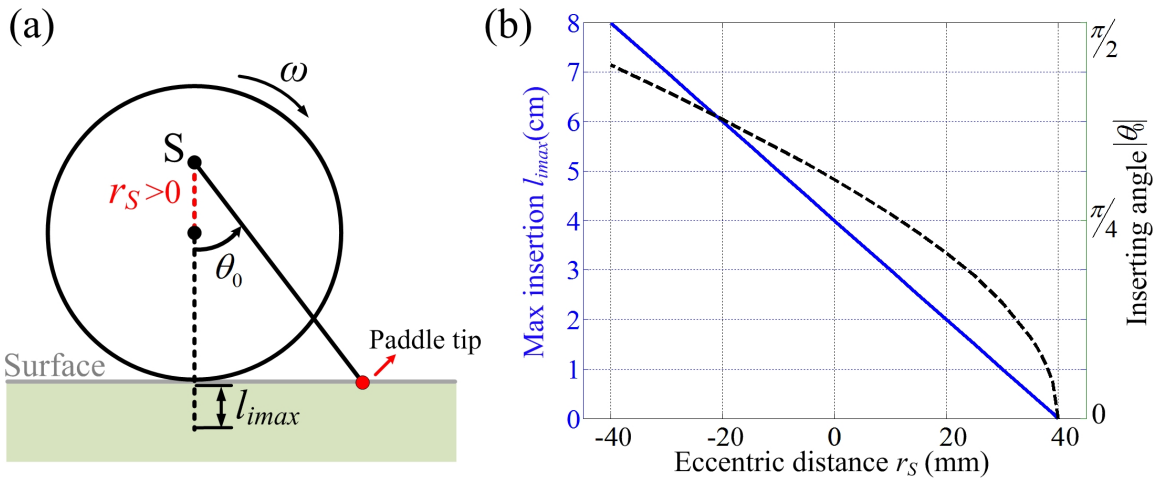

Figure 4.2. Kinematic analysis: (a) definition of inserting angle and maximum insertion depth of the paddle; (b) dependence of the inserting angle and maximum insertion depth on the eccentric distance of the paddle shaft.

4.2.2 Simulation

Based on the built terradynamic model and the kinematics analysis, the predicted interaction force between the paddle and the sand was calculated. The results with different eccentric distances are depicted in Fig. 4.3. It is seen that the configuration with small eccentric distance or long protruding length can generate larger thrusts in both horizontal and vertical directions. The direction of the thrust in the horizontal axis is always positive, while there exists both positive and negative forces in the vertical direction. According to the angular position of the paddle θ, we can tell that positive forces are generated during the insertion phase and the negative forces are generated during the extraction phase. Moreover, the magnitude of positive force is larger than the negative force, which means it is more difficult to insert the paddle into the sand than to extract it. Through the figure we can also find that the forces in both directions are not symmetric about the median position $\theta = 0$. This may be caused by the gravity effect [19].

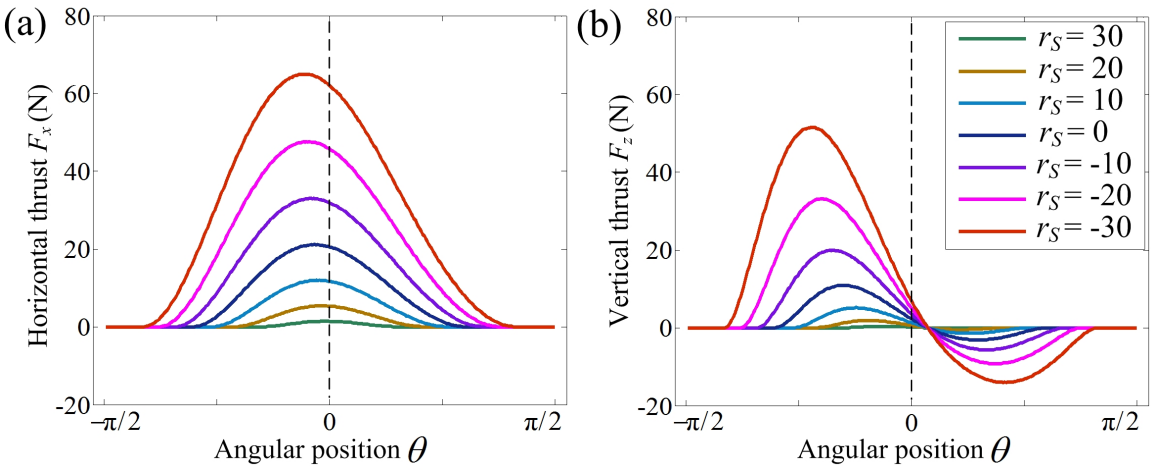

Figure 4.3. simulated terradynamic forces generated by the paddle with various eccentric distances.

4.2.3 Experimental Verification

In order to verify the terradynamic model as well as the simulation results, an thrust measuring experimental setup was constructed as shown in Fig. 4.4. The wheel-paddle

module was controlled by one MCU unit as introduced in Section. 2.4. A 6-axis force sensor was applied to connect the tested wheel-paddle module with a mounted plate. The generated sand thrust was recorded by Arduino and the data was sent to the main controlling laptop. During the experiment, the wheel-paddle module was first regulated to the wheel rim just contacting with the sand surface. And then the paddle shaft was located at the exact eccentric distance from the wheel center. In all trials, the wheel joint was controlled to rotate at a constant velocity of 10 deg/s. To reduce the random errors in the measured forces, each trial was conducted five times and the results were averaged.

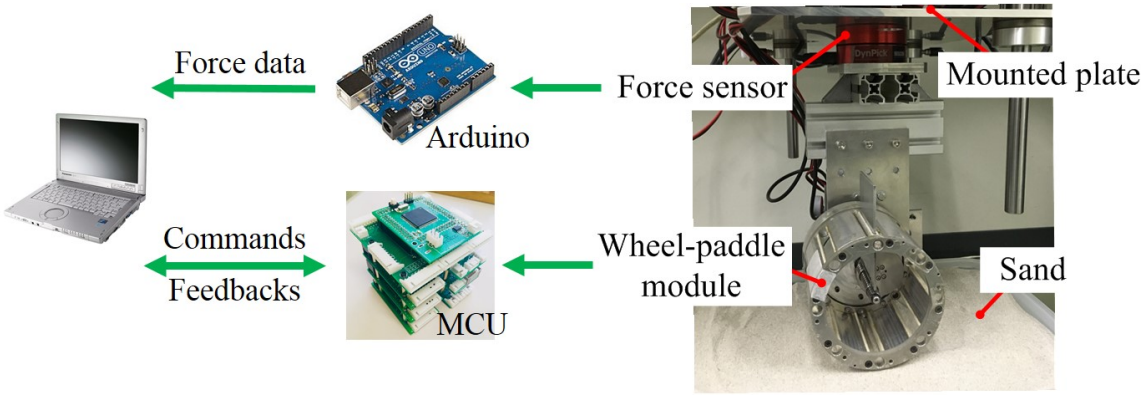

Figure 4.4. Sand thrust measuring setup.

The experimental results are shown in Fig. 4.5. To verify the terradynamic model, both the simulated results and the measured results are depicted. Considering the real application of the hybrid mode, results of four configurations with nonnegative eccentric distances ($r_S \geq 0$) are shown in the figure. It is found that the terradynamic model can almost predict the interaction force accurately in each configuration. And it is proved that the thrusts do increase with smaller eccentric distance or longer protruding length of the paddle. However, while generating larger propelling thrust in the horizontal direction, the vertical interaction force is increasing as well, which may lead to large vibration to the whole system.

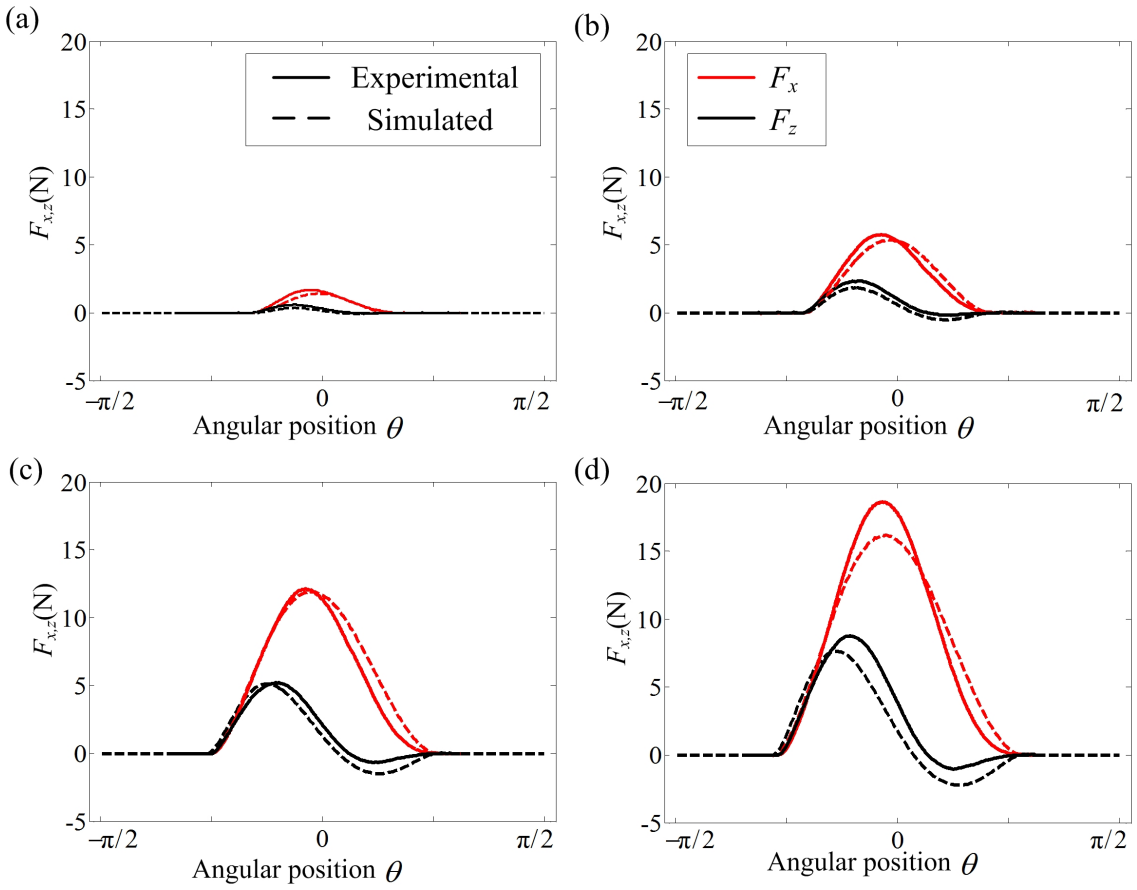

Figure 4.5. Terradynamic forces generated by the wheel-paddle module with different eccentric distance of the paddle shaft.

4.3 One-module Free Walking

Based on the paddle terradynamics, it has been found that large protruding length of the paddle or small eccentric distance of the paddle shaft can generate great terradynamic forces. However, the locomotion performance resulting from the terradynamic forces are still unknown, which is important for evaluating a robotic system. Hence in this section, indoor free walking tests will be conducted with one wheel-paddle module and the performance of the locomotion will be evaluated.

4.3.1 Experimental Setup

To realize free walking of one wheel-paddle module and test the mobility, an indoor platform was built as shown in Fig. 4.6. Fig. 4.6(a) shows the overall layout of the whole experimental environment, which consists of a testbed allowing the wheel-paddle module to walk freely, a power source for the robotic system, a main controlling PC, a logging camera and a motion capture system. The motion capture system (VZ4050, PTI, Canada) is used to obtain the real time position of the wheel-paddle module. The details of the testbed are shown in Fig. 4.6(b). The foundation of the testbed is based on aluminum frames assembling together. Two horizontal sliding guides and three vertical sliding guides allow the wheel-paddle module to move freely in the two directions. One MCU controls the wheel-paddle module to move in a sand box with the size of $1150 \times 600 \times 200mm$. A marker was fixed with the wheel-paddle module so that the motion capture system can track the motion of the marker. To describe the inertia of the system, totally the mass that can mover vertically along the vertical guides is $4.3kg$, which includes the wheel-paddle module and the MCU. And the mass that can mover horizontally along the horizontal guides is 6.7 kg, containing the wheel-paddle module, the MCU, three vertical guides, and all the slide blocks on the sliding guides.

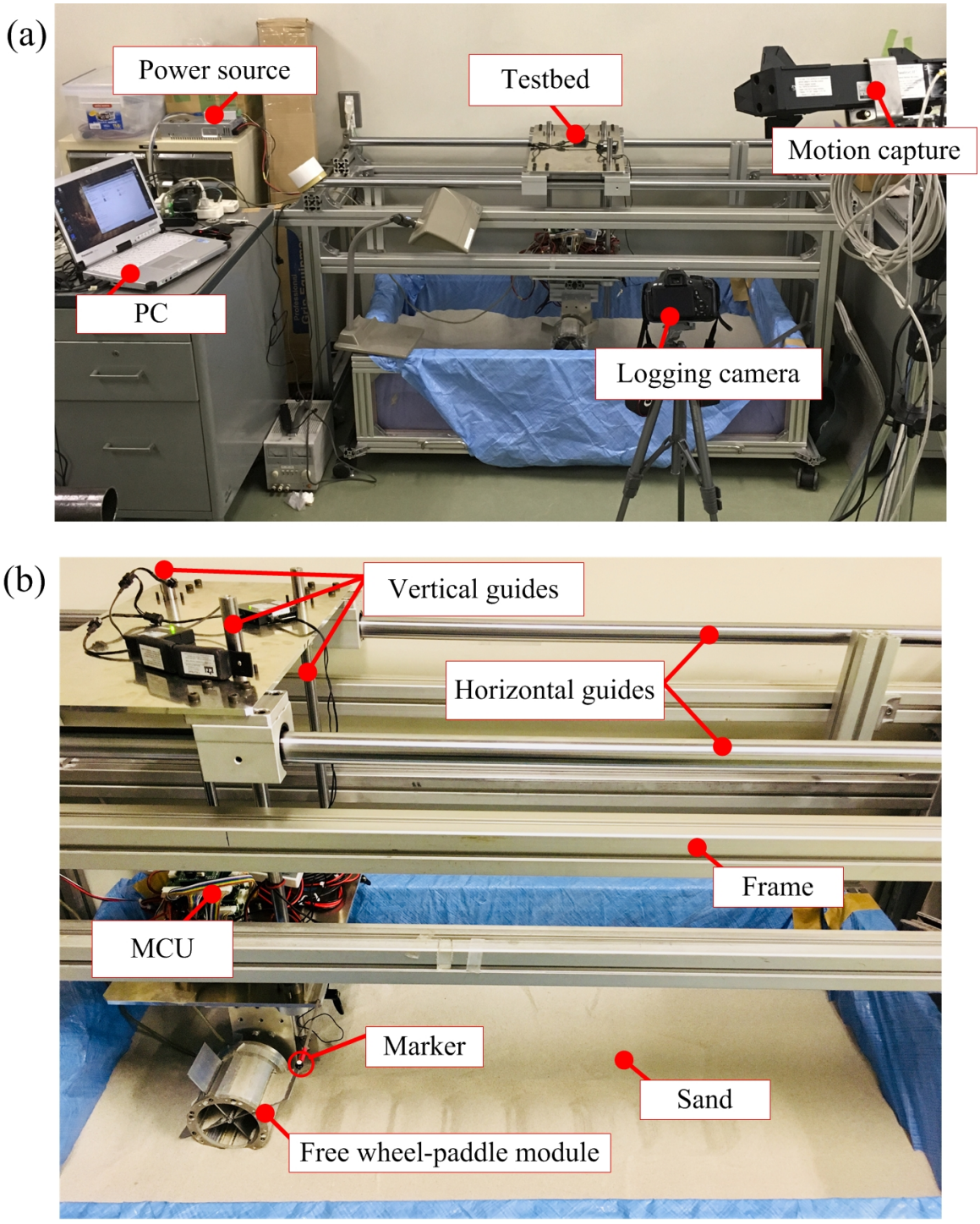

Figure 4.6. Indoor free-walking experimental platform: (a) overall layout; (b) 2-DoF free-walking testbed design.

4.3.2 Design of Experiment

To explore the locomotion performance of the module under different situations, the free-walking tests are designed as shown in Table. 4.2. In addition to the eccentric distance, angular velocity of the wheel was also varied to explore the motion. The directly recorded parameters during the experiments include the horizontal locomotion speed, the height variation, the motor torque and the rotational speed of the motor. The motion capture system works at a sampling frequency of $100Hz$. Before each trial, we used a claw to homogenize the sand and a gradienter to calibrate the height level. All the trials were conducted five times to reduce the random error.

Table 4.2. VARIABLES DURING THE TESTS

Inputs	Angular velocity ω (rad/s)	0.75, 1.5, 2.25, 3, 3.75, 4.5
	Eccentric distance r_S (mm)	40, 30, 20, 10, 0
Outputs	Speed, height variation, motor torque, motor rpm	

4.3.3 Results Analysis

A. Traversing Speed

The traversing speed of the wheel-paddle module in the forward direction or horizontal direction is analyzed based on the data recorded by the motion capture system. Fig. 4.7 shows both the velocity and the displacement of the module in horizontal direction with different rotational speed of the wheel joint. The configuration is wheel-support in this figure which means the eccentric distance of the paddle shaft is $40mm$. Each subgraph shows the motion data in five seconds of one trial. It is easy to find that the traversing speed almost increases with the actuating velocity ω increasing. Only when the actuating velocity adds from $\omega = 3.75rad/s$ to $\omega = 4.5rad/s$, the traversing speed decreased, which could be caused by the slippage happening between the wheel and the sand. It means the wheel-only support configuration is easy to slip at high locomotion speed.

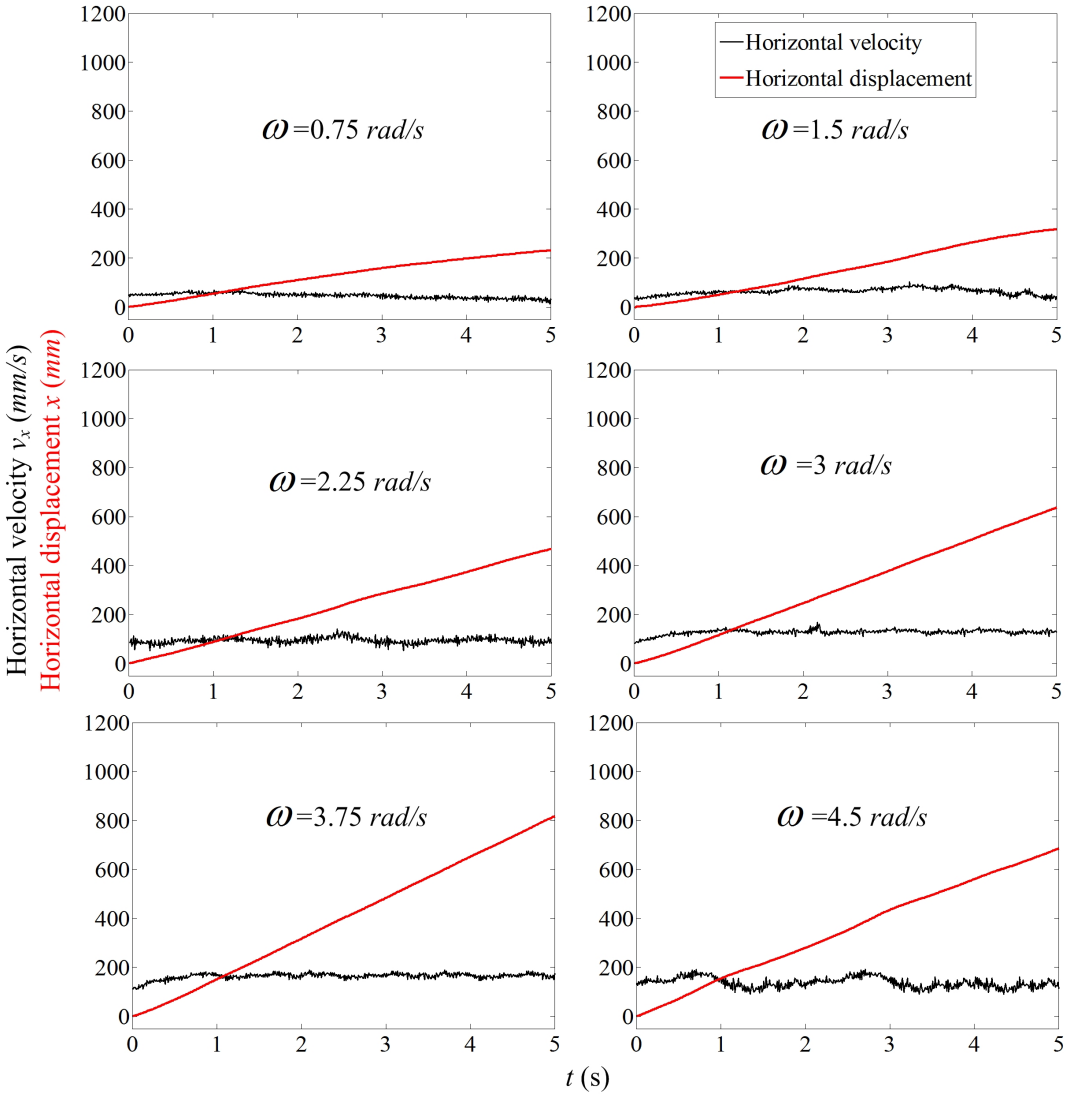

Figure 4.7. Horizontal velocity v_x and displacement x under different actuating rotational speeds of the wheel joint when $r_S = 40mm$.

To give a comparison with the wheel-support configuration, Fig. 4.8 shows the results of paddle-support configuration $r_S = 0mm$. First we found that the forward velocity v_x is not constant due to the paddle supporting situation. And at high speeds comparing $\omega = 3.75rad/s$ with $\omega = 4.5rad/s$, the velocity did not decrease as happened in the wheel-support configuration. Besides, the average traversing speed (reflecting from the maximum values of red lines) in each actuating velocity ω of paddle-support (Fig. 4.8) is larger than the wheel-support (Fig. 4.7).

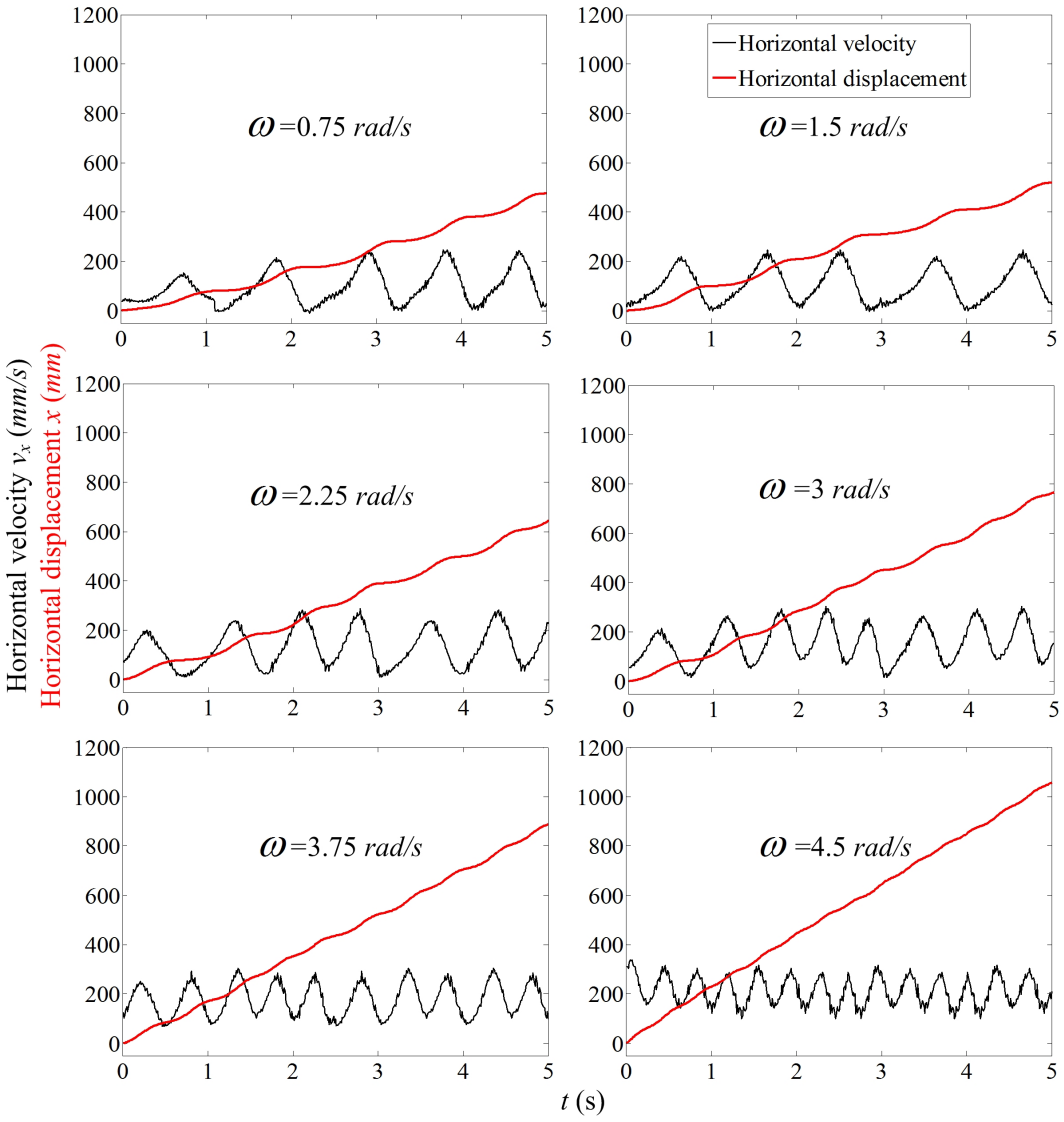

Figure 4.8. Horizontal velocity v_x and displacement x under different actuating rotational speeds of the wheel joint when $r_S = 0mm$.

In order to compare directly between the wheel-support and paddle-support configura-

tions, the forward displacements of both cases with various actuating velocities are depicted together as shown in Fig. 4.9. It is clear to see that the slippage happens to the high speed locomotion at wheel-support configuration. And the paddle-support configuration not only avoided the slippage at high speeds but also increased the overall traversing speeds.

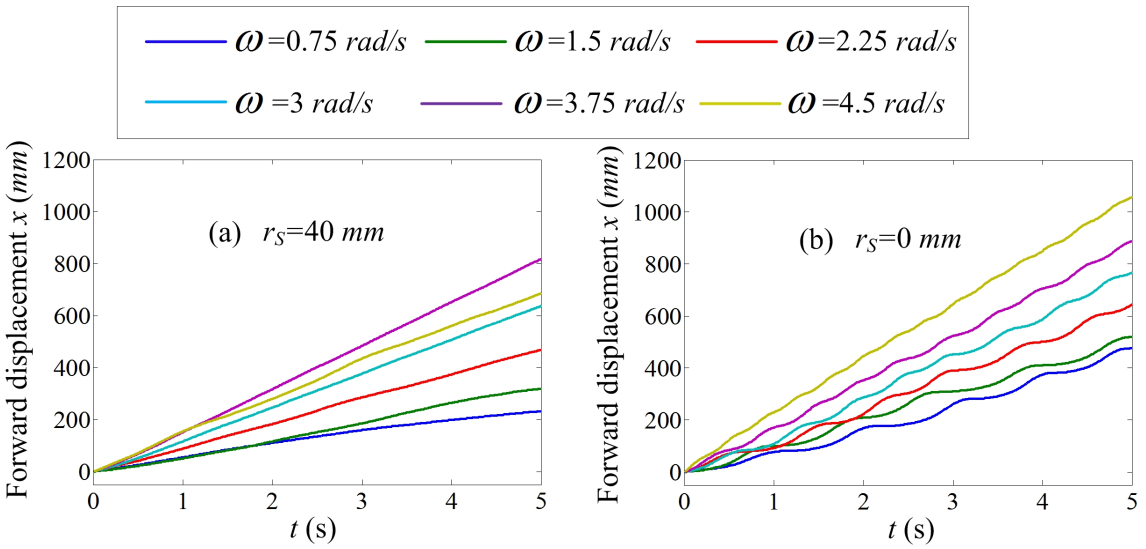

Figure 4.9. Forward locomotion with different configurations and rotational speeds: (a) $r_S = 40mm$; (b) $r_S = 0mm$.

However, these results are only from two individual trials. To obtain more general conclusions, we conducted the experiments with five different eccentric distances of the paddle shaft, and the trials were repeated to receive average results. Fig. 4.10 shows the average forward locomotion speeds of the wheel-paddle module under different angular velocities of the wheel joint. Results of five eccentric distances are presented for comparison. It can be found that the locomotion speeds generally go up with larger angular velocity. Longer protruding length of the paddle also comes with faster motion. However, it is noticed that the locomotion speeds tend to go down at high actuating angular velocity ($\omega = 4.5$) in cases of $r_S = 40$ and $r_S = 30$. Since $r_S = 40$ represents the wheel-only support situation and $r_S = 30$ also corresponds to very short paddle protruding length, we believe slippage happened between the wheel and the sand at high rotational speeds, which could be found in the logged video as well.

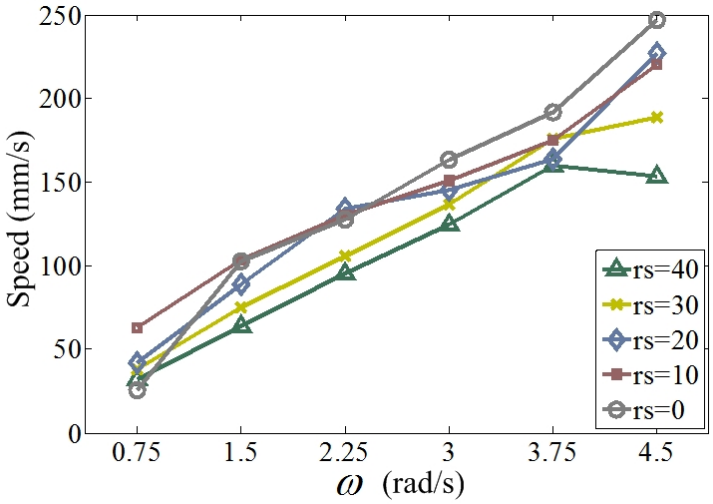

Figure 4.10. Traversing speed during the free-walking tests.

B. Efficiency

The slippage also resulted in inefficiency, as seen in Fig. 4.11. Here, we still use the Specific Resistance (SR) to evaluate the efficiency of the locomotion. To be specific, small SR values mean high locomotion efficiency. The results show that the locomotion in wheel-only support configuration ($r_S = 40$) is the most inefficiency, and the value of SR reaches the highest at $4.5 rad/s$. It can be concluded that the slippage happening between the wheel and the soil reduces both the forward speed and the efficiency, while the paddles protruding out of the wheel can effectively improve the performance. Concerning the most efficient configuration, it is found that it depends on the actuated angular velocity ω. When the angular velocity is small ($\omega < 2.25 rad/s$), $r_S = 10$ is the most efficient. While $r_S = 0$ is comparatively more efficient at high actuating velocity ($\omega > 2.25 rad/s$). This phenomenon could be caused by large resistance existing at low speed when $r_S = 0$, which consumes more energy to move the unit.

C. Vertical Vibration

Fig. 4.12 shows the amplitude of the height variant in vertical direction of the wheel-paddle module during the locomotion, which are obtained based on the data recorded

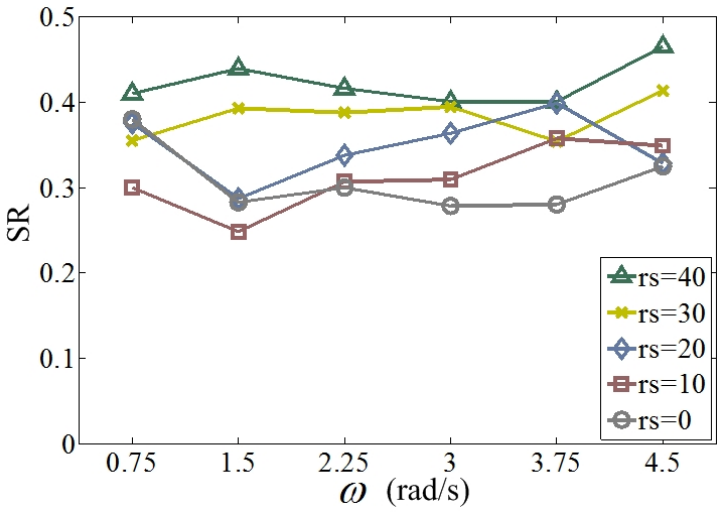

Figure 4.11. Experimental results of free walking tests: (a) forward locomotion speed of the paddle wheel; (b) specific resistance; (c) height variant.

by the motion capture as well. When the module performs with the wheel-only support configuration, the height variant is nearly zero. But the values get much larger after the eccentric distance turns to be smaller than $30mm$. This means while the configuration with small eccentric distance can perform high speed and efficiency, vibrations may be caused to the system at the same time.

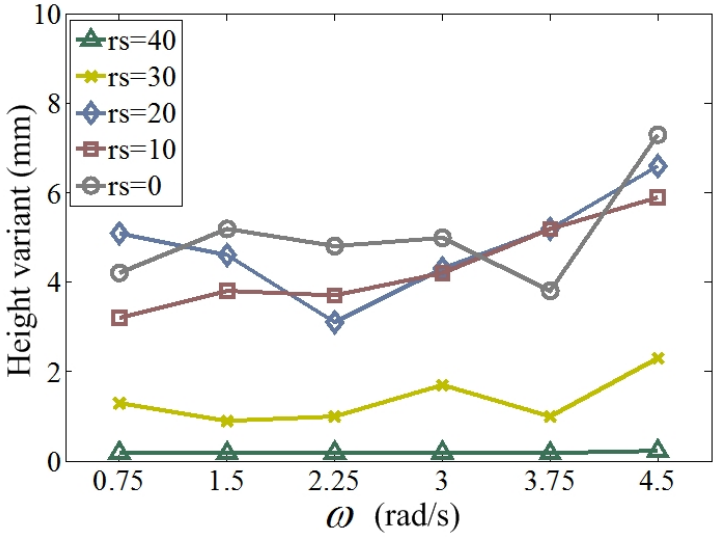

Figure 4.12. Experimental results of free walking tests: (a) forward locomotion speed of the paddle wheel; (b) specific resistance; (c) height variant.

4.4 Robot Traversing Sand Field

4.4.1 Field Environment

The locomotion performance of one wheel-paddle module has been evaluated with indoor testbed. To verify the trafficability of the whole robot in real world soft terrain, experiments were also conducted in the sand field as shown in Fig. 4.13. The experiment site is located at Ritsumeikan University (BKC, Shiga, Japan) and is named as Robot Experimental Field. To be noticed, the properties of the sand substrate in this field (name Sand II) are different from the one that was used in indoor tests (name Sand I). The particle diameter and the density are larger than the sand in testbed. Besides, the sand field is not guaranteed to be even or homogeneous, which increased the randomness of the results. Though by multiple experiments we find the results reflecting general conclusions that will be illustrated by following.

4.4.2 Results Analysis

Experiments were conducted with various configurations (or support stances) of the robot as well as different actuating velocities of the wheel joint. First the energy consumption was evaluated under different configurations, which include the paddle-support ($r_S = 0mm$), the hybrid-support ($r_S = 30mm$) and the wheel-support ($r_S = 40mm$). The motor currents during one rotational period of 2 seconds while traversing in sand are shown in Fig. 4.14(a). It is found that the currents are the largest in paddle-support configuration while least in the wheel-support. However, the specific resistance (SR) was also calculated and the results are shown in the figure. We can see that the hybrid-support tends to be the most efficient, and the wheel-support is the most inefficient. This could be caused by the slippage happened between the wheel and the sand during wheel-only support situation. The slippage reduced the current consumption but decreased the traversing speed at the same time, resulting inefficiency. This result also proved the conclusion in one-module

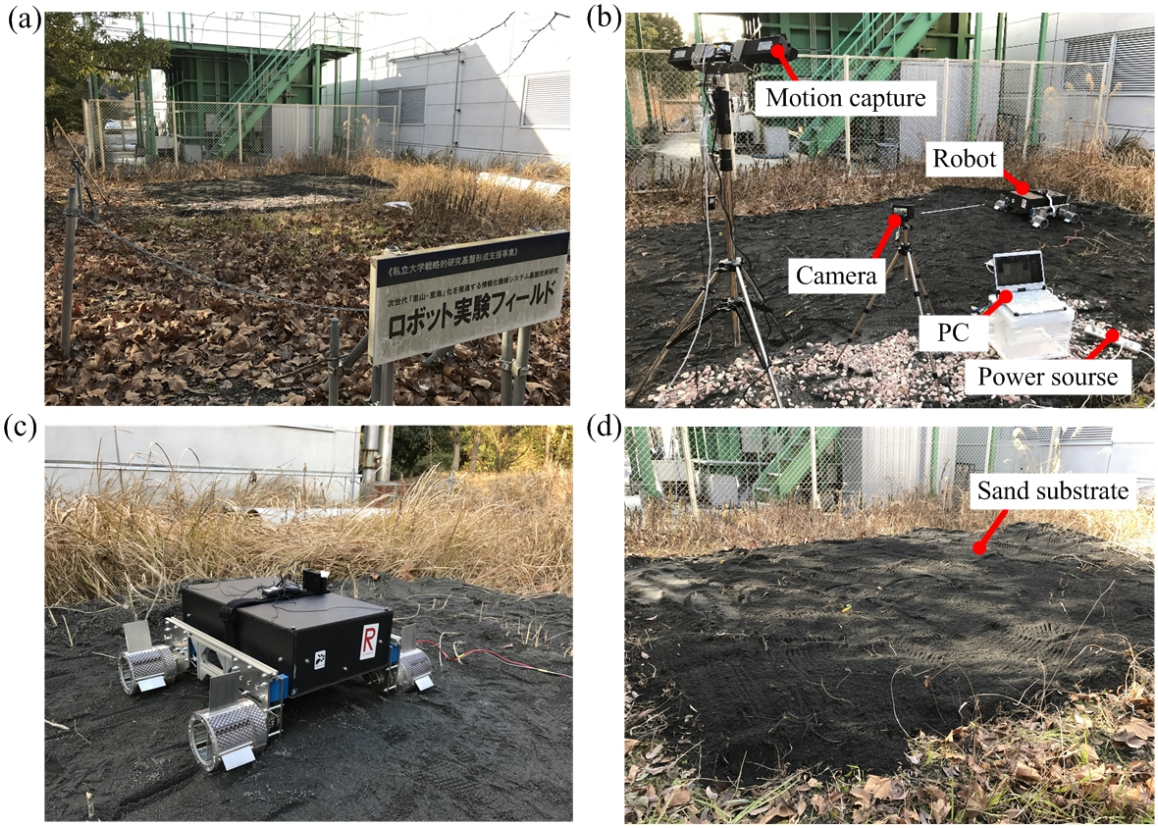

Figure 4.13. Experimental environment of real sand field: (1) robot experiment field in Ritsumeikan University; (b) overall layout of instruments; (c) tested robot with four wheel-paddle modules; (d) sand field.

free walking test that the protruding paddle helps reduce the slippage and can improve the performance.

Besides, to give a comparison between the locomotion in sand field and on flat floor under different configurations, the results from floor tests are shown in Fig. 4.14(b) as well. The same phenomenon can be found in the current results that along with the paddle protruding out of the wheel, the current increased. The difference is that the value of the specific resistance also increased with the current increasing, which means the wheel-support is the most efficient in floor locomotion. The reason of the difference between sand locomotion and floor locomotion is whether the slippage occurs. In both cases, the paddle-support configuration consumes more energy. But the slippage affects the locomotion speed so as to the specific resistance.

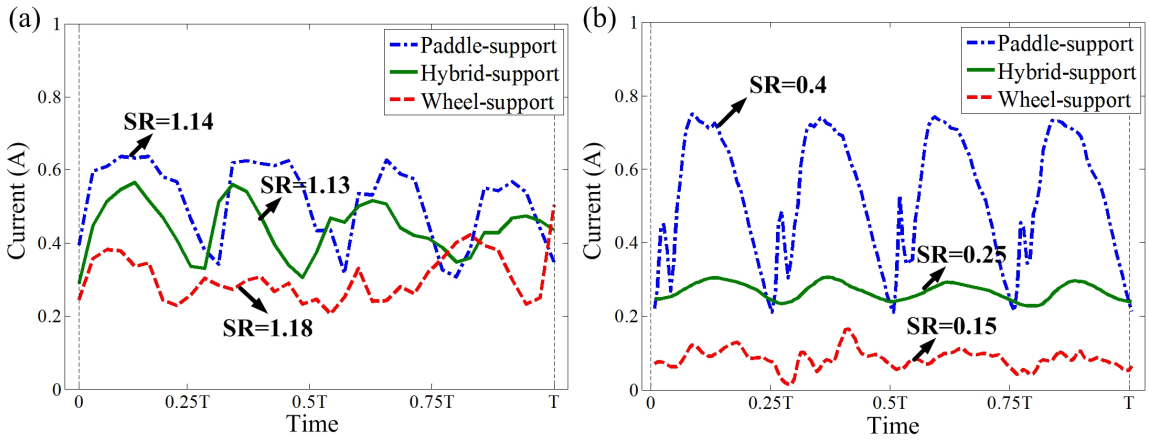

Figure 4.14. Comparison of the energy consumption with different support situations: (a) results in sand field; (2) results of floor motion.

Since the hybrid-support configuration was found to be the most efficient in sand locomotion, we evaluated the traversing speed as well as the specific resistance in different actuating velocities of the wheel joint. The results are shown in Fig. 4.15. It is found that the traversing speed increased slowly at low actuating velocity (before $3rad/s$). And after then the traversing speed almost increased linearly along with the actuating velocity. When the actuating velocity passes $8rad/s$ the traversing speed of the robot is approaching one body length per second. Through the specific resistance curve in blue line, we can see it is

not efficient at low speeds. While along with the traversing speed increasing, the efficiency is getting higher. The inefficiency at low speeds could be caused by large resistance from the sand substrate.

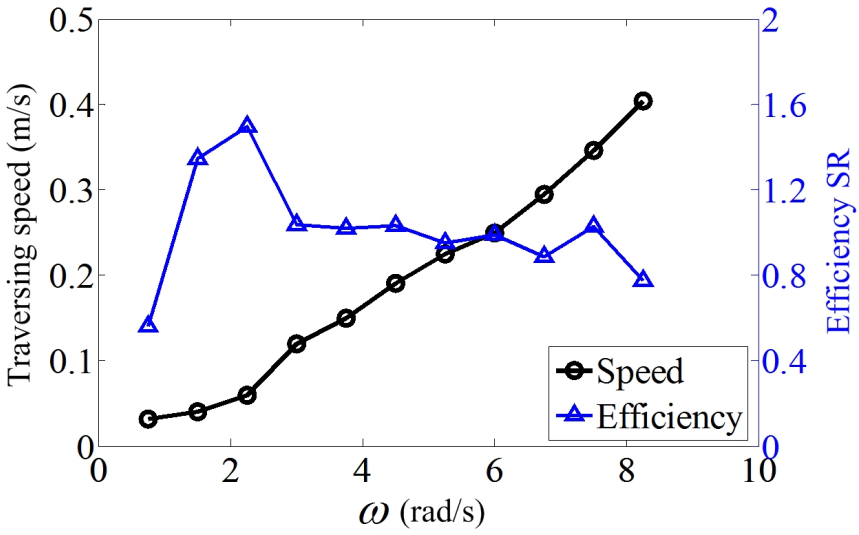

Figure 4.15. Traversing speed and specific resistance of the robot while conducting hybrid mode in sand field with various actuating velocities.

So far, all the locomotion performances of the robot on various terrains have been evaluated in hybrid mode. The dependence of the efficiency specific resistance on the traversing speed is summarized in Fig. 4.16. All the specific resistances in rough terrains are depicted in asterisks, the flat floor data are in black line and the sand field data are in blue line. We can see that the efficiency of the locomotion in rough terrain is between the sand and flat floor. The sand locomotion is the most inefficient due to its large resistance generated by the substrate, which has set up a claim to the motion planning in granular media.

4.5 Discussion

Comparing the results from one-module free walking and whole robot tests in sand field, we found the optimal eccentric distance of the paddle shaft (or the maximum protruding length of the paddle) is different. In one-module free walking, it is found that the paddle-

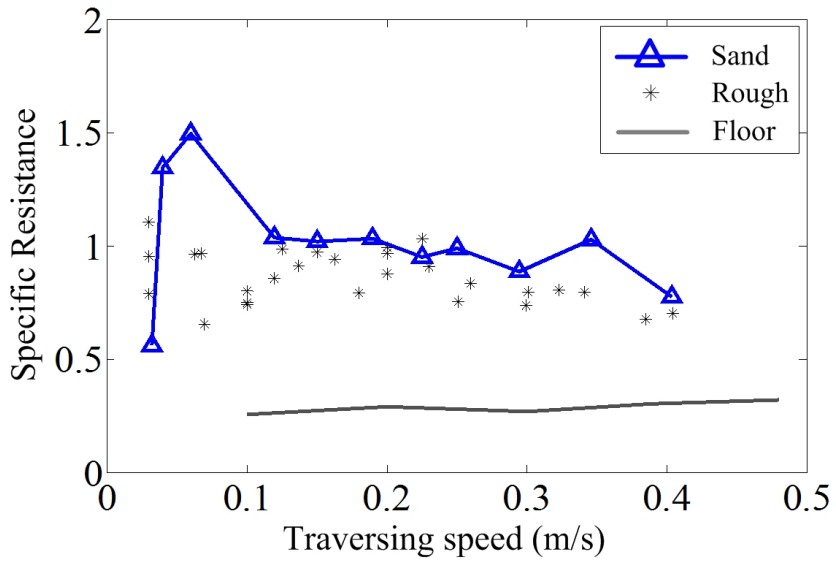

Figure 4.16. Comparison of the robot locomotion efficiency in different terrain situations.

support configuration ($r_S = 0mm, r_S = 10mm$) achieves the most efficient locomotion in laboratory sand (Sand I). While in outdoor field tests with Sand II, the results have shown better efficiency in hybrid-support configuration. The reason inducing the difference fundamentally comes from two aspects. One is the different inertia of the system. As described in Section. **??**, in the testbed the mass that can move vertically along the vertical guides is $4.3kg$ and $6.7kg$ along the horizontal guides. But the mass of the robot in field tests is $24kg$. Another aspect is the properties of the sand used in both tests. Compared with the Sand I used in laboratory test, Sand II in outdoor tests has larger particle size and density, which means it is more difficult to insert the paddle into Sand II than Sand I. Both the above aspects affect the sinkage of the system in the substrate, and so as to the propulsion force and resistance force. Hence, we conclude the optimal configuration is dependent on the system inertia and the sand properties. For a mature robot prototype, the inertia is constant but the terrain encountering is variable according to the environment. To achieve optimal configuration in various granular media terrain, it is necessary to know beforehand the properties of the substrate.

However, it is not accessible to derive all the properties of various granular media. And even it is possible, a detecting system that can distinguish the substrate type in real-time

need to be developed. Through the experiments, we found it possible to detect the sinkage of the wheel if setting up a camera that can shoot the contact situation between the wheel and the sand substrate. Fig. 4.17 shows some pictures taken in the one-module free walking tests. For example, the indentations in Fig. 4.17(a) indicate where the paddles pull out of the sand. The length between two indentations thus equals one step length. We can find the step length in $r_S = 30mm$ is smaller than $r_S = 0$, which coincide with the theoretical analysis. As for the exact length of each step, it depends on the sinkage of the wheel as well, which also gives us another way to detect the sinkage. Fig. 4.17(b) shows different pile shapes after the module traversing in different speeds. And the pile shape is also affected by the eccentric distance r_S as shown in the left figure of Fig. 4.17(c). As we concluded, it is easy to slip in wheel-support configuration ($r_S = 40mm$) especially at high locomotion speeds. As seen in Fig. 4.17(c), the step length also decreases along with the slippage happening. So the slippage can be detected through the step length variance as well. Fig. 4.17(d) compares the sinkage of the wheel in different configurations. It proved that the protruding paddle can not only reduce the slippage but also the sinkage. All these photos have inspired us to realize detecting the locomotion performance of the robot in soft terrain through image processing method.

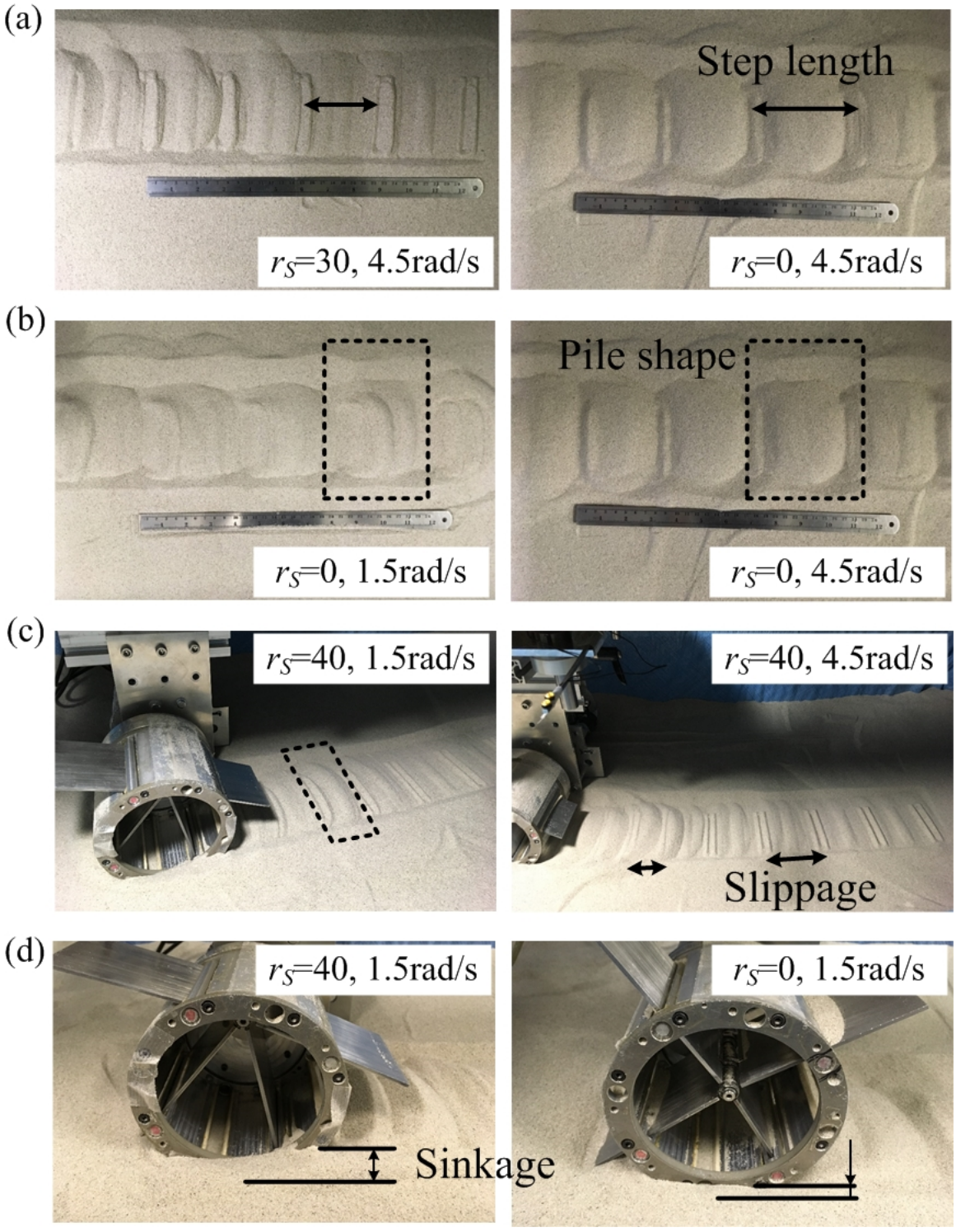

Figure 4.17. Images shoot from the one-module free walking tests.

Chapter 5

Propulsion in Aquatic Environment

So far the locomotion performance of the developed wheel-paddle integrated robot on terrestrial terrains has been investigated. Thanks to the large area of the paddles, this robot can be applied to effective propulsion in aquatic environment as well. This chapter introduces several swimming modes that are suitable for different application scenarios. We built a hydrodynamic model to predict the generated thrust underwater and the propulsion performance of different swimming modes were evaluated and compared. Based on the simulation and experiment results, an optimized solution will be suggested.

5.1 Previous Work

5.1.1 Existing Swimming Modes

Due to the reconfigurability of the eccentric paddle mechanism, various swimming modes can be achieved as well. It is also necessary to vary the swimming mode according to the water environment and the task requirement. Two different swimming modes have been proposed in our previous work, as shown in Fig. 5.1. The oscillating paddling mode is

similar to the swimming mode of AQUA [51, 52], both mimic the motion of fish tail, as shown in Fig. 5.1(a). Since there are four paddles in one wheel-paddle module, one of them is recognized as the working paddle to protrude the longest out of the wheel (as depicted in blue line). While conducting the oscillating paddling mode, only the angular position of the wheel is actuated, but the paddle shaft is fixed at the eccentric distances r_S and the angular position θ_S. To generate a smooth periodical oscillating motion, the angular position of the wheel follows a sinusoidal trajectory. The sinusoidal trajectory is defined by the oscillating amplitude A_P, the oscillating period T, and the average position of oscillation A_0. For the rotational paddling mode, the paddle shaft is also fixed during the motion at a certain eccentricity as shown in Fig. 5.1(b). Different from the oscillating mode, the wheel joint is actuated to rotate continuously in the same direction at a certain velocity ω.

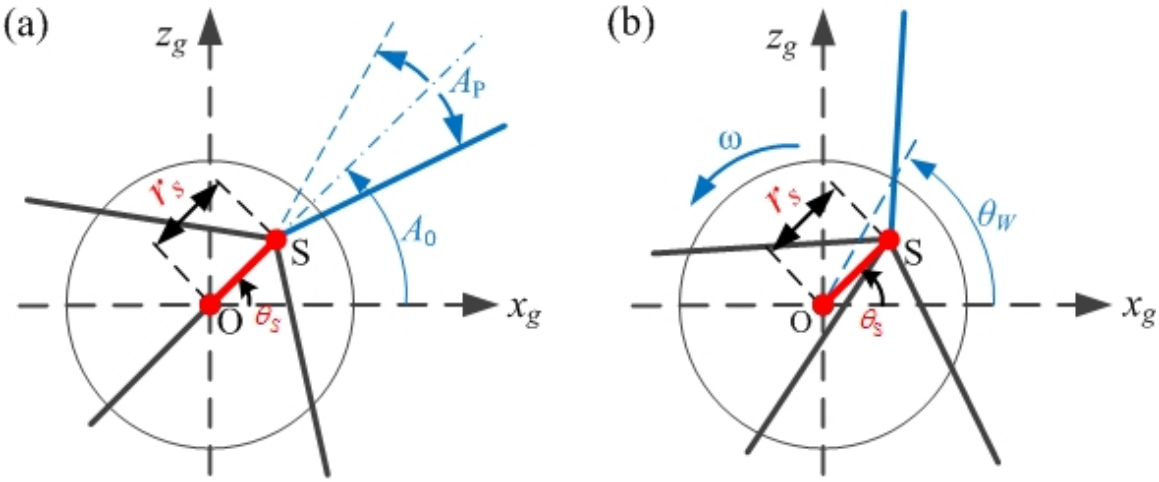

Figure 5.1. Existing swimming modes realized by the eccentric paddle mechanism: (a) oscillating mode; (b) rotational mode.

Each of these two modes has its own specialty and weakness, so they are suitable for different occasions. Generally, the rotational paddling mode can achieve faster cruising speed, but it may be limited by the space to deal with. Besides, the rotational paddling mode induces huge undulations to the fluent, which may destroy the aquatic environment. But on the other side, the oscillating paddling mode can reach comparatively stable flow field and is able to maneuver in shallow water.

5.1.2 Motivation

In our previous work, it has been verified that both oscillating paddling mode and rotational paddling mode can produce effective underwater propelling forces. And a rough thrust model and simulation were introduced as well [39, 53]. To study the effect of the paddle compliance on the generating thrusts, both rigid and flexible paddles were utilized in the oscillating paddling trials [39, 40]. For the rigid paddle situation, the thrust will increase with smaller oscillating period, larger oscillating amplitude, and bigger asymmetry ratio. And for the rotational paddling mode, the propelling thrust increases with the decreasing of motion period.

Yet, the module was set horizontal during all the tests, which violated the design concept of the robot and may cause mistakes to the results. Therefore, the module will be set vertical to do the experiments in this chapter. Besides, the vector of the force has never been referred to in the past measurements. While generating vectored thrust is substantial in controlling the motion of the robot underwater. Hence, we will explore the vectored thrust generated by the eccentric paddle mechanism. And since the comparison between the oscillating paddling mode and the rotational paddling mode is still not covered, it will be discussed as well in this chapter.

5.2 Hydrodynamic Modeling

The previous thrust model was based on Georgiades's [52] research where the generated force consists of lift force and drag force. But after resetting the attitude of the wheel-paddle module from horizontal to vertical, extra mass of water could be produced on the surface of the paddles. Generally, there are two fundamental theories about modeling the hydrodynamic force that acts on swimming bodies. One is the Taylor's [54] resistive force model which is effective for slow motion at low Reynolds numbers. The viscous force is dominant in this situation. Another one is the Lighthill's [55] reactive force model which is suitable for large swimmers that dominated by added mass effects. Comparing with

the reactive forces, the resistive forces can be neglected in this case. Consequently, both models are only valid when the geometry of the swimmer and the flow regime meet the corresponding assumptions.

Considering the geometry of our wheel-paddle robot and the motion kinematics, it is concluded to be containing both the two cases mentioned above. To be specifically, both the drag force effect and the added mass effect are working during the motion and they should be considered in our thrust model [56]. As a result, we modeled the hydrodynamic force based on the Morisons equations, which takes into account the drag forces, the added mass effects, the fluid moment and the current effects [57, 58]. The paddle is recognized as a slender body, and the forces generated by the wheel as well as the part of the paddle inside the wheel are ignored for simplification. What is more, the fluid is regarded as viscid and incompressible.

5.2.1 Notations and Defined Symbols

The schematic diagram of hydrodynamic force applying on the wheel-paddle system is shown in Fig. 5.2. For simplification, only the eccentricity from the wheel center (O) to the paddle shaft (S), and one paddle are depicted. The wheel and other details are not shown in the figure. An inertial coordinate frame F_I ($x^g O z^g$) was created based on the origin O and the body frame F_B ($x^{p,i} S z^{p,i}$) of the i-th paddle (i=1, 2, 3, 4) is at the origin S. As shown in the figure, the x-axis of body frame $x^{p,i}$ is along the paddle length. The y-axis of both frames go into the page. Then the rotational matrix from the global frame to the paddle frame is expressed as

$$R^g_{p,i} = \begin{bmatrix} \cos\theta_{pi} & -\sin\theta_{pi} \\ \sin\theta_{pi} & \cos\theta_{pi} \end{bmatrix} \tag{5.1}$$

where θ_{pi} denotes the angular position of the i-th paddle. As declared in Section. 2.2.2, the inputs of the model or the actuated joints include the eccentric distance r_S, the eccentric angle θ_S and the angular position of the wheel θ_W. The angular position θ_{pi} can thus be obtained based on the kinematics as described in Equation. 2.2. Parameter $df_i^{p,i}$ denotes

the fluid force applied on an element of the paddle length in the body frame. In our model, the current velocity is assumed to be constant and irrotational. And for simplification, the vertical component of the current velocity was set to be zero during the modeling. Hence, the current velocity can be expressed in the inertial frame as

$$V_c^g = \begin{bmatrix} V_x \\ 0 \end{bmatrix} \tag{5.2}$$

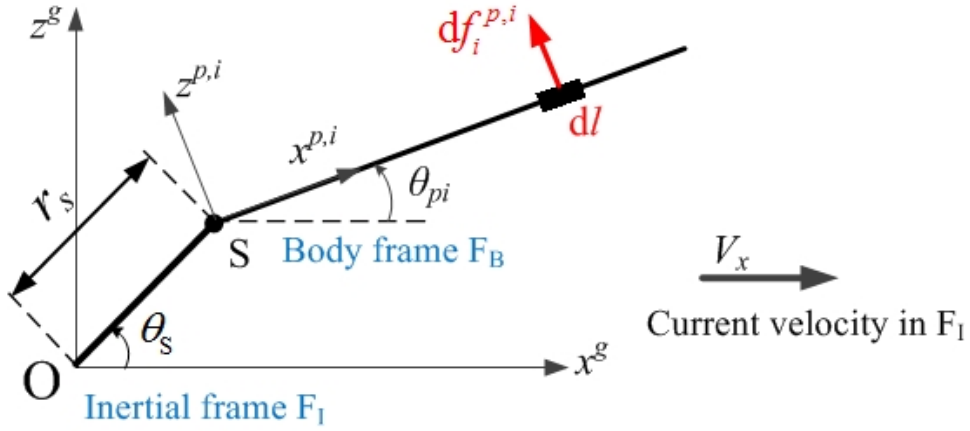

Figure 5.2. Schematic diagram of the hydrodynamic thrust applied on a paddle segment.

5.2.2 Modeling Thrust on Paddle Element

The complete modeling process could be found in Fig. 5.3. Firstly, the kinematics was applied to obtain the angular position of i-th paddle θ_{pi} (i=1,2,3,4), as well as the angular velocity $\dot{\theta}_{pi}$ and the angular acceleration $\ddot{\theta}_{pi}$. Then the current velocity was measured through experiments. Detailedly, we put a floater on the water surface and recorded the displacement during a certain time when conducting each trial. And to make it accurate, each trial was repeated seven times and the average result was obtained. After getting the current velocity in the inertial frame, the corresponding velocity ($V_c^{p,i}$) and acceleration ($\dot{V}_c^{p,i}$) of the current at each paddle frame were also calculated, following

$$V_c^{p,i} = (R_{p,i}^g)^T V_c^g \tag{5.3}$$

$$\dot{V}_c^{p,i} = \frac{d}{dt}((R_{p,i}^g)^T V_c^g) = \begin{bmatrix} -\sin\theta_{pi}\cdot\dot{\theta}_{pi} & \cos\theta_{pi}\cdot\dot{\theta}_{pi} \\ -\cos\theta_{pi}\cdot\dot{\theta}_{pi} & -\sin\theta_{pi}\cdot\dot{\theta}_{pi} \end{bmatrix} \begin{bmatrix} V_x \\ 0 \end{bmatrix} \tag{5.4}$$

As shown in Fig. 5.2, if the location of the paddle element dl from the paddle shaft is denoted as L. Then the normal velocity of the element resulting from the paddle rotation is

$$V_i^{p,i} = \begin{bmatrix} 0 \\ \dot{\theta}_{pi} L \end{bmatrix} \tag{5.5}$$

And the relative velocity $V_{r,i}^{p,i}$ and acceleration $\dot{V}_{r,i}^{p,i}$ of the paddle element dl in the body frame which are relative to the current, could be expressed as

$$V_{r,i}^{p,i} = V_i^{p,i} - V_c^{p,i} \tag{5.6}$$

$$\dot{V}_{r,i}^{p,i} = \dot{V}_i^{p,i} - \dot{V}_c^{p,i} \tag{5.7}$$

As a result, the hydrodynamic force exerted on the paddle element dl of i-th paddle in the body frame can be calculated through

$$df_i^{p,i} = -\begin{bmatrix} \mu_t & 0 \\ 0 & \mu_n \end{bmatrix} \dot{V}_{r,i}^{p,i} - \begin{bmatrix} c_t & 0 \\ 0 & c_n \end{bmatrix} V_{r,i}^{p,i} - \begin{bmatrix} c_t & 0 \\ 0 & c_n \end{bmatrix} \mathrm{sgn}(V_{r,i}^{p,i})(V_{r,i}^{p,i})^2 \tag{5.8}$$

which is a modified formula based on the Morison's equation [59]. Each term on the right side of the equation indicates the effects from added mass forces, the effects from the linear drag forces, and the effects from the nonlinear drag forces successively. The constants in the formula are obtained through

$$\begin{bmatrix} c_t & 0 \\ 0 & c_n \end{bmatrix} = \begin{bmatrix} \frac{1}{8}\rho\pi C_f l(a+b) & 0 \\ 0 & \frac{1}{2}\rho C_D l a \end{bmatrix} \tag{5.9}$$

$$\begin{bmatrix} \mu_t & 0 \\ 0 & \mu_n \end{bmatrix} = \begin{bmatrix} 0 & 0 \\ 0 & \rho\pi C_A l(\frac{a}{2})^2 \end{bmatrix} \tag{5.10}$$

which are dependent on the geometry of the paddles and the fluid characteristics. The notation l, a and b denote the length of the paddle, the width of the paddle and the thickness of the paddle respectively, as described in Table. 2.1. ρ is the density of the

water, while C_f and C_D are the drag coefficients in x and z directions, and C_A is the added mass coefficient. According to the experience values in [60, 61] and the Reynolds number differences, the coefficients in our case were set as $C_f = 0.3$, $C_D = 20$, $C_A = 10$, which were verified through experiments. Besides, μ_t indicates the added mass parameter in the x-axis, and it was set to zero because the added mass effect in the longitudinal direction of the paddle could be neglected compared with the body mass.

5.2.3 Modeling Thrust on Wheel-paddle Module

Based on the force applied on the paddle element, the total thrust on the ith paddle in the inertial frame can be calculated by integration on the protruding length of the paddle outside the wheel, following

$$f_i^g = R_{p,i}^g f_i^{p,i} = R_{p,i}^g \int_{l-l_{pi}}^{l} df_i^{p,i} \tag{5.11}$$

where $f_i^{p,i}$ is the thrust of paddle i in the body frame, and l_{pi} is the paddle length inside the wheel [40]. Then the whole fluid thrust produced by one wheel-paddle module can be obtained

$$F = \sum_{i=1}^{4} f_i^g \tag{5.12}$$

which can also be expressed as the sum of added mass forces and drag forces [62].

5.3 Thrust Measuring Experiment

In order to experimentally measure the fluid forces generated by the wheel-paddle module and verify the proposed hydrodynamic model, we built a force measuring setup. Both the oscillating paddling mode and the rotational paddling mode were tested with various inputs to explore the propulsion performance and compare with each other.

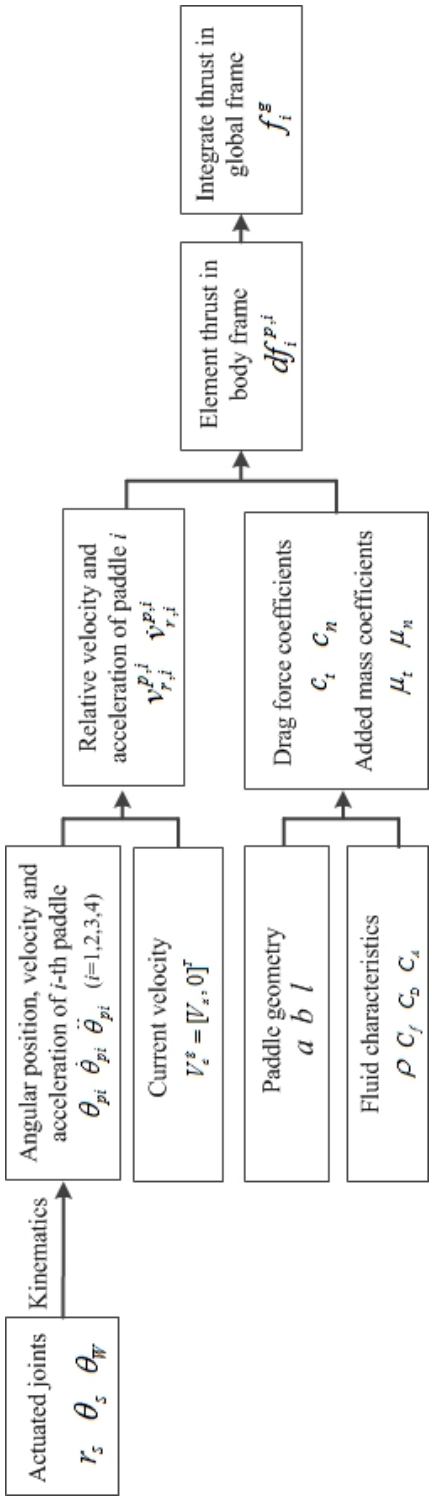

Figure 5.3. Process for modeling the thrust generated by the wheel-paddle module.

5.3.1 Experimental Setup

The experimental setup is shown in Fig. 5.4. Since this is a force test on one wheel-paddle module and to protect the electronic parts from water, a simple new prototype was constructed for the experiment, as seen in Fig. 5.4(a). A 6-axis force sensor (F/T Delta SI-330-30, ATI Industrial Automation, USA) was connected with the tested wheel-paddle module. Timing belts were applied to transit torques from the motors to the wheel-paddle module. During the experiment, the motors and the force sensor were maintained above the water surface, while the wheel-paddle module was submerged beneath the water surface. The tested module follows the original design principle. But most parts were fabricated with 3-D printer, so the total mass is much smaller than the real robot prototype. To be mentioned here, this fabrication method may be limited to aquatic locomotion currently due to the less stress properties. Fig. 5.4(b) shows the experimental field, where a water tank with the size of $2.3m \times 1.8m \times 1.7m$ is used. Comparing with the size of the tested module, the water tank is so much larger that the boundary effect could be ignored.

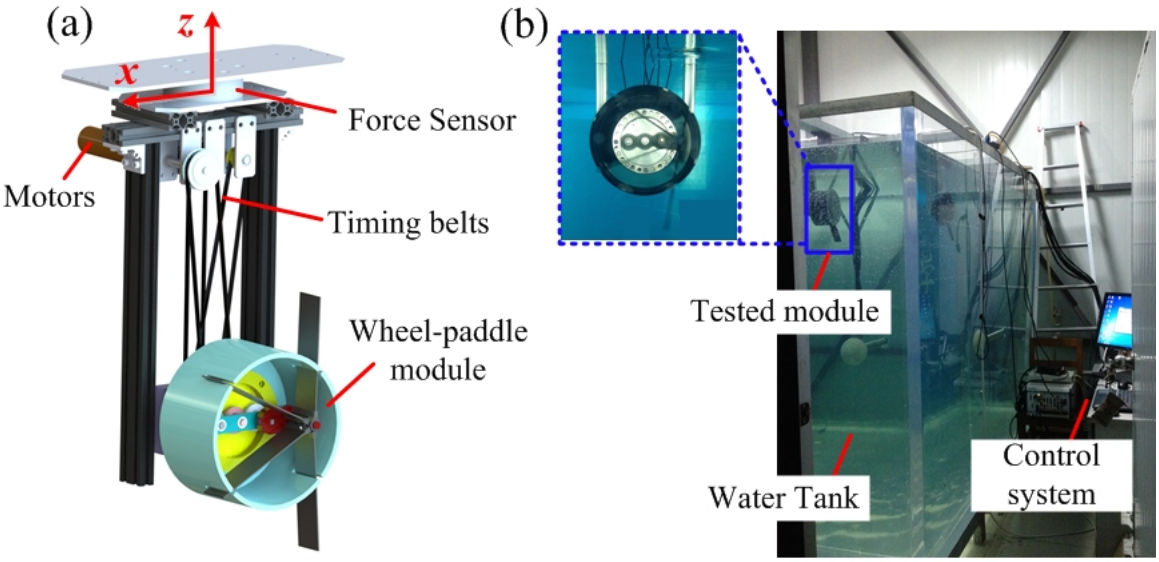

Figure 5.4. Experimental setup for measuring thrust.

5.3.2 Design of Experiment

Since the purpose of the study is to explore the thrust characteristics such as the force amplitude, the vector, and the propulsion efficiency, and then to compare the two paddling modes from these aspects. Therefore, we designed the tested trials and listed the values of each controlled parameter during the experiment as seen in Table. 5.1. Generally, the paddle shaft's location was adjusted to change the propulsion direction and the wheel joint was controlled to vary the amplitude of thrust. To be specifically, the eccentric distance (r_S) was always fixed at $60mm$, to protrude the longest length out of the wheel. The angular position of the paddle shaft was set around the wheel circle at an interval of $30deg$ separately in each trial to explore the vectored property. And to obtain different force amplitudes, both the locomotion period (T) and amplitude (A_p, oscillating mode) were altered.

To reduce the random errors in the test, each combination trial was conducted for seven times or seven groups. And for the data from each group, we took five out of fifteen periods for analysis. The average results were then obtained based on the five periods from seven groups. Besides, we waited until the waves receded between two trials so as to avoid the influence from the previous test. The force data recorded by the sensor is called instantaneous forces $F_{x,z}(t)$, which is inevitable to include various noise signals such as the vibration of the frame, the whitle noise and the waves produced during the motion. To deal with these noise signals, We used an automatic wavelet denoise toolbox [63]. Except for the instantaneous forces, we also calculated the cumulative force F_{cum} and the time-averaged force F_{ave} to analyze the net thrust, following

$$F_{cum} = \int_0^{nT} F_{x,z}(t)dt \tag{5.13}$$

$$F_{ave} = \frac{1}{nT} F_{cum} \tag{5.14}$$

5.3.3 Results Analysis

The experimental results will be analyzed from three aspects. First, how the force magnitudes change with the motion period and the oscillating amplitude will be presented

Table 5.1. PARAMETER SETTINGS DURING THE EXPERIMENTS

Controlled Joint	Description	Symbols (Units)	Swimming Modes	
			Oscillating Paddling Mode	Rotational Paddling Mode
Paddle shaft	Eccentric distance	$r_S(mm)$	60	60
	Angular position	θ_S (deg)	-180 $\sim$ 180 (interval 30)	-180 $\sim$ 180 (interval 30)
Wheel	Motion period	T (s)	0.8, 1, 1.2	2.5, 3.5, 4.5, 5.5
	Oscillation amplitude	A (deg)	30, 45, 60	N/A

in Part A. Then, the dependence of thrust vectors on the angular position of the paddle shaft is analyzed in Part B. Finally, the propulsion efficiency will be compared between two swimming modes.

A. Thrust Magnitude

To study the thrust magnitude, we first fixed the paddle shaft at the angular position of $0deg$ in all the tests. For the oscillating paddling mode, the instantaneous forces generated with $A_p = 45$ and $T = 0.8$ are shown in Fig. 5.5(a). It is found that the proposed hydrodynamic model successfully predicted the forces in both directions. And the frequency of the forces in x-axis is twice the frequency in z-axis. To examine clearly the effective thrusts, the time-averaged forces with various oscillating periods and amplitudes are depicted in Fig. 5.5(b). If we just look at the forces in the forward direction or x-axis, it is seen that the effective thrust increases with larger oscillating amplitude and shorter motion period.

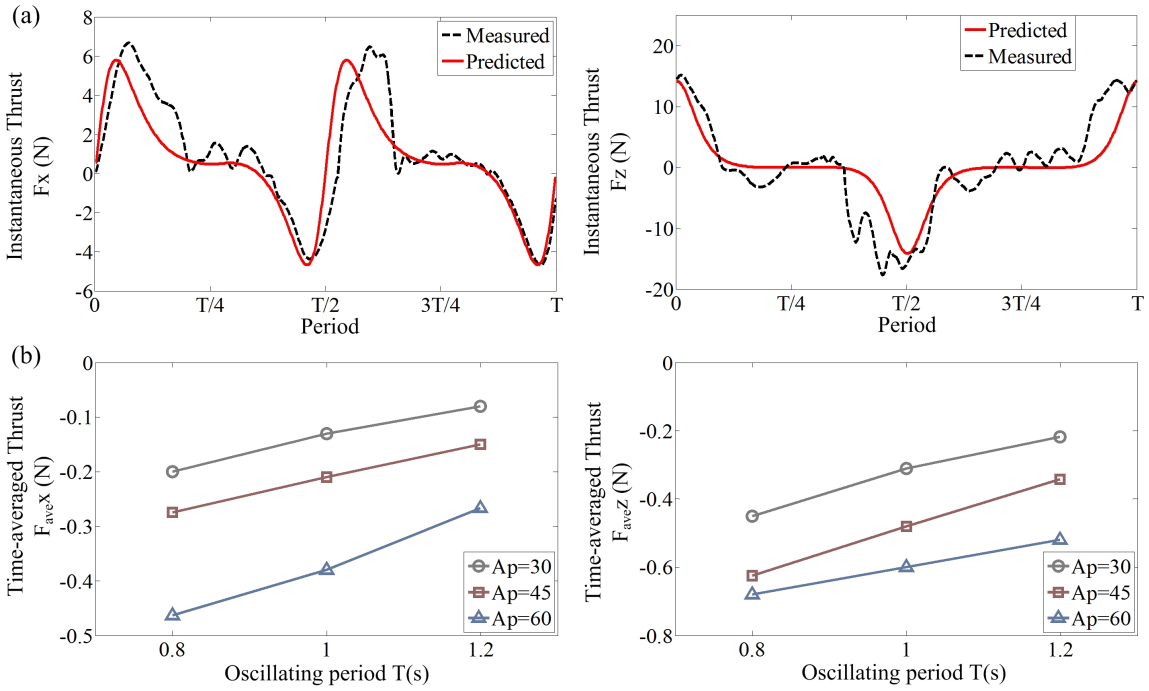

Figure 5.5. (a) Instantaneous thrusts and (b) time-averaged thrusts generated by the oscillating paddling mode when angular position of the paddle shaft is at 0.

As for the rotational paddling mode, the instantaneous forces are also depicted in Fig.

5.6(a), where the rotational period is 2.5s. The model results accorded with the measured ones as well. Different with the profile of the forces generated by the oscillating model, four peaks and four troughs exist in both directions in rotational mode. To analyze the effective thrust, cumulative forces were calculated and shown in Fig. 5.6(b). It is found that the effective force increases with smaller rotational period. And comparing with the oscillating mode, the amplitude of effective thrust of rotational mode is much larger.

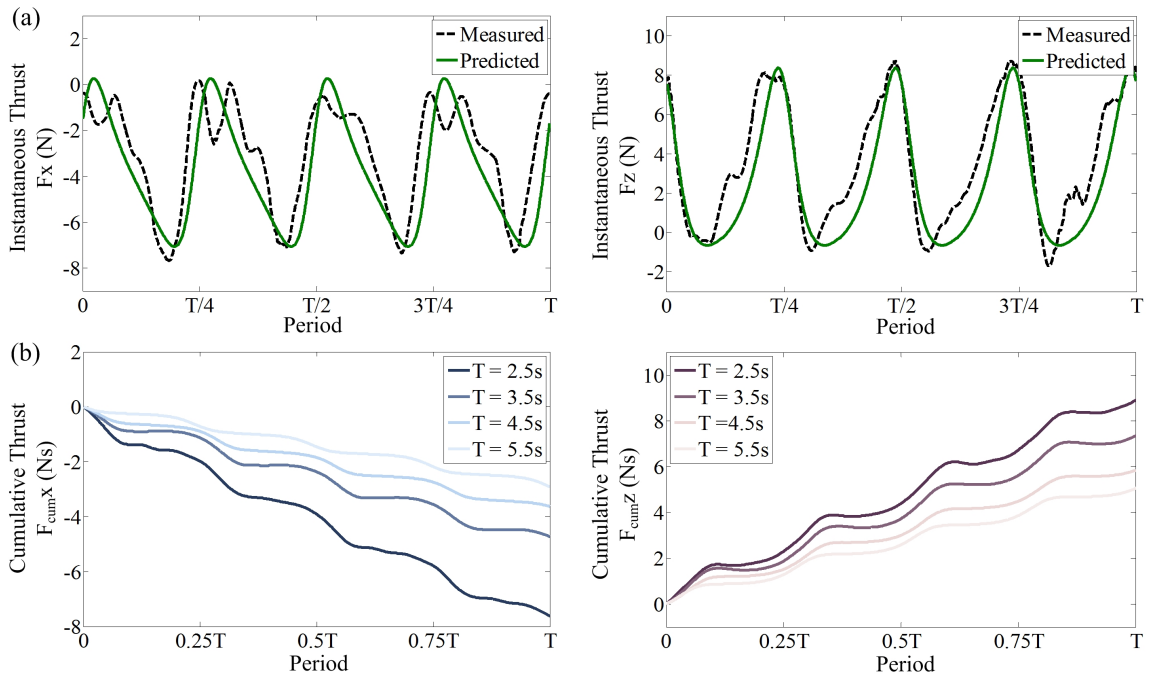

Figure 5.6. (a) Instantaneous thrusts and (b) cumulative thrusts generated by the rotational paddling mode when angular position of the paddle shaft is at 0.

B. Thrust Direction

As declared before, the thrust direction may be varied by adjusting the location of the paddle shaft or the eccentric angular of the paddle shaft. In this section, we keep the motion period and the oscillating amplitude constant while locate the paddle shaft all around the wheel circle to measure the generated forces. As shown in Fig. 5.7(a), the force direction of the oscillating paddling mode actually changed with the eccentric angular of the paddle shaft. What is more, the relation almost follows a linear function according to the fitted curve. Except for the force direction, the force magnitudes were also calculated while

adjusting the location of the paddle shaft, as shown in Fig. 5.7(b). It is found that even the oscillating period is constant, the force magnitude still changes along with the angular position of the paddle shaft. The results of the rotational paddling mode are also presented, as seen in Fig. 5.8. Same phenomenon can be discovered from the results. Besides, we can see that the largest forces in both modes occurred near the angular position of $-90deg$, which means the paddle shaft is located at the lowest point inside the wheel.

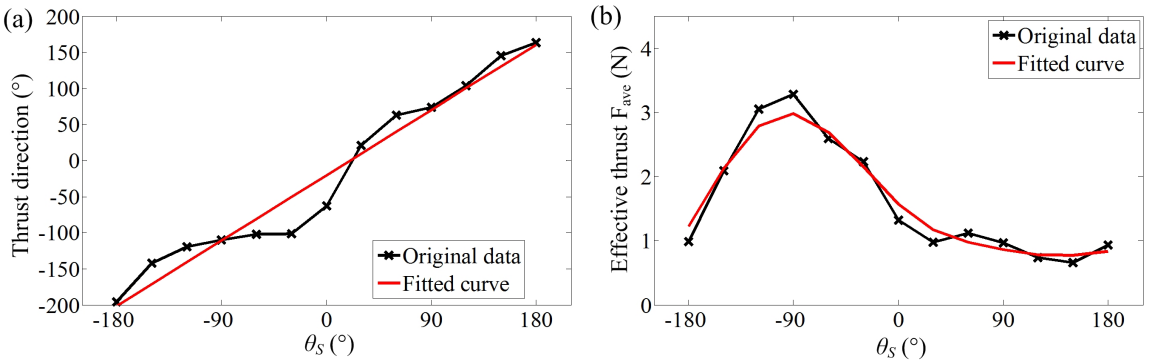

Figure 5.7. (a) Thrust direction of the oscillating paddling mode ($A_p = 45$, $T = 0.8s$) with different angular position of paddle shaft; (b) Effective thrust magnitudes with different angular position of paddle shaft.

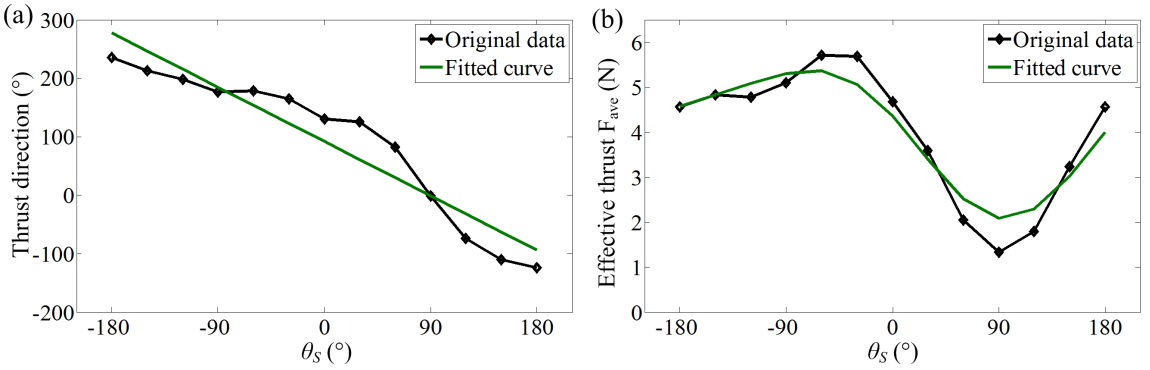

Figure 5.8. (a) Thrust direction of the rotational paddling mode ($A_p = 45$, $T = 0.8s$) with different angular position of paddle shaft; (b) Effective thrust magnitudes with different angular position of paddle shaft.

To make it more clear to understand the vectored characteristics of the thrust and compare between the two swimming modes, a vectored thrust figure containing both modes was depicted as shown in Fig. 5.9. The coordinate of each marked point in the figure indicates the generated effective thrust in x-axis and z-axis directions separately. It is easy

to find that both modes can generate vectored thrust around a circle and the rotational paddling mode produces larger forces.

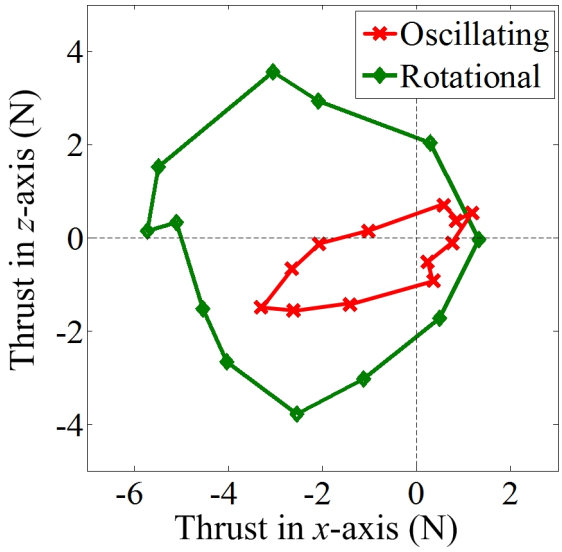

Figure 5.9. Generated vectored thrust by both oscillating paddling mode and rotational paddling mode.

C. Propulsion Efficiency

It is already known that the rotational paddling mode can generate larger thrusts than the oscillating mode, and both of them can produce linear vectored thrust. This section will discuss on the propulsion efficiency from energy consumption. Here the efficiency was calculated by dividing the thrust magnitude with the work consumption by all the motors in one motion period. The work consumption by the motors can be obtained through the feedback from the controllers. As a result, the calculated propulsion efficiency is shown in Fig. 5.10. It is found that although the oscillating paddling mode did not generate larger thrusts, it is more efficient at some locations of the paddle shaft. The path that the paddles travel through in rotational mode is much longer than in the oscillating mode, which costs more energy while generating larger effective thrust. Hence, we conclude that the rotational paddling may be good at generating large thrust and fast motion in broad water area, but the oscillating paddling mode is more suitable for efficient cruising in narrow space.

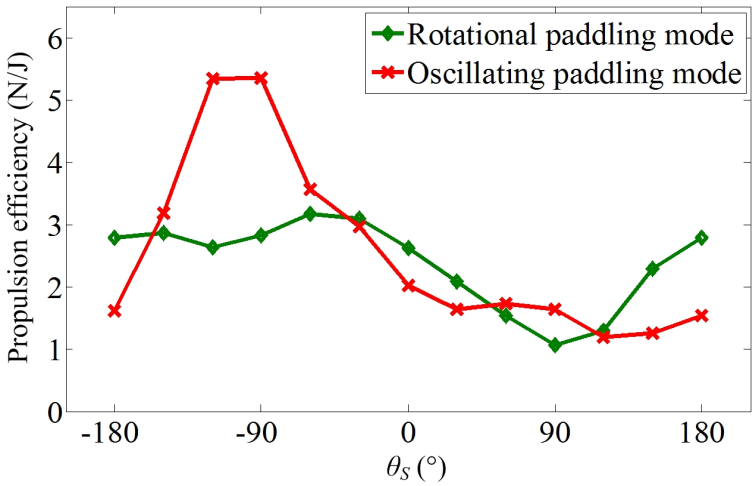

Figure 5.10. Comparison between the energy consumption of both swimming modes.

5.4 Optimization on Negative Thrust

Through the previous sections, we have learned the thrust characteristics of the oscillating paddling mode and the rotational paddling mode. However, it is found that quite a lot negative forces exist in the instantaneous force data of the oscillating paddling mode, as shown in Fig. 5.5(a). And the amplitude of the negative force almost equals the amplitude of the positive force, which resulted in small effective forces as shown in Fig. 5.5(b). Actually this is a common problem that happens to most fish inspired swimming robots. For the real fish, both the compliance of the body and the kinematics they realized help reduce the negative force and increase the swimming efficiency. But it is still a big challenge to achieve complete biomimetic due to the limit of material and biology. Hence, we will introduce a new motion sequence which helps reduce the negative thrust effectively.

In order to reduce the negative force generated by the oscillating paddling mode, we first investigated the reason causing this phenomenon. By following the direction of the thrusts and the motion of the mainly working paddle, we found that the negative forces always occur when the relative velocity direction of the paddle is same with the forward direction, and the thrust will be positive when the directions are opposed. The former is called recovery phase and the latter is called stroke phase. For most fish-like swimming motion, both these

two phases have to exist at the same time. Hence, we believe the net thrust can be increased by extending the working time and improving the propulsion effectiveness in stroke phase, at the same time reducing the resistance force in recovery phase. Then we noticed the front crawl stroke, which is a competitive swimming stroke realized by human and is known as the fastest and most efficient among all the four competitive strokes [64, 65]. Human conduct the recovery phase in the air and insert the upper limb into the water at a small incident angle to reduce the resistance force. Even though our wheel-paddle robot is more than a surface swimmer, we get inspiration from the human swimming and have designed a front crawl stroke based on our mechanism. To be noted that the motion of human legs in front crawl stroke will not be involved in this research because legs only contribute 10% to the propulsion [66].

5.4.1 Novel Swimming Mode: Front Crawl Stroke

The front crawl stroke realized in the eccentric paddle mechanism consists of a stroke phase and a recovery phase in one stroke period as well. Fig. 5.11(a) shows the stroke phase conducted by human [67], and Fig. 5.11(b) depicts the stroke motion realized by the eccentric paddle mechanism where the wheel works like the human shoulder and the paddles are seen as the upper limbs. In configuration A, the paddle shaft is located at the left-most location ($r_S = 60$, $\theta_S = 180°$) so that the working paddle (paddle 1) protrudes the longest outside of the wheel. While performing the stroke phase, the paddle shaft and the wheel rotate around the wheel center at the same angular speed, and end with the paddle shaft arriving at the right-most location ($r_S = 60$, $\theta_S = 0°$). As a result, the working paddle goes through an angular displacement of π which is much larger than the oscillating amplitude of less than $\pi/2$. The effective propulsion area of the working paddle is marked with blue shadow in Fig. 5.11(c). For simplification, the effect of paddle 2 and paddle 3 will not be considered since the protruding lengths of both are very small. In order to actuate the wheel and the paddle shaft to rotate synchronously around the wheel center, the velocities

of the input joints need to follow

$$\omega_0 = \omega_1 = \omega_2 \tag{5.15}$$

where $\omega_0, \omega_1, \omega_2$ are the angular velocity of the wheel joint, the sun gear and the annulus gear respectively. This equation is based on the kinematics of the eccentric paddle mechanism, which derivation can be found in our previous work [46].

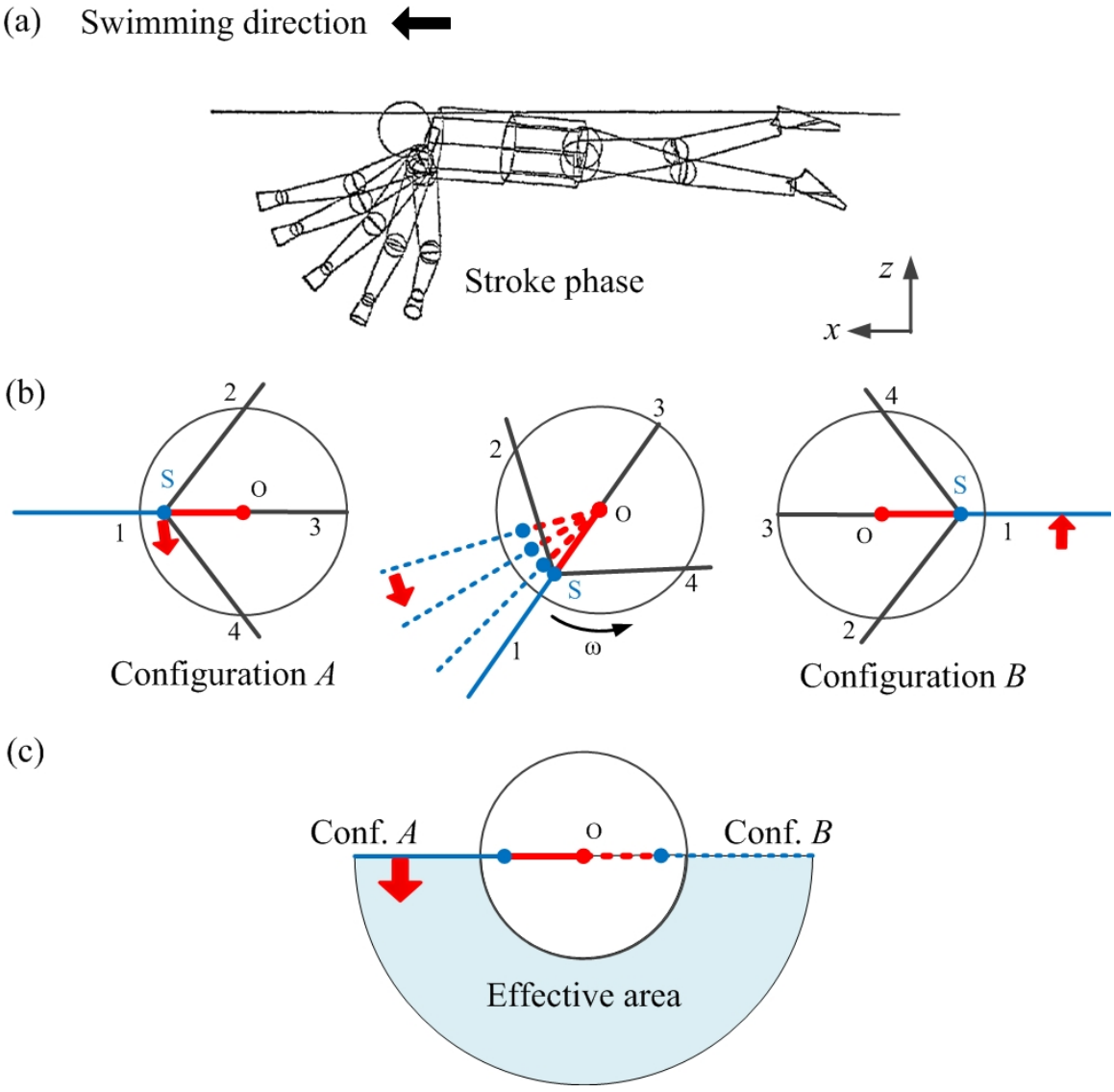

Figure 5.11. (a) Human performing the stroke phase during the front crawl stroke [67]; (b) stroke phase realized by the eccentric paddle mechanism; (c) Effective propulsion area in stroke phase by the working paddle.

As for the recovery phase, Fig. 5.12(a) shows the human action on the water surface. But to reduce the resistance force underwater, the working paddle is planned to retract

horizontally into the wheel and then stick out of the wheel horizontally as well. In this case, the upstream face which is the cross section of the paddle will be very small area. The resistance force thus can be minimized. As shown in Fig. 5.12(b), after the stroke phase, the wheel-paddle mechanism will transfer from configuration B back to configuration $A^{'}$ to finish one stroke cycle. The only difference between the configuration A and $A^{'}$ is the main working paddle, which changes from paddle 1 to paddle 3. Therefore, paddle 1 and 3 take turns to perform as the working paddle. During all the recovery phase, the wheel joint keeps still. And to actuate the paddle shaft move straight along the diameter, the joints ω_1 and ω_2 should satisfy

$$\omega_1 = 9\omega_2 \tag{5.16}$$

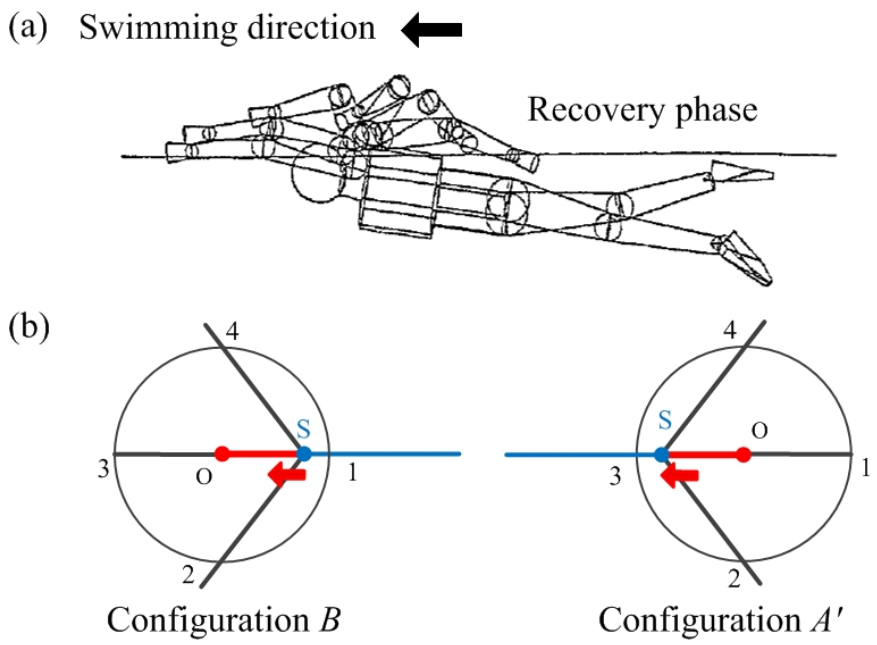

Figure 5.12. (a) Human performing the recovery phase during the front crawl stroke [67]; (b) recovery phase realized by the eccentric paddle mechanism.

To realize accurate control of the front crawl stroke, the planetary gear system that actuate the paddle shaft is crucial. We first depicted the planned trajectory of the paddle shaft as shown in Fig. 5.13 with the solid black line. The linear speed of the paddle shaft

in the stroke phase and the recovery phase can be calculated as

$$v_S = \begin{cases} 0.06\omega_0 = 0.06\omega_1 = 0.06\omega_2, & \text{stroke phase} \\ 180\omega_2 \cos(3\omega_2 t - \frac{\pi}{2}), & \text{recovery phase} \end{cases} \tag{5.17}$$

where t is the time after the paddle shaft left the right-most point. It can be found that the speed of the paddle shaft is constant during the stroke phase, while the speed profile follows a sinusoidal curve during the recovery phase. Moreover, the speed reaches the highest at the wheel center and equals zero at configurations $A(A^{'})$ and B. As a result, the step change occurs to the speed of the paddle shaft when transiting at configuration A and configuration B. And if following Equation. 5.15 and Equation. 5.16, it is easy to see that the velocity step change also happens to each actuated joint, which may result in vibration of the system as well as the inaccuracy of the motion. To solve this problem, the trajectory of the paddle shaft was optimized as shown in Fig. 5.13 with the green lines. Sinusoidal curves were used to connect the stroke phase and the recovery phase.

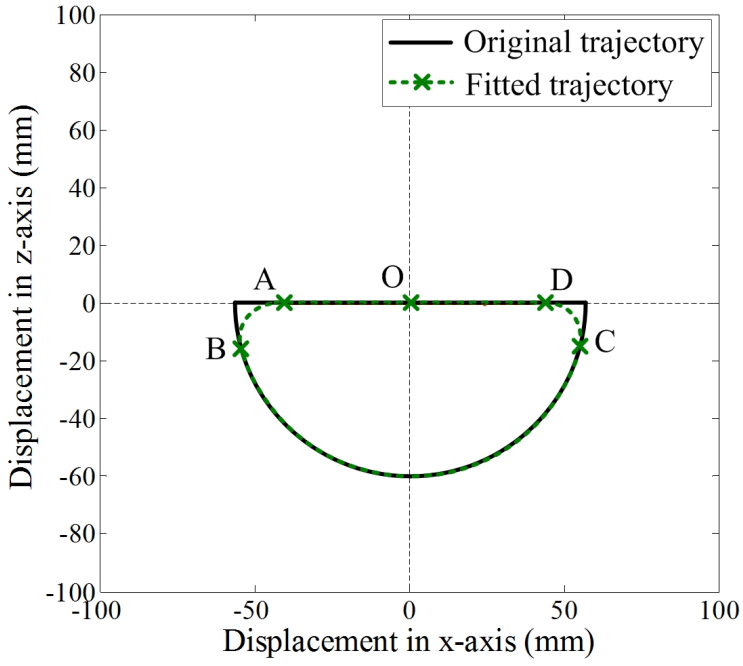

Figure 5.13. Designed trajectory of the paddle shaft.

To define the front crawl stroke mathematically, T is denoted as the period of one whole stroke motion. Duty factor a is defined as the ratio of the time in stroke phase to the period

T. The fitting time between the stroke phase and the recovery phase (curve AB and CD in Fig. 5.13) is described by $t^{'}$. To be specifically, the velocity curves of the actuated joints when $T = 2.2s$, $a = 0.5$, $t^{'} = 0.3s$ were depicted as an example in Fig. 5.14. The key points in Fig. 5.13 are also marked in Fig. 5.14 for reference. And two periods are shown in the velocity curves. It is obvious that all joints are following continuous velocity curves. And the velocity directions keep constant as well, which helps reduce the inaccuracy caused by the gear clearance. To ensure the fitting performance concerning both the paddle shaft and the paddle, the fitting time $t^{'}$ was optimized as constant $0.3s$.

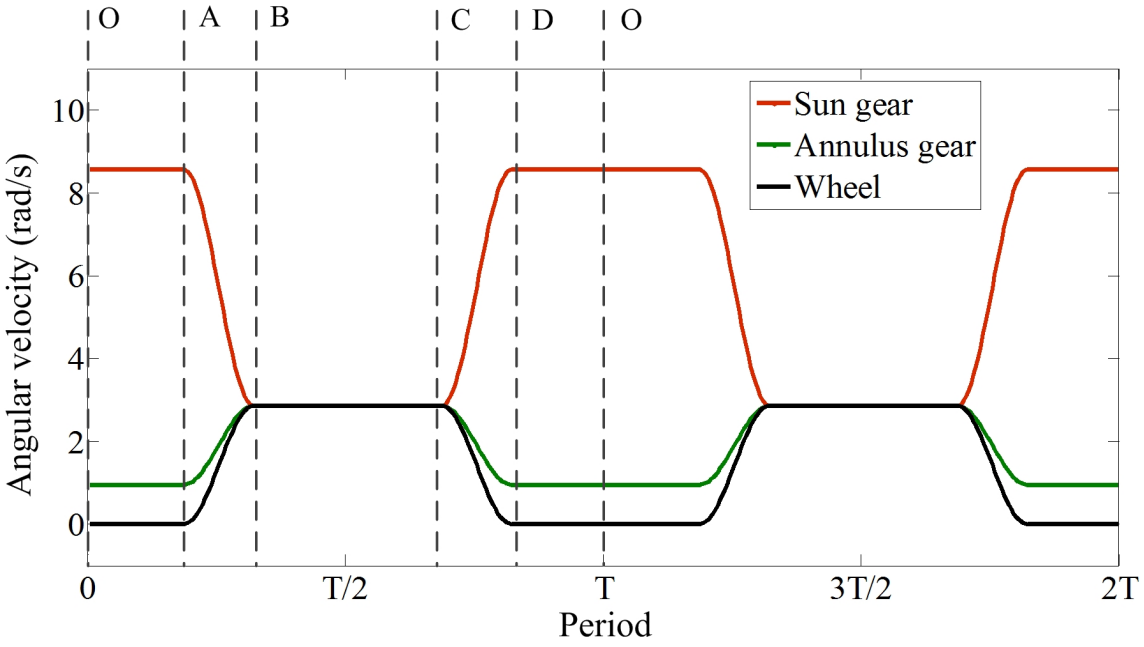

Figure 5.14. Actuated angular velocity of each joint during the front crawl stroke.

5.4.2 Simulation Study

Based on the hydrodynamic model in Sec. 5.2, we first looked into the predicted forces by the front crawl stroke. The simulation results with various combinations of the period T and the duty factor a are shown in Fig. 5.15, where the x-axis is the along the forward direction and the y-axis is on the vertical direction. From the instantaneous force results in Fig. 5.15(a), it is found that the negative forces in the forward direction are very small

comparing with the positive forces in all cases. And smaller duty factor tends to decrease the negative force more effectively. Based on the time the negative forces exist, it is deduced that the negative force was generated during the recovery phase by the resistance of the paddle upstream. Besides, the force profile tends to be stable but with lower peak in larger duty factors. And generally short period results in large amplitude of force.

To explore the effective net thrust, the cumulative force which was calculated by integrating the instantaneous force over time was also shown in Fig. 5.15(b). We can see that the force generated by smaller period and duty factor is comparatively larger, but not too much. And the forces in the vertical direction almost equal zero, which presents the same characteristics with the fin-like oscillating motion.

5.4.3 Experimental Verification

To verify the simulation results, the front crawl stroke was realized experimentally as well. Same with the previous aquatic experiments, each trial was repeated seven times and averaged to reduce the random errors. And to create a stable flow field, twenty periods of strokes were repeated in one trial and the last ten periods data were recorded. Fig. 5.16 shows one period results of the instantaneous force and the cumulative force with the stroke period of $1.4s$ and the duty factor of 0.3. The instantaneous forces show that the simulation results almost successfully predicted the actual force profiles. Only there are little vibrations existing during the recovery phase in the measured forces. The reasons could be from two aspects. One is that the section of the paddle inside the wheel was ignored during the theoretical analysis. But in real experiments, that part could affect the results as well. And according to the kinematics of the paddle inside the wheel, it can be induced that the vibrations occur in the recovery phase. Another reason should be the cross section of the paddle which can generated resistance force as an upstream face. It also affects more during the recovery phase. Except for the instantaneous force, the cumulative force were also calculated in Fig. 5.16(b). It is seen that the experimental net thrusts are

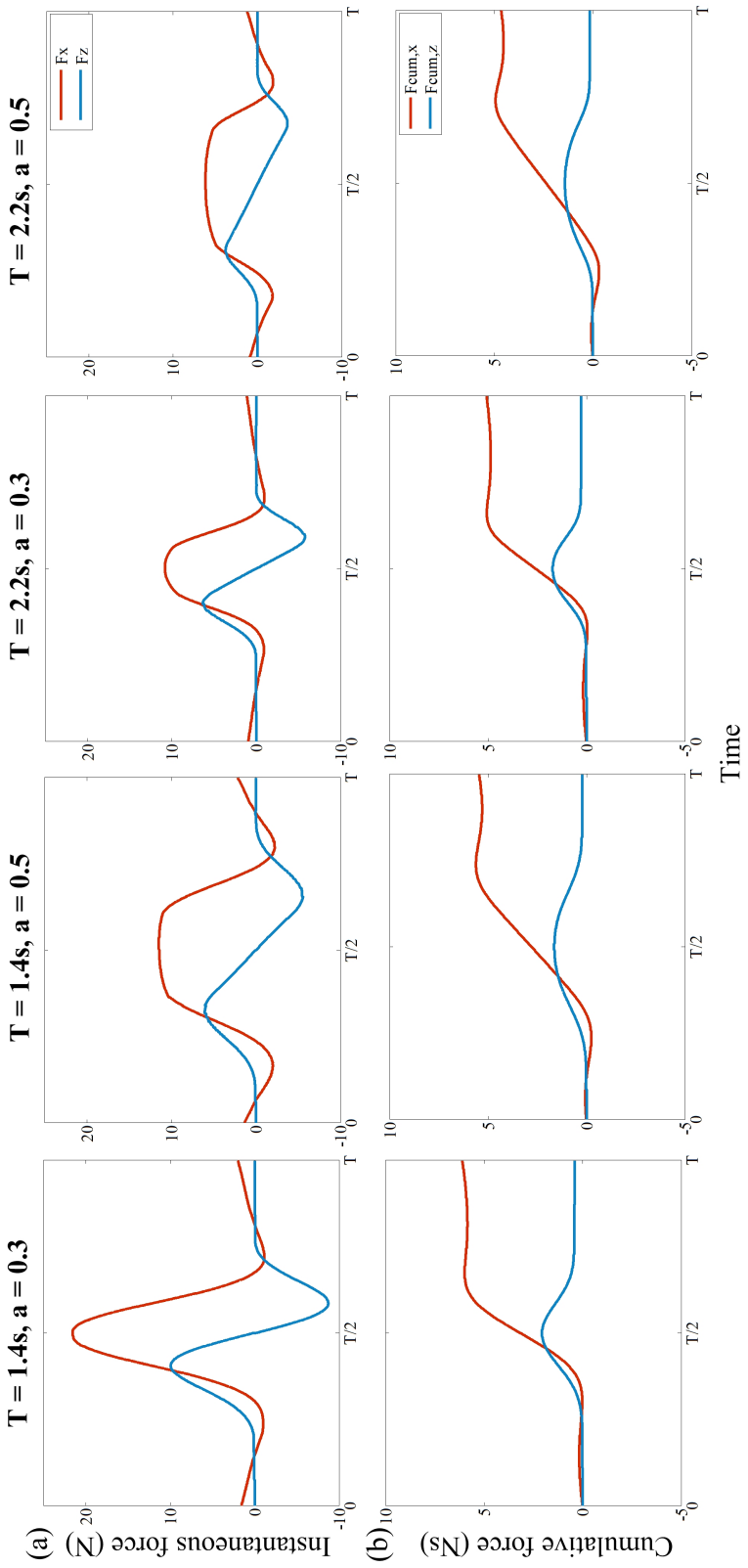

Figure 5.15. Predicted (a) instantaneous forces and (b) cumulative forces generated by the front crawl stroke with various time periods and duty factors.

a little larger than the simulation results. This is because different from the theoretical model, the flow velocity is not time constant during the experiments.

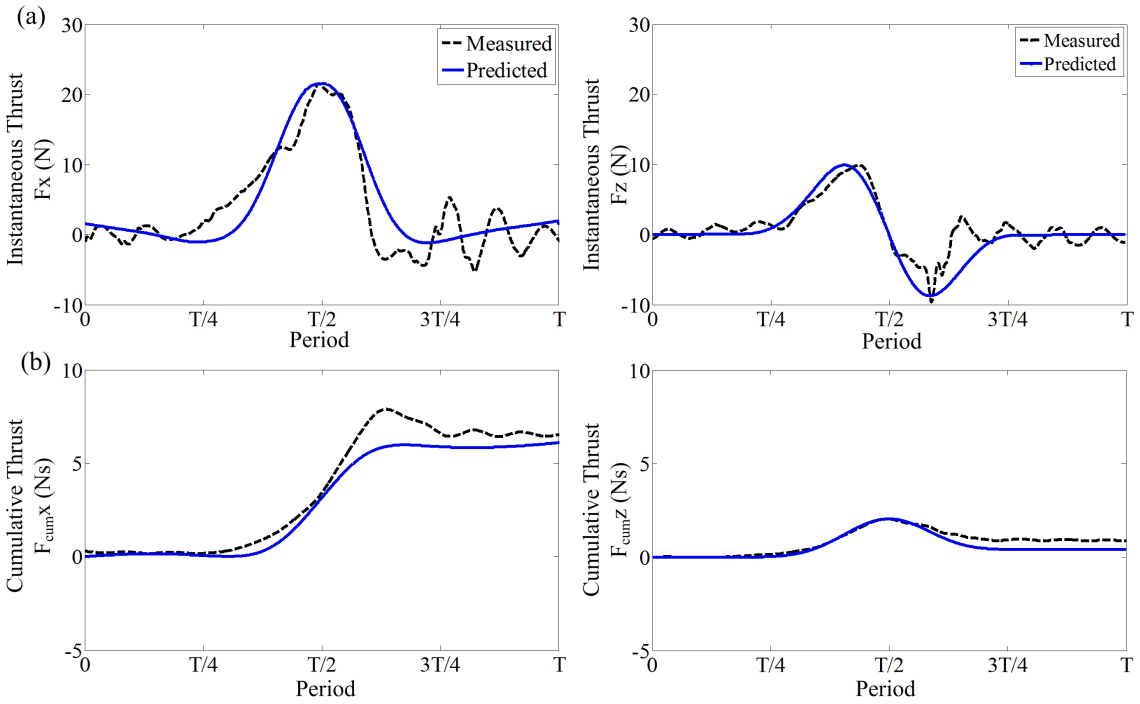

Figure 5.16. Comparison between the predicted and measured forces generated with $T = 1.4s, a = 0.3$: (a) instantaneous force in forward direction (x-axis) and vertical direction (z-axis); (b) cumulative force in forward direction and vertical direction.

As seen from the cumulative force in z-axis, the values almost equal zero in both simulation and experimental results. Hence, we focus on the thrust in the forward direction. Fig. 5.17 shows the cumulative forces in x-axis with different stroke periods and duty factors. It is found that generally short motion period leads to large net thrust. But during the period from $1.6s$ to $2.0s$, the net thrust vary little. Besides, the results of smaller duty factor do generate much larger net thrusts. The maximum cumulative thrust is more than three times large of the minimum value, by speeding up the stroke frequency. Yet, the thrust profiles of small duty factor are not as smooth and stable as the ones of large duty factor. And the negative force is more effectively reduced in larger duty factor scenarios.

To inspect the energy efficiency of the front crawl stroke, the output torques and the angular velocities of the motors were back fed and recorded to calculate the energy consumption during all the experiments. To mathematically evaluate the efficiency, we defined

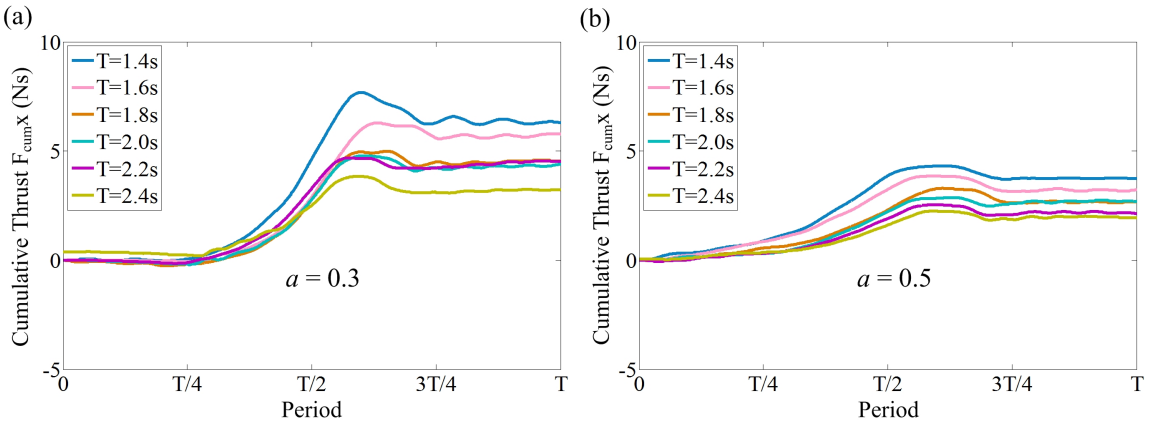

Figure 5.17. Cumulative thrust in the forward direction (x-axis) with different stroke periods and duty factors: (a) duty factor $a = 0.3$; (b) duty factor $a = 0.5$.

a stroke efficiency η as

$$\eta = \frac{\int F_x(t)dt}{\sum_{i=1}^{3} \int T_i(t)\omega_i(t)dt} \tag{5.18}$$

where $T_i(t)$ and $\omega_i(t)$ indicate the output torque and angular velocity of motor i at time t, and $F_x(t)$ is the propelling thrust in the forward direction at time t [68]. Fig. 5.18 shows the comparison of the stoke efficiency under different time periods and duty factors. It is found that the strokes with lower duty factor ($a = 0.3$) are always more efficient than the large duty factor ($a = 0.5$) in all periods. Specifically, the stroke efficiency is almost constant when the duty factor is 0.5, while the generated thrust increases with shorter period. In comparison, there exists an obvious extreme value of the efficiency when the duty factor is 0.3. The most efficient stroke happens to the period of $2.2s$ instead of $1.4s$, which suggests that generating larger propulsion thrust may also consume more energy. Hence, it is important to figure out a balance between the propulsion thrust and the energy efficiency.

5.5 Discussion

Now that we have already explored the characteristics of the front crawl stroke swimming mode, it is possible to compare it with the previous oscillating propulsion mode. Based on

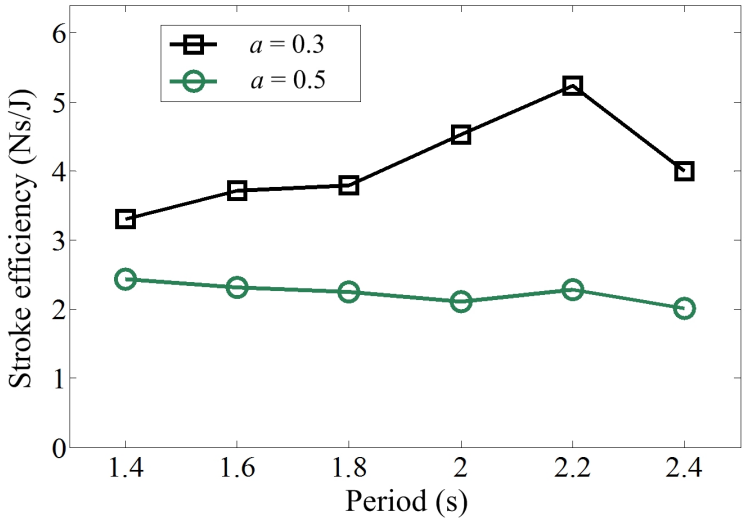

Figure 5.18. Energy efficiency of the front crawl stroke.

the intension of reducing the negative force in front crawl stroke, among all the conducted tests of these two propulsion modes, we chose two trials in which both modes achieved the same maximum positive force to analyze. As shown in Table. 5.2, the oscillating propulsion reaches the maximum instantaneous force of $12N$ when the oscillating period is $0.8s$ and the amplitude is $\pi/4$ [37]. At the same time, the front crawl stroke comes up to $11.5N$ with the stroke period of $2s$ and the duty factor of 0.3. But we can see the negative force in oscillating mode has five times amplitude of the front crawl stroke. Moreover, the negative force in oscillating mode continues longer time than that in the front crawl stroke. Hence, it leads to a big drop behind in the time-averaged cumulative force, which is calculated through dividing the cumulative force by the time it took and means the net thrust in unit time. The result of front crawl stroke is more than 3 times of the oscillating mode. As for the propulsion efficiency, front crawl stroke achieved 2.7 times η as much as the oscillating mode, even though three motors were actuated during the locomotion. Thanks to the non-reciprocating velocity trajectory of each joint, the work done by the front crawl stroke did not exceed too much than we expected.

But on the other side, the oscillating mode still does better in generating stable force and realizing precise position control due to the high frequency of motion. Another phenomenon

Table 5.2. COMPARISON BETWEEN OSCILLATING PROPULSION AND FRONT CRAWL STROKE

Swimming Mode	**Oscillating Paddling mode**	**Front Crawl Stroke**
Maximum positive thrust	12 N	11.5 N
Maximum negative thrust	-10 N	-2 N
Effective net thrust	0.68 N	2.25 N
Propulsion efficiency η	1.66 Ns/J	4.5 Ns/J

that we would like to discuss here is the undulation in the propulsion force generated by the front crawl stroke. As we know, continual constant thrust is necessary to generate a stable movement. Undulation in the force or the motion will raise the complexity of controlling and waste energy. However, we can find clearly crests of the wave in the forward direction forces F_x, especially when performing with short stroke period and lower duty factor. The propulsion force lasts long and stable while stroke slowly, but the effective thrust is small and it is not energy efficient. In addition, the cumulative forces display that the net force seldom increase during the recovery phase. To solve this problem, we will explore the gait sequence and combination in the four-module robot platform. Meanwhile, we may notice the forces generated in the vertical direction F_z, which could passively induce the variation of the robot's Euler angles while conducting free motion of the whole robot. This problem can be fixed by adjusting the configuration A shown in Fig. 5.11. Specifically, the direction of the net force can be adjusted to horizontal by altering the protruding angle of the working paddle, so as to avoid generating vertical forces. As for the exact protruding angle of the paddle, we will study theoretically and experimentally in the future. This report just focused on reducing the negative force existed in the oscillating mode to improve the net propulsion force and efficiency. And it was verified with the one-module platform that the front crawl stroke can realize it. In the future work, we will figure out the optimal gait pattern to achieve both efficient and stable swimming performance in the wheel-paddle integrated robot.

Chapter 6

Discussion

In this thesis, we first introduced the development of a wheel-paddle robot including four eccentric paddle modules. Due to the specialty of the locomotion mechanism, the four wheel-paddle modules only realized sandproof. The body that contains the electrical parts is protected from splashing water. Thus, it is possible to explore the mobility with this prototype in some severe environment such as sand, mud, snow, or even amphibious situations like shallow or water surface. As a primary testing prototype, we believe there are still much terrain research could be carried out except for those involved in this thesis. However, some problems were also found during the fabrication and the evaluation experiments of this robot prototype. For example, the balance between the friction force and the sandproof effectiveness at the hinges of each module is difficult to realize. To prevent the sand or particles from going inside the wheel, felt was applied between the paddle and the hinge, and also between the hingle and the wheel. But when the pressure among them is too large, the movement of the paddle and the rotation of the hinge will be affected, or even get stuck. In order to ensure the normal operation, we adjusted the pressure to low values. As a result, small sand particles went into the wheel and the gaps during the locomotion on granular media. These sand need to be cleaned up manually after a certain period. To realize long-term operation in outdoor environment, this problem need to be improved in the future.

Considering the application in rough terrains, we used the hybrid mode instead of previous legged locomotion. The reason is that the legged modes were originally designed for flat ground locomotion and they are based on position control, which is not suitable for rough terrain application. And the control of the legged mode is very complex, the accuracy of the transmission is difficult to maintain. To traverse and transform among various terrain situations, the robot should be able to vary its configuration accordingly to adapt to the terrain. Hence, we proposed the hybrid mode which can transform among different support stances easily only by adjusting the location of the paddle shaft. Through the experimental evaluation, we found the protruding paddles can reduce the slippage in rough terrains and the locomotion efficiency is not worse than previous legged motion but better than some other rough terrain robots. To be specific in soft terrain, the protruding paddles effectively reduced the slippage of the wheel at high speed. But the exact optimal configuration depends on several factors like the system inertia and the properties of the substrate. These factors will affect the sinkage and slippage of the robot, so as to affect the locomotion performance. Therefore, to adapt to different kinds of substrate, it is suggested to control the robot based on the detection feedback of sinkage and slippage. The detection method could include but not limited to current sensing and image processing. Since this thesis mainly presents the robot design and primary overall evaluation of the performance, to realize automatic control of the robot in rough terrains, there are still much work to be explored.

As for the aquatic locomotion, due to the previously insufficient research, we still focus on the propelling thrust generated by one wheel-paddle module in this thesis. Except for the thrust amplitude, the vectored characteristics were also studied, which is important for the motion control. Through the comparison between the oscillating mode and the rotational mode, it was found that the similarity between them is the ability of generating linear vectored thrust, and the difference lies in the oscillating propelling mode is more efficient but the rotational propelling mode can generate larger thrusts. To achieve both high efficiency and large propelling thrust, we looked into these two modes and it was found that large negative thrusts were generated during the performance, which resulted in small

net thrust. It also means that the efficiency could be increased more if the negative thrust could be reduced or even removed. According to the relation between the kinematics of the oscillating mode and the generated forces, we proposed a novel mode named as front crawl stroke, where we got inspiration from the human swimming as well. From both theoretical and experimental results, it was verified the front crawl stroke did increase the net thrust as well as the propulsion efficiency at the same time. The motion performance of all these three modes will be tested in the future on the robot. Incidentally, the front crawl stroke can also be varied to change the initial configuration and adjust the thrust direction. By controlling the thrust direction of each wheel-paddle module, the robot can realize regulation of position and orientation correspondingly. And considering imitating completely the human free-style swimming, front crawl stroke and oscillating mode can be combined to explore the performance.

Chapter 7

Conclusion and Future Work

7.1 Conclusion

In this thesis, a wheel-paddle robot based on the eccentric paddle mechanism has been developed. The objective is to evaluate the locomotion performance in various amphibious environment.

The robot is equipped with four wheel-paddle modules and complete control system. Considering the application in severe environment, necessary protection schemes are added in the prototype. And a simple but effective locomotion mode is proposed for accessing rough terrains. It is verified that the robot performing with the hybrid mode can traverse various rigid terrains like flat ground, rough grass, stones and gravels. And the efficiency is competitive among other rough terrain robots.

Moreover, the trafficability in soft terrain has been explored specially. The paddle terradynamics shows the longer protruding length the paddle has, the larger traction force can be generated. The free walking experiments also prove that the configuration with longer protruding paddles can move faster and more efficient. Especially at high speed, the protruding paddles successfully reduced the slippage happening between the wheel-paddle and the substrate. The tests are conducted in outdoor field as well. The results have shown that the robot tends to be more efficient with faster traversing speed. But combining with

the indoor experiment, it is also seen that the optimal configuration is varying along with the substrate properties as well as the system inertia.

Finally, the thrust performance of one wheel-paddle module is evaluated thoroughly. A hydrodynamic modeling method suitable for the mechanism is proposed. Both the oscillating swimming mode and the rotational swimming mode are found to generate linear vectored thrust. The oscillating mode is superior in efficiency while the rotational mode is better in generating larger amplitude of thrust. To reduce the negative force during the oscillating motion and achieve both high efficiency and large thrust, a novel front crawl stroke is proposed. The experiments have verified its effectiveness and superiority.

7.2 Future Work

In order to achieve real application of the wheel-paddle robot in severe environment, there are still much work to be further studied.

As shown in the results from locomotion on soft terrain, the protruding paddles can improve the performance. However, the optimal configuration is dependent on the system inertia and the substrate properties. These two factors will directly affect the slippage and sinkage of the robot. Therefore, it is necessary to detect the slippage and the sinkage for realizing automatic control of the robot in such terrains. The detection methods could be current sensing or setting external cameras for image processing.

Through the experiments on rough terrains it is also found that the vibration of the robot is very big when the protruding length of the paddle is large, which does no good to the system stability. To reduce the vibration and improve the stability, it is suggested that the eight-paddle configuration be used (currently four paddles in one module). Or the gait sequence among four modules should be planned in the future.

On the other hand, the properties and performance of paddles made from soft materials can be explored. In RHex-like robot, researchers have studied the effect of the leg shape on the locomotion performance [19]. It is proved that the C-shape is better than the flat

one and the reverse C-shape leg. However, the leg shape is not variable when dealing with different terrain situations. By using compliant paddles or legs, the shape is adjusted passively. The optimal compliance need to be studied furthermore. And the interaction between granular media and soft locomotor should another interesting research topic.

The compliant paddles can be utilized in underwater propulsion as well, which is similar with real fish body. To achieve the best motion performance underwater, the proposed three swimming modes can be combined. And the vector characteristics of the thrusts need to be verified again through free motion of the robot.

This thesis focus on the evaluation of forward locomotion. As for the obstacle negotiability, the maximum obstacle height and the maximum slop gradient are to be analyzed. And it is found that either the paddle-support or the wheel-support configuration is not suitable for turning. The paddles and the wheel produce large resistance forces during the rotation. If the focus of the robot is only dealing with terrestrial terrain, the author suggests replacing the paddles with cylinder legs. In order to put the robot into real application, the mechanism should be simplified and the prototype should be fabricated lighter.

Appendix A

Supplemental Motion Tests

It has been presented in the main body of the locomotion performance on various terrains. But the terrains are still flat, which do not contain any obstacles. And the focus is on the forward locomotion. For realizing field application, the wheel-paddle robot should be acquired of comprehensive mobility which include turning, climbing up slops, negotiating obstacles, et al.. Hence, some supplemental motion tests are presented in this section to verify its mobility.

A.1 Trajectory Following

In the trajectory following experiment, the robot was expected to follow an desired trajectory as shown in Fig. A.1, depicted in black solid lines. The trajectory contains a square and a half circle. The experimental setup is also shown in Fig. A.1. To obtain the position and orientation of the robot, a motion capture system (VZ4050, PTI, Canada) was utilized. During the experiment, all the paddles are retracted so only the wheels contact with the ground. So the control accuracy of the wheel joint and the robot kinematics can be verified.

The trajectory following results are shown in Fig. A.2. Both the desired trajectory and the actual trajectory of the robot are depicted in a planar coordinate system. The desired

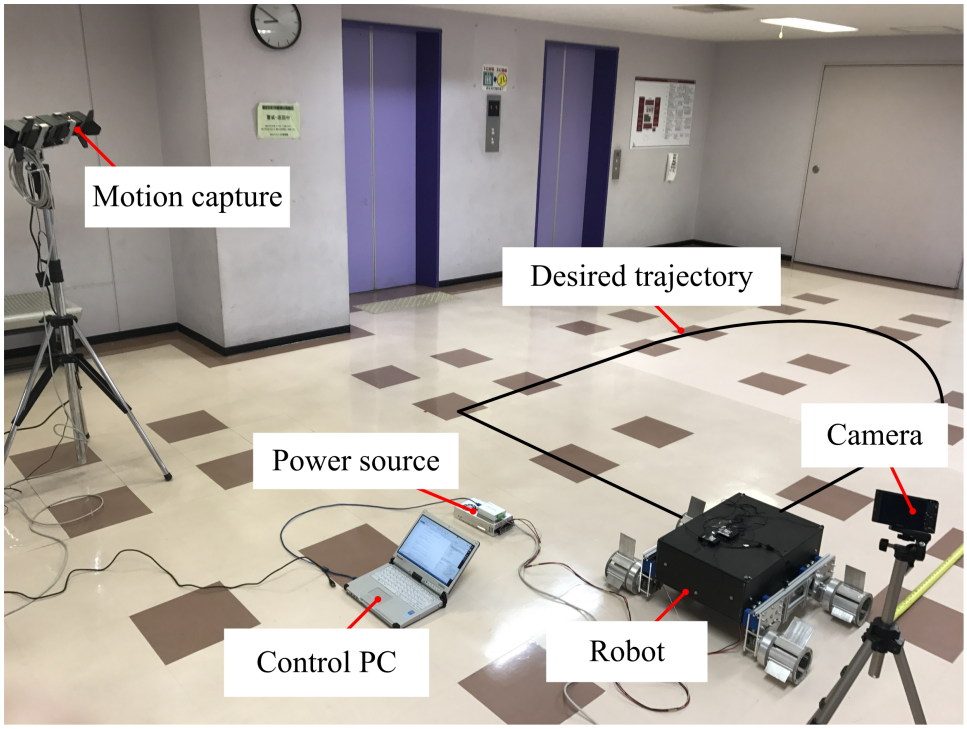

Figure A.1. Trajectory following experimental setup.

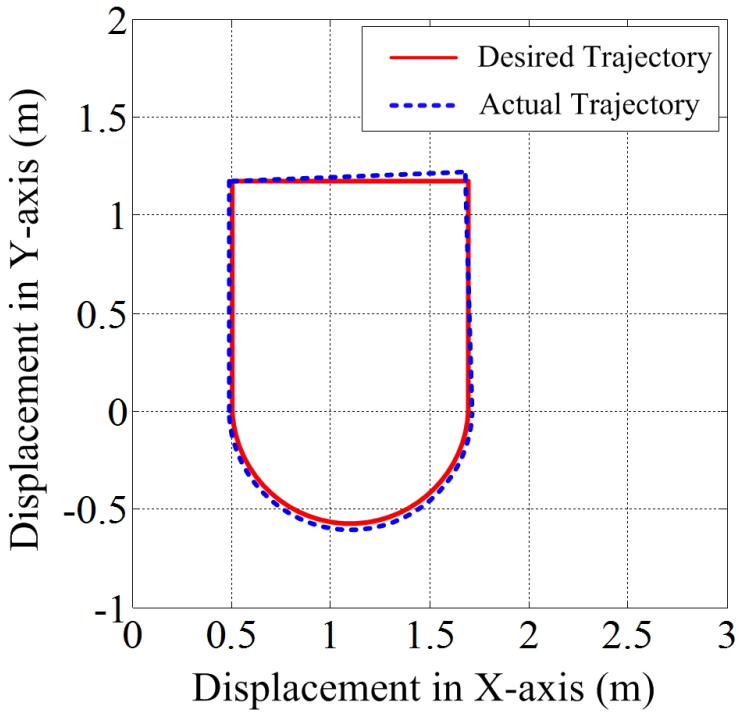

Figure A.2. Trajectory following performance of the robot.

length of the square edge is $1.2m$, which is same with the diameter of the half circle. It is seen that the robot can almost exactly follow the desired trajectory, which means the robot can conduct straight movement, point turning and different steering. But it is noted that the turning radius was a little larger than the desired one. The reason causing this could be the side slip happened to the wheels.

A.2 Obstacle Negotiation

To verify the obstacle negotiability of the wheel-paddle robot, tests were conducted with indoor man-made obstacles. As shown in Fig. A.3(a), the robot was crossing cylinder woods with height of $0.1m$, which is nearly the diameter of the wheel. During the climbing process, the wheel will slip if contacting with the wood. The slippage will stop till the paddles contact with the woods and climb up, which means the robot can not successfully cross the woods without the assistance of the paddles.

Fig. A.3(b)(c) show the process of the robot climbing up the slops of $15deg$ and $30deg$ separately. During the tests, the robot was actuated to perform wheel-support at a forward speed of $0.1m/s$. It was found the slippage happened to the wheels while climbing slop of $30deg$. For the wheel-support mode, the largest incline of the slop is dependent on the substrate material as well.

The obstacle negotiation experiment was also conducted in outdoor field. As shown in Fig. A.4(a), the robot was traversing rough grass land and crossing over obstacles with the height of nearly $0.11m$. In Fig. A.4(b), the robot was actuated to walk from grass land to stones and deal with a step at last. During all the process, the robot works at the hybrid-support configuration. The stone land has an incline of nearly $10deg$. It is verified that the robot performing with hybrid mode can realize turning, upslope, obstacle negotiating in rough terrains as well.

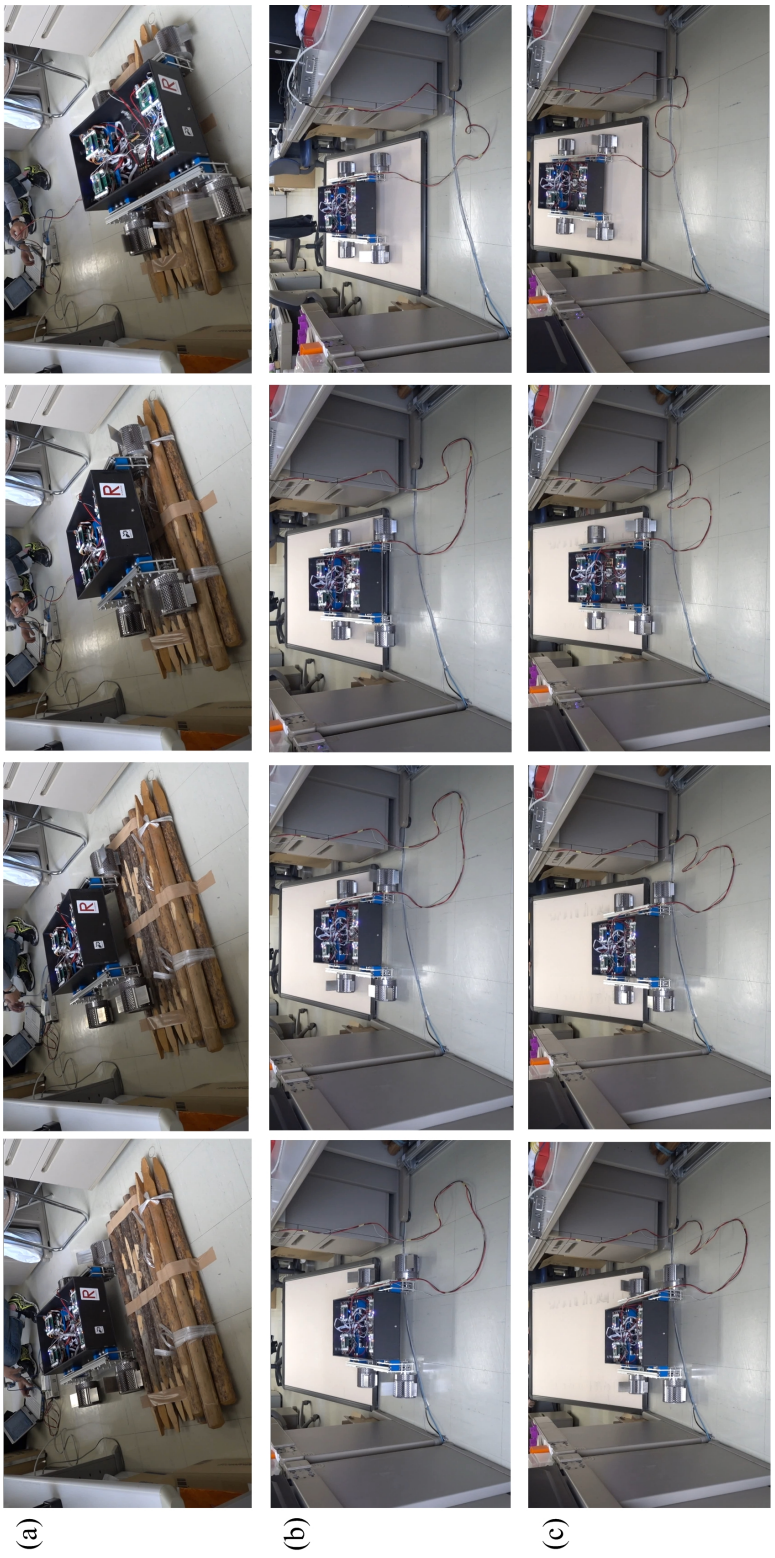

Figure A.3. Obstacle negotiability of the robot with indoor tests: (a) crossing over woods of $0.1m$; (b) uphill a slop of $15deg$; (c) uphill a slop of $30deg$.

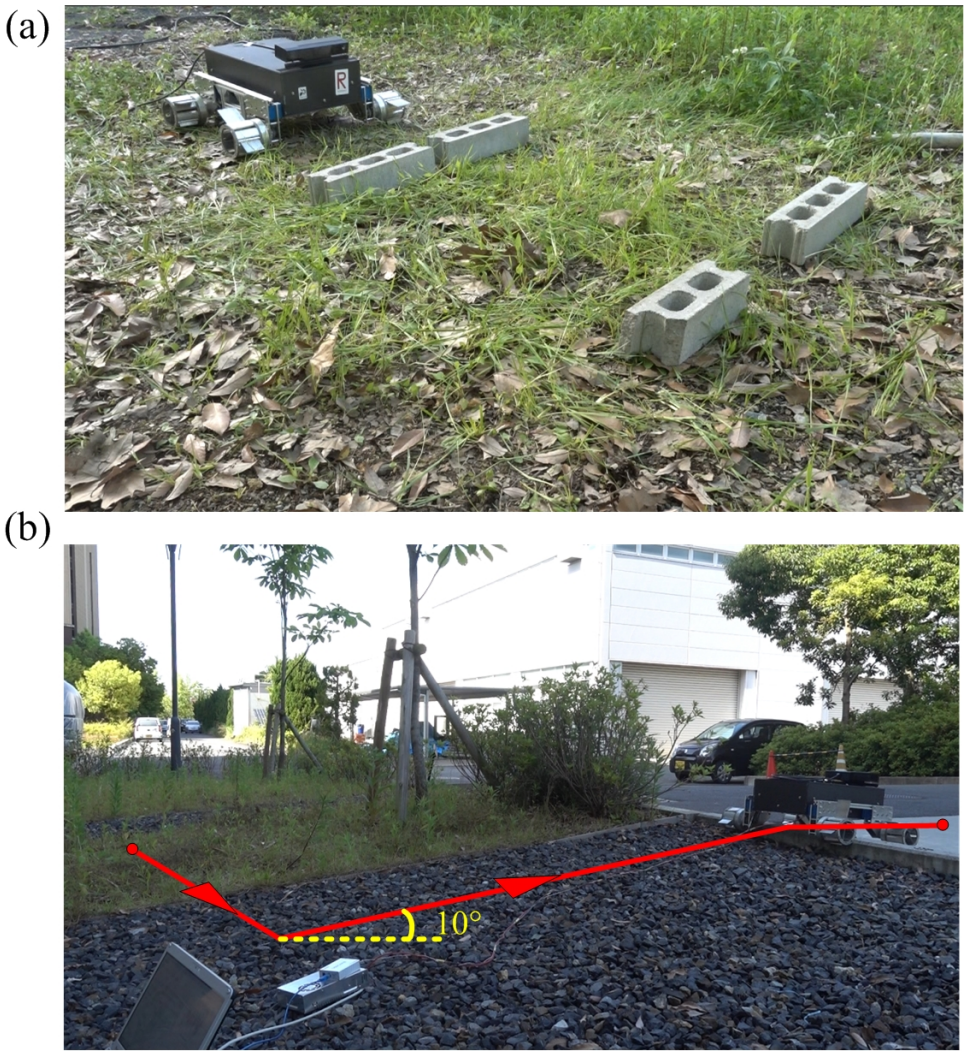

Figure A.4. Trajectory following performance of the robot.

A.3 Motion Accuracy of Paddle Shaft

As explained in above chapters, each wheel-paddle module contains three actively actuated joints. One controls the rotation of the wheel, the other two control the location of the paddle shaft. To ensure the performance of each joint in the robot, the trajectory following experiment in Section. A.1 has proved the accuracy of the wheel joint. To make sure the paddle shaft can also be controlled to locate accurately, trajectory following test of the paddle shaft was conducted as well.

As shown in Fig. A.5, a half-circle and a direct line has been used as the reference trajectory. It is seen that the actual trajectory almost coincide with the desired trajectory, which has verified that the paddle shaft can realize accurate positioning.

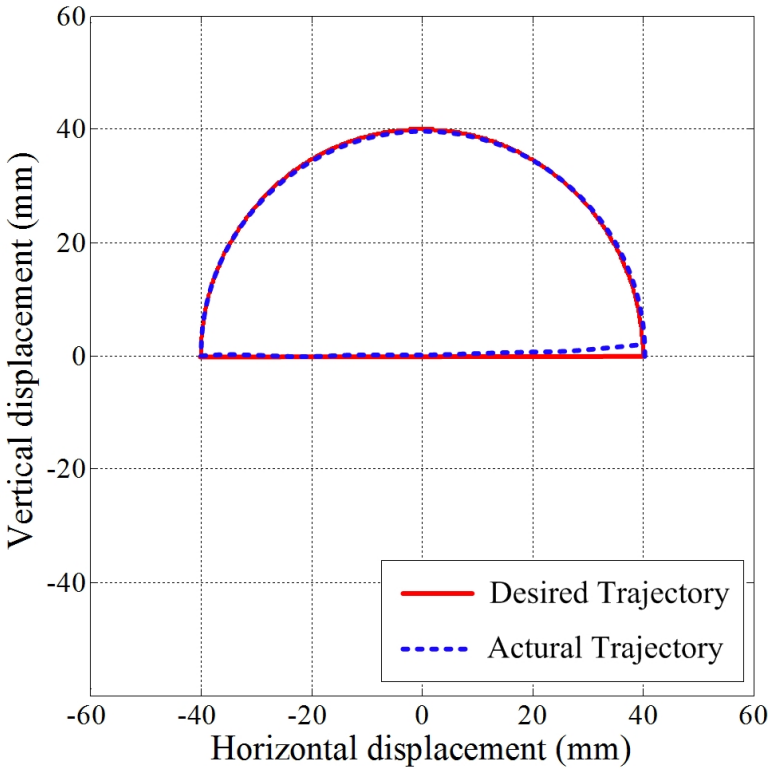

Figure A.5. Trajectory following results of the paddle shaft.

Appendix B

To Date Publications of the Wheel-Paddle Robot

Robot Design:

1. Yayi Shen, Guoteng Zhang, Yang Tian and Shugen Ma, Development of a wheel-paddle integrated quadruped robot for rough terrain and its verification on hybrid mode, ***IEEE Robotics and Automation Letters***, vol.3, no.4, pp. 4062–4067, 2018.

2. Yayi Shen, Shugen Ma, Hiroki Tomita, et al., Development of a Multi-terrestrial Robot with Eccentric Paddle Mechanism, In *Proc. of the 2018 JSME Conference on Robotics and Mechatronics (**ROBOMECH 2018**)*, Kitakyushu, Japan, pp. 2A2–L07, Jun. 2018.

3. Yi Sun, Yang Yang, Shugen Ma, et al., Design of a high-mobility multi-terrain robot based on eccentric paddle mechanism, ***Robotics and biomimetics***, 3(1): 8, 2016.

4. Yayi Shen, Huayan Pu, Yi Sun, et al., Improved effective design of the eccentric paddle mechanism for amphibious robots, In *Proc. of the 2014 IEEE Int. Conf. on Robotics and Biomimetics (**ROBIO'14**)*, Bali, Indonesia, pp. 437–442, Dec. 2014.

5. Yi Sun and Shugen Ma, A versatile locomotion mechanism for amphibious robots: Eccentric paddle mechanism, ***Advanced Robotics***, vol.27, no.8, pp. 611–625, 2013.

6. Yi Sun and Shugen Ma, ePaddle mechanism: Towards the development of a versatile amphibious locomotion mechanism, In *Proc. of the 2011 IEEE/RSJ Int. Conf. on Intelligent Robots and Systems (**IROS'11**)*, San Fancisco, USA, pp. 50355040, Sept. 2011.

7. Yi Sun and Shugen Ma, Legged gaits planning for a novel ePaddle-based amphibious robot, In *Proc. of the 2011 IEEE Int. Conf. on Robotics and Biomimetics (**ROBIO'11**)*, Phuket, Thailand, pp. 299304, Dec. 2011.

8. Yi Sun, Shugen Ma, and Xin Luo, Design of an eccentric paddle locomotion mechanism for amphibious robots, In *Proc. of the 2010 IEEE Int. Conf. on Robotics and Biomimetics (**ROBIO'10**)*, Tianjin, China, pp. 10981103, Dec. 2010.

Flat Ground Motion:

1. Huayan Pu, Chang Liu, Yi Sun, et al., Optimized non-reciprocating legged gait for an eccentric paddle mechanism, ***Robotics and Autonomous Systems***, 103: 83–92, 2018.

2. Huayan Pu, Jinglei Zhao, Yi Sun, et al., Non-reciprocating legged gait for robot with epicyclic-gear-based eccentric paddle mechanism, ***Robotics and Autonomous Systems***, 68: 36–46, 2015.

3. Jun Zou, Huayan Pu, Yayi Shen, et al., Optimized non-reciprocating tripod gait for a hexapod robot with epicyclic-gear-based eccentric paddle mechanism, In *Proc. of the 2015 IEEE Int. Conf. on Robotics and Biomimetics (**ROBIO'15**)*, Zhuhai, China, pp. 564–569, Dec. 2015.

4. Jinglei Zhao, Huayan Pu, Yi Sun, et al., Stability analysis and gait planning of a quadruped robot based on the eccentric paddle mechanism, ***Control Intelligent Systems***, 42(4): 311-7, 2014.

5. Yi Sun, Shugen Ma, Yang Yang and Huayan Pu, Towards stable and efficient legged race-walking of an ePaddle-based robot, ***Mechatronics***, vol.23, no.1, pp. 108–120, 2013.

6. Huayan Pu, Yi Sun, Shugen Ma, Yang Yang, et al., Design and locomotion simulation of an improved eccentric paddle mechanism for amphibious robots, In *Proc. of the 2013 IEEE Int. Conf. on Robotics and Biomimetics (**ROBIO'13**)*, Shenzhen, China, pp. 510–515, Dec. 2013.

7. Yi Sun, Shugen Ma and Yang Yang, Planning of legged racewalking gait for an ePaddle-based amphibious robot, In *Proc. of the 10th Int. IFAC Symp. on Robot Control (**SYROCO'12**)*, Dubrovnik, Croatia, pp. 218–223, Sept. 2012.

8. Yi Sun and Shugen Ma, Decoupled kinematic control of terrestrial locomotion for an ePaddle-based reconfigurable amphibious robot, In *Proc. of the 2011 IEEE Int. Conf. on Robotics and Automation (**ICRA'11**)*, Shanghai, China, pp. 1223-1228, May. 2011.

Uneven Terrain Motion:

1. Yi Sun, Yang Yang, Shugen Ma, et al., Modeling paddle-aided stair-climbing for a mobile robot based on eccentric paddle mechanism, In *Proc. of the 2015 IEEE/RSJ Int. Conf. on Intelligent Robots and Systems (**IROS'15**)*, Hamburg, Germany, pp. 4153–4158, Sep. 2015.

2. Yang Yang, Yi Sun and Shugen Ma, Drawbar pull of a wheel with an actively actuated lug on sandy terrain, ***Journal of Terramechanics***, vol.56, pp. 17–24, 2014.

3. Yang Yang, Yi Sun, Shugen Ma and Ryohei Yamamoto, Characteristics of normal and tangential forces acting on a single lug during translational motion in sandy soil, ***Journal of Terramechanics***, vol.55, pp. 47–59, 2014.

4. Yang Yang, Yi Sun and Shugen Ma, Effect of lug sinkage length to drawbar pull of a wheel with an actively actuated lug on sandy terrain, In *Proc. of the 2014 IEEE Int. Conf. on Robotics and Automation (**ICRA'14**)*, Hongkong, China, pp. 2932–2937, Jun. 2014.

5. Yang Yang, Yi Sun, Ryohei Yamamoto and Shugen Ma, Characteristics of tangential force acting on a single lug with translational motion in sandy soil, In *Proc. of the 2014 IEEE Int. Conf. on CYBER Technology in Automation, Control, and Intelligent Systems (**CYBER'14**)*, Hongkong, China, pp. 31–36, Jun. 2014.

6. Yang Yang, Yi Sun, Ryohei Yamamoto and Shugen Ma, Influence of moving direction on normal force acting on a single lug during translational motion in sandy soil, In *Proc. of the 2014 IEEE Int. Conf. on Robotics and Biomimetics (**ROBIO'14**)*, Bali, Indonesia, pp. 425–430, Dec. 2014.

7. Ryohei Yamamoto, Yang Yang, Yi Sun and Shugen Ma, Influences of lug motion on lug-soil reaction forces in sandy soil, In *Proc. of the 2014 IEEE Int. Conf. on Automation Science and Engineering (**CASE'14**)*, Taipei, Taiwan, pp. 176–181, Aug. 2014.

8. Ryohei Yamamoto, Yang Yang, Yi Sun and Shugen Ma, Characteristics of lug-soil interaction forces acting on a rotating lug in sandy soil, In *Proc. of the 2014 IEEE Int. Conf. on Robotics and Biomimetics (**ROBIO'14**)*, Bali, Indonesia, pp. 451–456, Dec., 2014.

9. Yang Yang, Yi Sun and Shugen Ma, Paddle trajectory generation for accessing soft terrain by an ePaddle locomotion mechanism, In *Proc. of the 2013 IEEE Int. Conf. on Robotics and Automation (**ICRA'13**)*, Karlsruhe, Germany, pp. 403–408, May. 2013.

Aquatic Motion:

1. Yayi Shen, Huayan Pu and Shugen Ma, Realizing efficient front crawl stroke with a wheel-paddle integrated mechanism: inspired by human competitive swimming, ***IEEE Journal of Oceanic Engineering***, Early access, 2019.

2. Yayi Shen, Yi Sun, Huayan Pu and Shugen Ma, Experimental verification of the oscillating paddling gait for an ePaddle-EGM amphibious Locomotion mechanism,

IEEE Robotics and Automation Letters (with ***IROS 2017*** option), vol.2, no.4, pp. 2322–2327, 2017.

3. Yayi Shen, Huayan Pu, Yi Sun, et al., Generating vectored thrust with the rotational paddling gait of an ePaddle-EGM mechanism: Modeling and experimental verifications, ***IEEE Journal of Oceanic Engineering***, vol.42, no.3, pp. 522–531, 2017.

4. Huayan Pu, Yi Sun, Shugen Ma, et al., Experimental study on the oscillating paddling gait of an epaddle mechanism with flexible configuration, ***Advanced Robotics***, vol.28, no.11, pp. 769–780, 2014.

5. Huayan Pu, Yi Sun, Yang Yang, and Shugen Ma, Modeling of the oscillating-paddling gait for an epaddle locomotion mechanism, In *Proc. of the 2013 IEEE Int. Conf. on Robotics and Automation (**ICRA'13**)*, Karlsruhe, German, pp. 3429–3435, May. 2013.

6. Yi Sun, Shugen Ma, Kazuhiro Fujita, Yang Yang, and Huayan Pu, Modeling the rotational paddling of an ePaddle-based amphibious robot, In *Proc. of the 2012 IEEE/RSJ Int. Conf. on Intelligent Robots and Systems (**IROS'12**)*, Algarve, Portugal, pp. 610–615, Oct. 2012.

7. Huayan Pu, Yi Sun, Shugen Ma, and Zhenbang Gong, Experimental study on oscillating paddling gait of an eccentric paddle mechanism, In *Proc. of the 2012 IEEE Int. Conf. on Robotics and Biomimetics (**ROBIO'12**)*, Guangzhou, China, pp. 187–192, Dec. 2012.

Bibliography

[1] Y. Sun and S. Ma, "A versatile locomotion mechanism for amphibious robots: eccentric paddle mechanism," *Advanced Robotics*, vol. 27, no. 8, pp. 611–625, 2013.

[2] K. Kato and S. Hirose, "Development of the quadruped walking robot, TITAN-IX-Mechanical design concept and application for the humanitarian de-mining robot," *Advanced Robotics*, vol. 15, no. 2, pp. 191–204, 2001.

[3] C. Semini, N. G. Tsagarakis, E. Guglielmino, M. Focchi, F. Cannella, and D. G. Caldwell, "Design of HyQ–a hydraulically and electrically actuated quadruped robot," *Proceedings of the Institution of Mechanical Engineers, Part I: Journal of Systems and Control Engineering*, vol. 225, no. 6, pp. 831–849, 2011.

[4] C. Semini, V. Barasuol, T. Boaventura, M. Frigerio, M. Focchi, D. G. Caldwell, and J. Buchli, "Towards versatile legged robots through active impedance control," *The International Journal of Robotics Research*, vol. 34, no. 7, pp. 1003–1020, 2015.

[5] M. Hutter, C. Gehring, A. Lauber, F. Gunther, C. Bellicoso, V. Tsounis, P. Fankhauser, R. Diethelm, S. Bachmann, M. Bloesch *et al.*, "ANYmal-toward legged robots for harsh environments," *Advanced Robotics*, vol. 31, no. 17, pp. 918–931, 2017.

[6] S. Seok, A. Wang, M. Y. Chuah, D. Otten, J. Lang, and S. Kim, "Design principles for highly efficient quadrupeds and implementation on the mit cheetah robot," in *Robotics and Automation (ICRA), 2013 IEEE International Conference on.* IEEE, 2013, pp. 3307–3312.

[7] U. Saranli, M. Buehler, and D. E. Koditschek, "Rhex: A simple and highly mobile hexapod robot," *The International Journal of Robotics Research*, vol. 20, no. 7, pp. 616–631, 2001.

[8] K.-J. Huang, C.-K. Huang, and P.-C. Lin, "A simple running model with rolling contact and its role as a template for dynamic locomotion on a hexapod robot," *Bioinspiration & biomimetics*, vol. 9, no. 4, p. 046004, 2014.

[9] Y.-C. Chou, K.-J. Huang, W.-S. Yu, and P.-C. Lin, "Model-based development of leaping in a hexapod robot," *IEEE Transactions on Robotics*, vol. 31, no. 1, pp. 40–54, 2015.

[10] W.-H. Chen, H.-S. Lin, Y.-M. Lin, and P.-C. Lin, "TurboQuad: A novel leg–wheel transformable robot with smooth and fast behavioral transitions," *IEEE Transactions on Robotics*, vol. 33, no. 5, pp. 1025–1040, 2017.

[11] Y.-S. Kim, G.-P. Jung, H. Kim, K.-J. Cho, and C.-N. Chu, "Wheel transformer: A wheel-leg hybrid robot with passive transformable wheels," *IEEE Transactions on Robotics*, vol. 30, no. 6, pp. 1487–1498, 2014.

[12] J.-J. Chou and L.-S. Yang, "Innovative design of a claw-wheel transformable robot," in *Robotics and Automation (ICRA), 2013 IEEE International Conference on*. IEEE, 2013, pp. 1337–1342.

[13] C. Li, P. B. Umbanhowar, H. Komsuoglu, D. E. Koditschek, and D. I. Goldman, "Sensitive dependence of the motion of a legged robot on granular media," *Proceedings of the National Academy of Sciences*, vol. 106, no. 9, pp. 3029–3034, 2009.

[14] K. Terzaghi, *Theoretical soil mechanics*. Chapman And Hall, Limited.; London, 1951.

[15] R. M. Nedderman, *Statics and kinematics of granular materials*. Cambridge University Press, 2005.

[16] P. Heil, E. C. Rericha, D. I. Goldman, and H. L. Swinney, "Mach cone in a shallow granular fluid," *Physical Review E*, vol. 70, no. 6, p. 060301, 2004.

[17] J. Aguilar, T. Zhang, F. Qian, M. Kingsbury, B. McInroe, N. Mazouchova, C. Li, R. Maladen, C. Gong, M. Travers *et al.*, "A review on locomotion robophysics: the study of movement at the intersection of robotics, soft matter and dynamical systems," *Reports on Progress in Physics*, vol. 79, no. 11, p. 110001, 2016.

[18] C. Li, P. B. Umbanhowar, H. Komsuoglu, and D. I. Goldman, "The effect of limb kinematics on the speed of a legged robot on granular media," *Experimental mechanics*, vol. 50, no. 9, pp. 1383–1393, 2010.

[19] C. Li, T. Zhang, and D. I. Goldman, "A terradynamics of legged locomotion on granular media," *science*, vol. 339, no. 6126, pp. 1408–1412, 2013.

[20] H. Marvi, C. Gong, N. Gravish, H. Astley, M. Travers, R. L. Hatton, J. R. Mendelson, H. Choset, D. L. Hu, and D. I. Goldman, "Sidewinding with minimal slip: Snake and robot ascent of sandy slopes," *Science*, vol. 346, no. 6206, pp. 224–229, 2014.

[21] H. C. Astley, C. Gong, J. Dai, M. Travers, M. M. Serrano, P. A. Vela, H. Choset, J. R. Mendelson, D. L. Hu, and D. I. Goldman, "Modulation of orthogonal body waves enables high maneuverability in sidewinding locomotion," *Proceedings of the National Academy of Sciences*, vol. 112, no. 19, pp. 6200–6205, 2015.

[22] N. Mazouchova, P. B. Umbanhowar, and D. I. Goldman, "Flipper-driven terrestrial locomotion of a sea turtle-inspired robot," *Bioinspiration & biomimetics*, vol. 8, no. 2, p. 026007, 2013.

[23] S. Zhang, Y. Zhou, M. Xu, X. Liang, J. Liu, and J. Yang, "Amphihex-i: Locomotory performance in amphibious environments with specially designed transformable flipper legs," *IEEE/ASME Transactions on Mechatronics*, vol. 21, no. 3, pp. 1720–1731, 2016.

[24] H. Kim and J. Lee, "Design, swimming motion planning and implementation of a legged underwater robot (caleb10: D. beebot) by biomimetic approach," *Ocean Engineering*, vol. 130, pp. 310–327, 2017.

[25] H. Hu, J. Oyekan, and D. Gu, "A school of robotic fish for pollution detection in port," *Biologically Inspired Robotics (Y. Liu and D. Sun, eds.)*, pp. 85–104, 2011.

[26] P. R. Bandyopadhyay, "Trends in biorobotic autonomous undersea vehicles," *IEEE Journal of Oceanic Engineering*, vol. 30, no. 1, pp. 109–139, 2005.

[27] S. F. Masoomi, "An efficient biomimetic swimming robot capable of multiple gaits of locomotion: design, modelling and fabrication." 2014.

[28] K. Kikuchi, Y. Uehara, Y. Kubota, and O. Mochizuki, "Morphological considerations of fish fin shape on thrust generation." *Journal of Applied Fluid Mechanics*, vol. 7, no. 4, 2014.

[29] K. L. Feilich and G. V. Lauder, "Passive mechanical models of fish caudal fins: effects of shape and stiffness on self-propulsion," *Bioinspiration & biomimetics*, vol. 10, no. 3, p. 036002, 2015.

[30] K. N. Lucas, P. J. Thornycroft, B. J. Gemmell, S. P. Colin, J. H. Costello, and G. V. Lauder, "Effects of non-uniform stiffness on the swimming performance of a passively-flexing, fish-like foil model," *Bioinspiration & biomimetics*, vol. 10, no. 5, p. 056019, 2015.

[31] Y.-J. Park, T. M. Huh, D. Park, and K.-J. Cho, "Design of a variable-stiffness flapping mechanism for maximizing the thrust of a bio-inspired underwater robot," *Bioinspiration & biomimetics*, vol. 9, no. 3, p. 036002, 2014.

[32] Y.-J. Park, U. Jeong, J. Lee, S.-R. Kwon, H.-Y. Kim, and K.-J. Cho, "Kinematic condition for maximizing the thrust of a robotic fish using a compliant caudal fin," *IEEE Transactions on Robotics*, vol. 28, no. 6, pp. 1216–1227, 2012.

[33] D. B. Quinn, G. V. Lauder, and A. J. Smits, "Maximizing the efficiency of a flexible propulsor using experimental optimization," *Journal of Fluid Mechanics*, vol. 767, pp. 430–448, 2015.

[34] C. Eloy, "On the best design for undulatory swimming," *Journal of Fluid Mechanics*, vol. 717, pp. 48–89, 2013.

[35] H. Park, Y.-J. Park, B. Lee, K.-J. Cho, and H. Choi, "Vortical structures around a flexible oscillating panel for maximum thrust in a quiescent fluid," *Journal of Fluids and Structures*, vol. 67, pp. 241–260, 2016.

[36] L. Wen, T. Wang, G. Wu, and J. Liang, "Quantitative thrust efficiency of a self-propulsive robotic fish: Experimental method and hydrodynamic investigation," *IEEE/ASME Transactions on Mechatronics*, vol. 18, no. 3, pp. 1027–1038, 2013.

[37] Y. Shen, Y. Sun, H. Pu, and S. Ma, "Experimental verification of the oscillating paddling gait for an epaddle-egm amphibious locomotion mechanism," *IEEE Robotics and Automation Letters*, vol. 2, no. 4, pp. 2322–2327, 2017.

[38] C. Georgiades, M. Nahon, and M. Buehler, "Simulation of an underwater hexapod robot," *Ocean Engineering*, vol. 36, no. 1, pp. 39–47, 2009.

[39] H. Pu, Y. Sun, Y. Yang, S. Ma, and Z. Gong, "Modeling of the oscillating-paddling gait for an epaddle locomotion mechanism," in *2013 IEEE International Conference on Robotics and Automation*. IEEE, 2013, pp. 3429–3435.

[40] H. Pu, Y. Sun, S. Ma, Z. Gong, and J. Luo, "Experimental study on the oscillating paddling gait of an epaddle mechanism with flexible configuration," *Advanced Robotics*, vol. 28, no. 11, pp. 769–780, 2014.

[41] Y. S. Song and M. Sitti, "Surface-tension-driven biologically inspired water strider robots: Theory and experiments," *IEEE Transactions on robotics*, vol. 23, no. 3, pp. 578–589, 2007.

[42] X. Jia, Z. Chen, A. Riedel, T. Si, W. R. Hamel, and M. Zhang, "Energy-efficient surface propulsion inspired by whirligig beetles," *IEEE Transactions on Robotics*, vol. 31, no. 6, pp. 1432–1443, 2015.

[43] Y. Shen, H. Pu, Y. Sun, J. Zhao, S. Ma, J. Luo, and Z. Gong, "Improved effective design of the eccentric paddle mechanism for amphibious robots," in *2014 IEEE International Conference on Robotics and Biomimetics (ROBIO 2014)*. IEEE, 2014, pp. 437–442.

[44] Y. Yang, Y. Sun, and S. Ma, "Drawbar pull of a wheel with an actively actuated lug on sandy terrain," *Journal of Terramechanics*, vol. 56, pp. 17–24, 2014.

[45] Y. Shen, G. Zhang, Y. Tian, and S. Ma, "Development of a wheel-paddle integrated quadruped robot for rough terrain and its verification on hybrid mode," *IEEE Robotics and Automation Letters*, vol. 3, no. 4, pp. 4062–4067, 2018.

[46] H. Pu, J. Zhao, Y. Sun, S. Ma, J. Luo, and Z. Gong, "Non-reciprocating legged gait for robot with epicyclic-gear-based eccentric paddle mechanism," *Robotics and Autonomous Systems*, vol. 68, pp. 36–46, 2015.

[47] H. Pu, C. Liu, Y. Sun, Y. Yang, J. Zou, N. Liu, S. Xie, Y. Peng, and J. Luo, "Optimized non-reciprocating legged gait for an eccentric paddle mechanism," *Robotics and Autonomous Systems*, vol. 103, pp. 83–92, 2018.

[48] Y. Sun, S. Ma, Y. Yang, and H. Pu, "Towards stable and efficient legged race-walking of an epaddle-based robot," *Mechatronics*, vol. 23, no. 1, pp. 108–120, 2013.

[49] Y. Kanayama, "Two dimensional wheeled vehicle kinematics," in *Proceedings of the 1994 IEEE International Conference on Robotics and Automation*. IEEE, 1994, pp. 3079–3084.

[50] S. Teitler and R. Proodian, "'what price speed', revisited," *Journal of Energy*, vol. 4, no. 1, pp. 46–48, 1980.

[51] G. Dudek, P. Giguere, C. Prahacs, S. Saunderson, J. Sattar, L.-A. Torres-Mendez, M. Jenkin, A. German, A. Hogue, A. Ripsman *et al.*, "Aqua: An amphibious autonomous robot," *Computer*, vol. 40, no. 1, pp. 46–53, 2007.

[52] C. Georgiades, M. Nahon, and M. Buehler, "Simulation of an underwater hexapod robot," *Ocean Engineering*, vol. 36, no. 1, pp. 39–47, 2009.

[53] Y. Sun, S. Ma, K. Fujita, Y. Yang, and H. Pu, "Modeling the rotational paddling of an epaddle-based amphibious robot," in *2012 IEEE/RSJ International Conference on Intelligent Robots and Systems*. IEEE, 2012, pp. 610–615.

[54] G. I. Taylor, "Analysis of the swimming of long and narrow animals," *Proceedings of the Royal Society of London. Series A. Mathematical and Physical Sciences*, vol. 214, no. 1117, pp. 158–183, 1952.

[55] M. J. Lighthill, "Large-amplitude elongated-body theory of fish locomotion," *Proceedings of the Royal Society of London. Series B. Biological Sciences*, vol. 179, no. 1055, pp. 125–138, 1971.

[56] C. E. Jordan, "Coupling internal and external mechanics to predict swimming behavior: a general approach," *American Zoologist*, vol. 36, no. 6, pp. 710–722, 1996.

[57] J. Morison, J. Johnson, S. Schaaf *et al.*, "The force exerted by surface waves on piles," *Journal of Petroleum Technology*, vol. 2, no. 05, pp. 149–154, 1950.

[58] E. Kelasidi, K. Y. Pettersen, and J. T. Gravdahl, "Modeling of underwater snake robots moving in a vertical plane in 3d," in *2014 IEEE/RSJ International Conference on Intelligent Robots and Systems*. IEEE, 2014, pp. 266–273.

[59] E. Kelasidi, P. Liljeback, K. Y. Pettersen, and J. T. Gravdahl, "Innovation in underwater robots: Biologically inspired swimming snake robots," *IEEE robotics & automation magazine*, vol. 23, no. 1, pp. 44–62, 2016.

[60] W. Khalil, G. Gallot, and F. Boyer, "Dynamic modeling and simulation of a 3-d serial eel-like robot," *IEEE Transactions on Systems, Man, and Cybernetics, Part C (Applications and Reviews)*, vol. 37, no. 6, pp. 1259–1268, 2007.

[61] M. Paidoussis, "8 solitary cylindrical structures in axial flow," in *Slender Structures and Axial Flow ser. Fluid-Structure Interactions*. Academic Press, 2003, vol. 2, pp. 787–1032.

[62] E. Kelasidi, K. Y. Pettersen, J. T. Gravdahl, and P. Liljebäck, "Modeling of underwater snake robots," in *2014 IEEE International Conference on Robotics and Automation (ICRA)*. IEEE, 2014, pp. 4540–4547.

[63] M. Misiti, Y. Misiti, G. Oppenheim, and J.-M. Poggi, "Wavelet toolbox," *The MathWorks Inc., Natick, MA*, vol. 15, p. 21, 1996.

[64] A. B. Craig, P. L. Skehan, J. A. Pawelczyk, and W. L. Boomer, "Velocity, stroke rate, and distance per stroke during elite swimming competition," *Med Sci Sports Exerc*, vol. 17, no. 6, pp. 625–634, 1985.

[65] S. Changalur and P. Brown, "An analysis of male and female olympic swimmers in the 200-meters events," *Can. J. Sport Sci*, vol. 17, pp. 104–109, 1992.

[66] A. P. Hollander, "Contribution of the legs to propulsion in front crawl swimming," *Swimming science*, pp. 17–29, 1987.

[67] T. Yanai and J. G. Hay, "Shoulder impingement in front-crawl swimming: Ii. analysis of stroking technique." *Medicine and science in sports and exercise*, vol. 32, no. 1, pp. 30–40, 2000.

[68] Y. Shen, H. Pu, and S. Ma, "Realizing efficient front crawl stroke with a wheel-paddle-integrated mechanism: inspired by human competitive swimming," *IEEE Journal of Oceanic Engineering (Early Access)*, 2019.